Dynamics and Interactions of Metal-Binding Domains in the Function of Wilson Disease Protein.

A Thesis Submitted to the
College of Graduate Studies and Research
In Partial Fulfillment of the Requirements
For the Degree of Doctor of Philosophy
In the Department of Biochemistry
University of Saskatchewan
Saskatoon

PERMISSION TO USE

In presenting this thesis in partial fulfillment of the requirements for a Postgraduate degree from the University of Saskatchewan, I agree that the Libraries of the University may make it freely available for inspection. I further agree that permission for copying of thesis in any manner, in whole or in part, for scholarly purposes may be granted by the professor of professors who supervised my thesis work or, in their absence by the Head of the Department or Dean of the College in which my thesis work was done. It is understood that any copying or publication or use of this thesis or parts thereof for financial gain shall not be allowed without my written permission. It is also understood that due recognition shall be given to me and to the University of Saskatchewan in any scholarly use, which may be made of any material in my thesis.

Requests for permission to copy or to make use of the material in this thesis in whole or in part should be addressed to:

Head of the Department of Biochemistry
University of Saskatchewan
Saskatoon, Saskatchewan, S7N 5E5

ABSTRACT

Wilson disease protein (ATP7B) is a P-type ATPase that catalyzes the transport of copper across cell membranes and is critical for maintaining copper homeostasis. ATP7B contains an N-terminal metal binding module that is found only in heavy metal transporters. The N-terminal region is composed of six metal-binding domains (MBD1-6) joined together by flexible linkers. Each MBD is approximately 70 amino acids and contains the signature motif, CXXC, with one Cu(I) binding between two cysteines. The structures of the individual MBDs have been solved, however, the dynamics and arrangement of the individual MBDs in the full-length protein were unknown. Gaining insights into the conformation and dynamics of this unique region helps us understand how the enzymatic and trafficking activity of ATP7B is regulated. In our study, we used recombinant single domain camelid antibodies, also known as nanobodies, to reveal functionally relevant transient interactions within a distinct group of MBDs. We identified new transient interactions between metal-binding domains 1, 2, and 3 and provided independent evidence for structurally and functionally distinct roles for MBD5-6. We demonstrated that nanobodies were used as effective probes for investigating molecular dynamics of multi-domain proteins.

Overexpression of ATP7B is associated with tumor resistance to cisplatin during chemotherapy. Cisplatin kills cancer cells by reacting with DNA, which prevents proper DNA transcription and replication. ATP7B was proposed to actively transport cisplatin out of the cell, however, low transport rates in physiological pH and high substrate specificity for copper suggests that cisplatin detoxification by active extrusion is unlikely. Rather, we proposed that the metal-binding domains in ATP7B functioned as a high-affinity reservoir by trapping cisplatin and then releasing it to other potential terminal acceptors in a non-toxic form. We used NMR spectroscopy to characterize cisplatin binding to metal-binding domain 2 (MBD2) of ATP7B. We demonstrated that platinum is transferred from Atox1 to MBD2 in a mechanism that parallels the copper-transport pathway in the cell, which suggested a possible route for cisplatin detoxification. Platinum was subsequently released to other terminal acceptors such as glutathione and glutaredoxin, which demonstrated that the metal-binding domains may not be the final destination for cisplatin.

ACKNOWLEDGEMENTS

I would like to thank my thesis supervisor, Dr. Oleg Dmitriev, for his tremendous support and guidance throughout my PhD program. I would also like to thank all the past and current members of the Dmitriev Lab for their technical support and advice: Hannah Pierson, Tahereh Haji, Christopher O'Grady, Dr. Natasha Dolgova, Eva Uhlemann, Daryna Kulik, and Dzmitriy Turavets. In particular, I'd like to thank Dr. Sergiy Nokhrin (University of Toronto) for all his help with NMR.

Lastly, I would like to thank my advisory committee members for their constructive criticism and continued support in my academic program: Drs. Jeremy Lee, Scot Leary, Mirek Cygler, and Ingrid Pickering.

TABLE OF CONTENTS

LIST OF TABLES

LIST OF FIGURES

LIST OF ABBREVIATIONS

A-domain	Actuator domain
Atox1	Antioxidant protein 1
ATP-BD	ATP-binding domain
ATP7A	Menkes disease protein
ATP7B	Wilson disease protein
CCS	Copper chaperone for superoxide dismutase 1
CSP	Chemical shift perturbation
CP	Ceruloplasmin
DDP	Cisplatin
FRET	Fluorescence resonance energy transfer
GSH	Glutathione
hCtr1	Human copper transporter 1
HCAbs	Heavy-chain antibodies
H/D	Hydrogen-deuterium
HSQC	Heteronuclear single quantum coherence
LpCopA	*Legionella pneumophila* CopA
N-domain	Nucleotide-binding domain
NER	Nucleotide excision repair
MBD	Metal-binding domain
NMR	Nuclear magnetic resonance
NOE	Nuclear Overhauser effect
P-domain	Phosphorylation domain
PPM	Parts per million
SA	Simulated annealing
SOD1	Superoxide dismutase 1
TAD	Torsion angle space
TGN	*Trans*-Golgi Network
TROSY	Transverse relaxation optimized spectroscopy
VHH	Variable domain of heavy-chain antibodies
XPA	Xeroderma pigmentosum complementation group A

1 Introduction

Copper is an essential trace element that mediates many cellular processes in living organisms including iron uptake, respiration, and radical detoxification. However, there are severe consequences when excess copper is not properly exported from the cell. Excess copper catalyzes the formation of reactive oxygen species that in turn cause protein malfunction and DNA mutations.

ATP7B is a P_{1B}-type ATPase that maintains copper homeostasis in the body. ATP7B uses the energy of ATP hydrolysis to translocate copper ions across the cell membrane. This copper transporter has two main functions in the liver, the tissue where ATP7B is primarily expressed. ATP7B transports copper into the secretory pathway for incorporation into copper-dependent enzymes. Another function of ATP7B involves excreting excess copper from the cell into bile. Mutations in ATP7B result in a severe disorder known as Wilson disease. Wilson disease is characterized by copper accumulation primarily in the liver and, if left untreated, severe hepatic disease and eventual death will occur.

ATP7B consists of a single polypeptide made up of several distinct domains. However, the most characteristic feature of heavy metal transporters is the N-terminal region containing six metal-binding domains. The N-terminal region functions by regulating copper transport and trafficking activity of ATP7B. The structures for all the individual metal-binding domains have been solved, but the arrangement of the individual metal-binding domains in the context of full-length MBD1-6 was unknown. Therefore, our main goal in this project was to examine the conformation and dynamics of MBD1-6 using high-resolution NMR spectroscopy.

2 Review of the literature

2.1 Physiological role of copper

2.1.1 Copper distribution and metabolism

Copper is an essential trace element that is required by living organisms in all the five kingdoms of life for proper growth and development. Copper mediates many biological functions in human cells by serving as a cofactor for numerous enzymes such as cytochrome oxidase, superoxide dismutase, and dopamine-β-hydroxlase (Lutsenko et al., 2007). The fast interconversion from oxidized Cu(II) to reduced Cu(I), and vice versa, allows copper to participate in many important biological redox reactions which include iron uptake, electron and oxygen transport, and radical detoxification (Lutsenko et al., 2007). However, excess copper is very toxic, catalyzing the formation of reactive oxygen species through the Haber-Weiss and Fenton reactions:

$$O_2\bullet^- + Cu^{2+} \rightarrow O_2 + Cu^+ \quad \text{(Haber-Weiss)} \quad (2.1)$$

$$Cu^+ + H_2O_2 \rightarrow Cu^{2+} + HO\bullet + OH^- \quad \text{(Fenton reaction)} \quad (2.2)$$

$$O_2\bullet^- + H_2O_2 \rightarrow O_2 + HO\bullet + OH^- \quad \text{(Net reaction)} \quad (2.3)$$

Reducing agents such as glutathione or ascorbate catalyze the conversion of Cu^{2+} to Cu^+ (reaction 2.1). Copper(I) spontaneously catalyzes the reaction with hydrogen peroxide (H_2O_2) to form the highly reactive hydroxyl radicals ($HO\bullet$) and anions (OH^-) (reaction 2.2). These reactive oxygen species can cause DNA mutations and protein malfunction. Therefore, mechanisms for maintaining copper homeostasis are critical for cell survival.

Dietary copper is absorbed by enterocytes in the small intestine and transported across the apical membrane by human copper transporter 1 (hCtr1) (Figure 2.1). In the enterocyte, copper chaperone antioxidant protein 1 (Atox1) binds and transports copper to Menkes disease Protein (ATP7A) (Hamza et al., 1999). As the copper concentration increases, ATP7A traffics to the basolateral membrane of the enterocyte and transports copper into the portal and general blood circulation (Ravia et al., 2005). In the bloodstream, copper is bound to serum proteins such as albumin and transcuprein (Linder, 1996). A majority of the copper in the bloodstream travels directly to the liver, and a smaller portion goes to the kidneys (Linder, 1996).

The liver is the major organ responsible for regulating copper homeostasis in the body. Wilson disease protein (ATP7B), a homologue of ATP7A, regulates the export of copper from the liver into the peripheral blood circulation. ATP7B has two main functions in the cell. It transports copper into the lumen of the *trans*-Golgi network (TGN) for incorporation into copper-dependent enzymes or it transports excess copper into bile for excretion (Lutsenko et al., 2007).

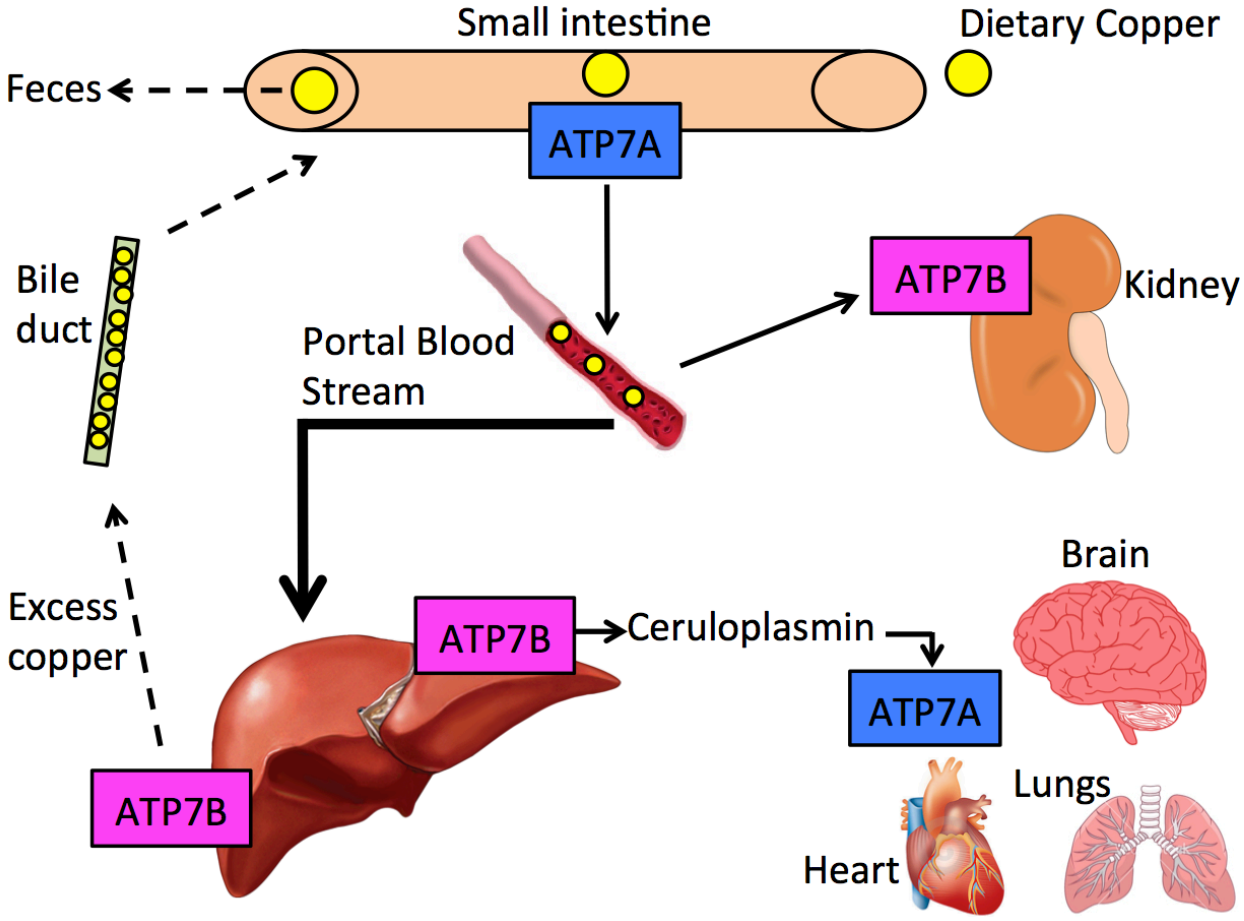

Figure 2.1: Copper distribution in the body. Under normal copper conditions, dietary copper (*yellow spheres*) is mainly absorbed in the small intestine and transported into the blood circulation by ATP7A. A majority of the copper entering the bloodstream goes to the liver and a smaller amount of copper goes to the kidneys. ATP7B transports excess copper to bile and to copper-dependent enzymes such as ceruloplasmin and albumin for peripheral blood circulation. Copper is transported into peripheral tissues that express ATP7A.

2.1.2 Intracellular trafficking of copper

Copper distribution in the cell is a tightly regulated process. Copper enters the cell by passive transport through hCtr1, a high-affinity copper channel in the plasma membrane. The hCtr1 monomer is 190 amino acids long and oligomerizes to a trimer to form the copper uptake pore (de Feo et al., 2009) (Figure 2.2A). It contains several characteristic sequence motifs that are involved in copper binding and transport through the cell membrane (Figure 2.2B). The N-terminal region contains histidine- and methionine-rich motifs that function in high-affinity copper uptake. These motifs capture copper ions in the extracellular space and transfer it towards the transmembrane pore. The second transmembrane domain contains the essential MxxxM motif that binds copper in the membrane and the third transmembrane domain contains a GxxxG motif that functions in helix packing and oligomerization (de Feo et al., 2009).

Since the transmembrane region contains only one copper-binding site near the extracellular side of the membrane, how does copper reach the cytoplasm? The authors proposed that binding of copper to the MxxxM binding site in TM2 triggers specific conformational changes that release copper to the C-terminal region (de Feo et al., 2009). The C-terminal region of hCtr1 contains an HCH motif, which has been proposed to function as a high-affinity copper sink that binds and directly transfers Cu(I) to chaperone proteins (de Feo et al., 2009).

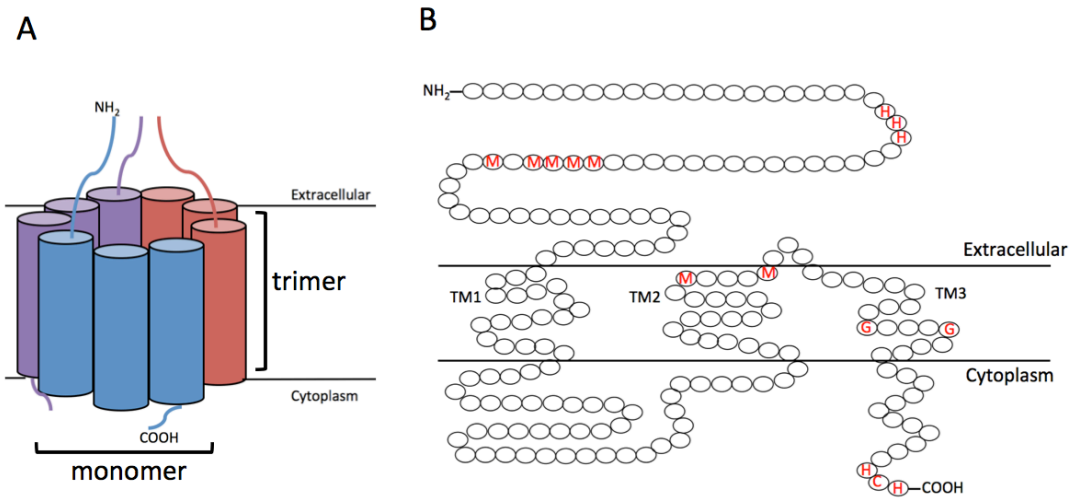

Figure 2.2: Structural model of hCtr1. (A) Side view of monomeric hCtr1 forming a pore in the membrane. (B) The sequence topology for the characteristic motifs of hCtr1 is highlighted (*red*).

The transfer of copper from hCtr1 to chaperone proteins is still a matter of debate. It was recently proposed that hCtr1 transfers Cu(I) to an exchangeable pool of copper-bound glutathione (GSH) (Maryon et al., 2013). GSH would function as an intermediary for chaperone proteins such as Atox1 to acquire Cu(I) (Figure 2.3; *red dashed arrows*). Copper chaperone proteins would have to search through the large cell volume and interact with Cu(I)-bound GSH in an orientation that is favorable for copper transfer. Instead, it was proposed that Atox1 directly acquires Cu(I) from hCtr1 by interacting electrostatically with the inner surface of the

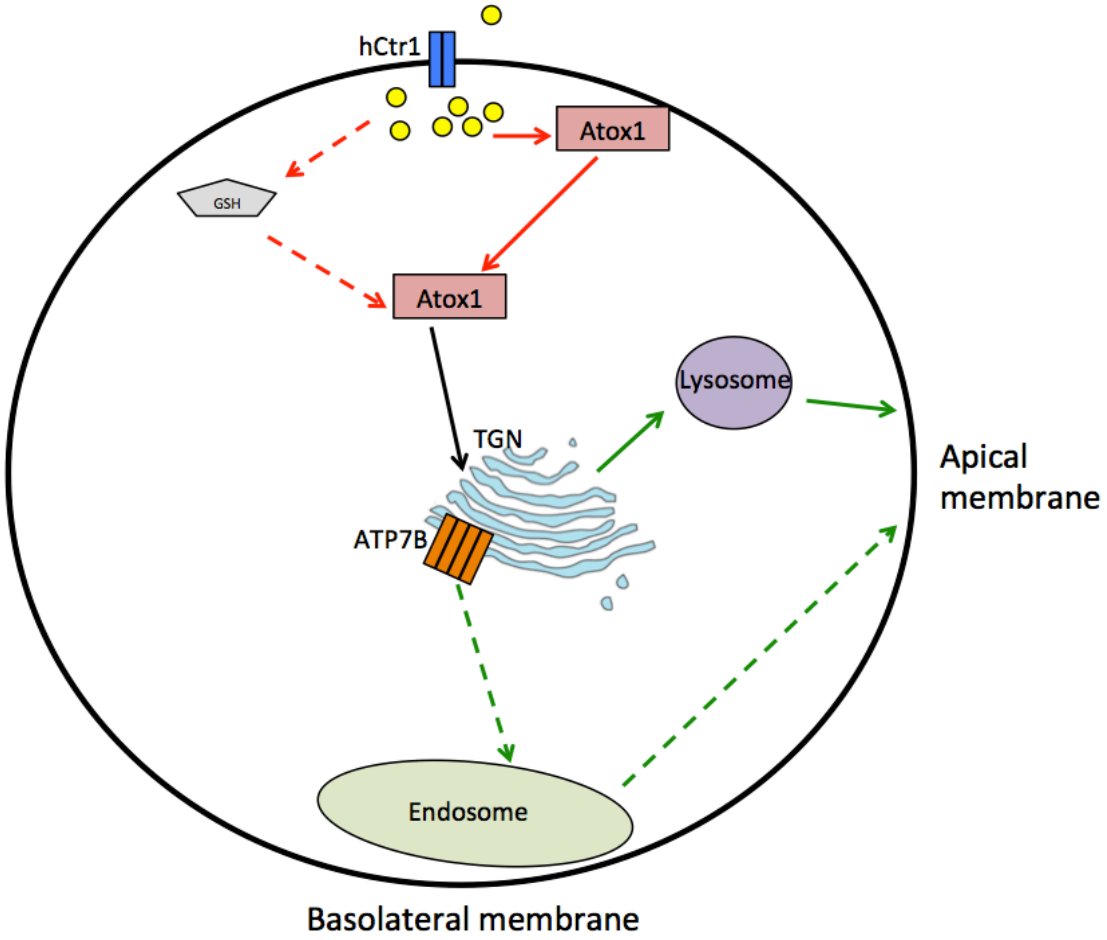

Figure 2.3: Proposed models of the copper transfer pathway and intracellular localization of ATP7B. Atox1 can either receive copper directly from hCtr1 (*red solid arrow*) or from copper-bound GSH (*red dashed arrow*). Atox1 transfers Cu(I) to ATP7B (*black arrow*). In the presence of copper, ATP7B will traffic to the apical membrane for subsequent copper excretion. To reach the apical membrane, two distinct trafficking routes have been proposed: ATP7B can either traffic to lysosomes (*green solid arrows*) or to basolateral endosomes (*green dashed arrows*) for subsequent excretion.

membrane bilayer (Flores and Unger, 2013) (Figure 2.3; *red solid arrows*). This mechanism has been observed for CCS (copper chaperone for superoxide dismutase 1) (Pope et al., 2013), as CCS must interact with lipid bilayers before activating superoxide dismutase 1 (SOD1) (Pope et al., 2013). Direct interaction between copper chaperones and the C-terminal copper-binding motif of hCtr1 would ensure an efficient mechanism of copper uptake and delivery in the cell.

Intracellular copper levels are controlled by protein-protein interactions and copper-dependent trafficking of ATP7B to different cell compartments. The human copper chaperone Atox1 plays a major role in copper distribution to the TGN, delivering copper to ATP7B and ATP7A (Hamza et al., 1999). Copper regulation of ATP7B is achieved by copper-induced trafficking (Figure 2.3). Although some studies have demonstrated that ATP7B does not exhibit copper-dependent trafficking (Harada et al., 2010; 2000), the general consensus is that, under low or basal copper concentrations, ATP7B is localized to the TGN. ATP7B transports copper from the cytoplasm into the lumen of the TGN for incorporation into various copper-dependent enzymes such as ceruloplasmin (CP), a major copper-carrying protein in the blood (Cater et al., 2004; 2006; Hung et al., 1997; Schaefer et al., 1999). An increase in copper concentration, however, triggers the movement of ATP7B from the TGN into cytoplasmic vesicles, which sequesters excess copper to be later removed by exocytosis at the apical canalicular membrane (Cater et al., 2006; Hung et al., 1997; Roelofsen et al., 2000). This process is reversible, allowing ATP7B to be recycled back into the TGN upon copper concentration decrease. Despite the observation of ATP7B copper-dependent trafficking to different cell compartments, the identity of the cytoplasmic vesicles and the trafficking route is still controversial. A study demonstrated that ATP7B directly traffics to lysosomes, which leads to ATP7B-lysosome mediated exocytosis at the apical membrane in HepG2 cells (Polishchuk et al., 2014) (Figure 2.3; *green solid arrows*). In contrast, two independent studies have more recently demonstrated that ATP7B reaches the apical membrane via basolateral endosomes (Lalioti et al., 2016; Nyasae et al., 2014) (Figure 2.3; *green dashed arrows*). ATP7B is then transported with the endosomes by transcytosis to the apical membrane (Lalioti et al., 2016). It is clear that ATP7B traffics to the apical membrane upon copper elevation, however, the identity of the 'cytoplasmic vesicles' is still uncertain.

In response to copper elevation, the exposure of characteristic sequence motifs in ATP7B may trigger the binding of proteins involved in ATP7B trafficking. Sequence differences in the N-terminal region of ATP7B and ATP7A may facilitate binding of different trafficking proteins. It has been demonstrated that the TGN retention signal at low copper and apical targeting signal at high copper resides in the $F^{37}AFDNVGYE^{45}$ (F37-E45) sequence (Braiterman et al., 2008), located in the first 63 amino acids of the N-terminal region (Guo, 2005). These 63 amino acids in the N-terminal region of ATP7B are absent in ATP7A. This may explain why ATP7A migrates to the basolateral membrane, while ATP7B trafficks to the apical membrane upon copper elevation in polarized cells (Lutsenko et al., 2007).

2.2 Copper-transporting ATPase ATP7B

2.2.1 Structural organization and mechanism of copper transport

ATP7A and ATP7B are P_{1B}-type ATPases that use the energy of ATP hydrolysis to transport copper across the cell membrane. ATP7A and ATP7B are large membrane proteins with a 56% sequence identity and a molecular weight of approximately 180 kDa and 165 kDa, respectively. The structures for ATP7A or ATP7B have not been determined, but homology models from bacterial Cu^+-ATPases (Gourdon et al., 2011) and other P-type ATPases (Toyoshima, et al., 2000; Apell, 2004) have provided structural and mechanistic insights into these transporters.

ATP7A and ATP7B consist of eight transmembrane helices and four distinct cytosolic modules: the N-terminal region, actuator domain (A-domain), ATP-binding domain (ATP-BD), which is composed of the phosphorylation (P-domain) and nucleotide-binding domain (N-domain), and a small C-terminus (Figure 2.4A). Except for P-domain, the structures for all the individual cytosolic domains in ATP7B have been determined. The N-domain is composed of six-stranded antiparallel β-sheets with two α-helical hairpins on each side of the β sheet (Figure 2.4B; *green*). Although the N-domain of ATP7B lacks sequence similarity to other P-type ATPases, the overall fold of this domain is highly conserved (Dmitriev et al., 2006). This demonstrates that the basic structural features of the domain have been conserved across evolution to perform the essential function of binding ATP. The A-domain of both ATP7A and ATP7B is composed of seven antiparallel β-sheets and two helices (Figure 2.4B; *magenta*). The

β-sheets form a double-stranded beta-alpha fold with two helices protruding outward (Banci et al., 2009b) (Figure 2.4B; *magenta*).

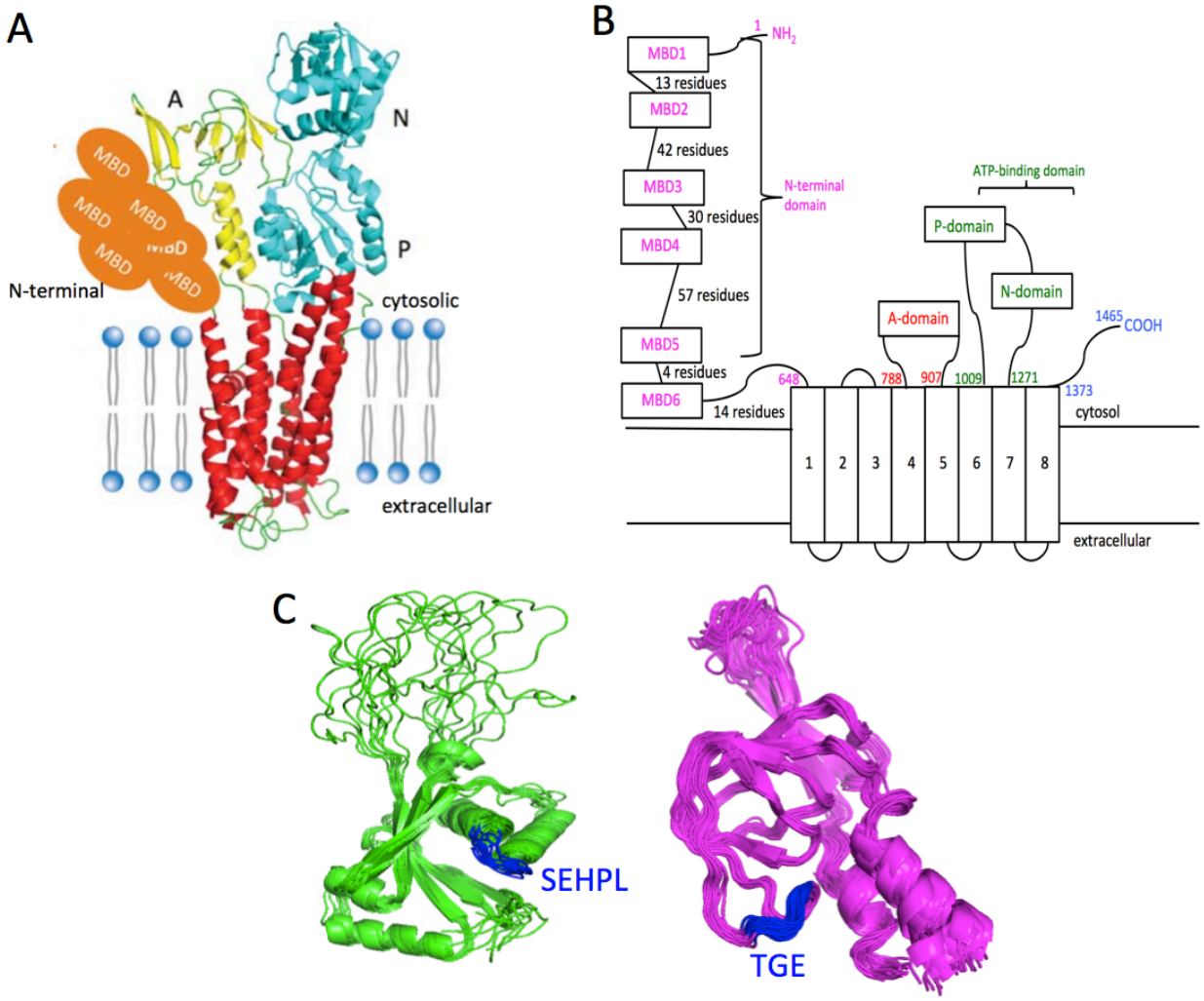

Figure 2.4: Domain architecture of ATP7B. (A) Homology model of ATP7B showing the metal-binding domains (*orange*), actuator domain (*yellow*), ATP-binding domain (*P- and N-domains; cyan*), and the transmembrane helices (*red*) (Schushan et al., 2012). (B) Linear structure of ATP7B indicating domain boundaries and linker lengths between MBDs. (C) Solution structures of the nucleotide-binding (*green*) (Dmitriev et al., 2006) and actuator domain (*magenta*) (Banci et al., 2009b). The highly conserved sequences involved in the catalytic cycle are labeled (*blue*).

The crystal structure of *Legionella pneumophila* CopA Cu^{+}-ATPase (LpCopA) provides mechanistic insights for copper binding in the transmembrane helices (Andersson et al., 2013; Gourdon et al., 2011). The single metal-binding domain of LpCopA was not resolved in the

crystal structure because of weak electron density (Andersson et al., 2013; Gourdon et al., 2011). This suggests that the high flexibility of the N-terminal region of ATP7B may preclude X-ray structure determination.

Similar to other P-type ATPases, ATP7B follows the Post-Albers catalytic cycle to transport copper ions across the cell membrane. The Post-Albers catalytic cycle transitions between two distinct protein conformations, E1, which binds the metal with high-affinity, and E2, the low affinity state, which releases the ion across the membrane (Albers, 1967) (Figure 2.5). Copper(I) binds to the high affinity CPC copper-binding motif located in the sixth transmembrane helix (E1). This triggers conformational changes in the cytoplasmic domains, allowing ATP to bind to the highly conserved SEHPL sequence in the N-domain (E1-ATP). A transient phosphorylated intermediate is formed when the γ-phosphate of ATP is transferred to the aspartate residue of the DKTG motif in the P-domain (E1-ADP). This phosphorylated intermediate is a key step in the catalytic cycle of all P-type ATPases. Transient phosphorylation of the P-domain induces rotational movement of the A-domain, allowing the two domains to interact with each other (E1-ADP; *black arrow*). These cytoplasmic domain movements reduce affinity of the copper-binding site in the CPC motif (E2P), which releases copper to the other side of the membrane. Subsequently, the highly conserved TGE loop protruding from the surface of the A-domain (Banci et al., 2009b) interacts electrostatically with the DKTG motif in the P-domain (Sazinsky et al., 2006). The TGE loop of the A-domain dephosphorylates the P-domain, thereby resetting the catalytic cycle of ATP7B (E2) for the next round of copper transfer across the membrane. Although copper binding to the highly conserved CPC motif is essential for copper translocation across the cell membrane, it is still unknown how copper reaches the binding site in the transmembrane region.

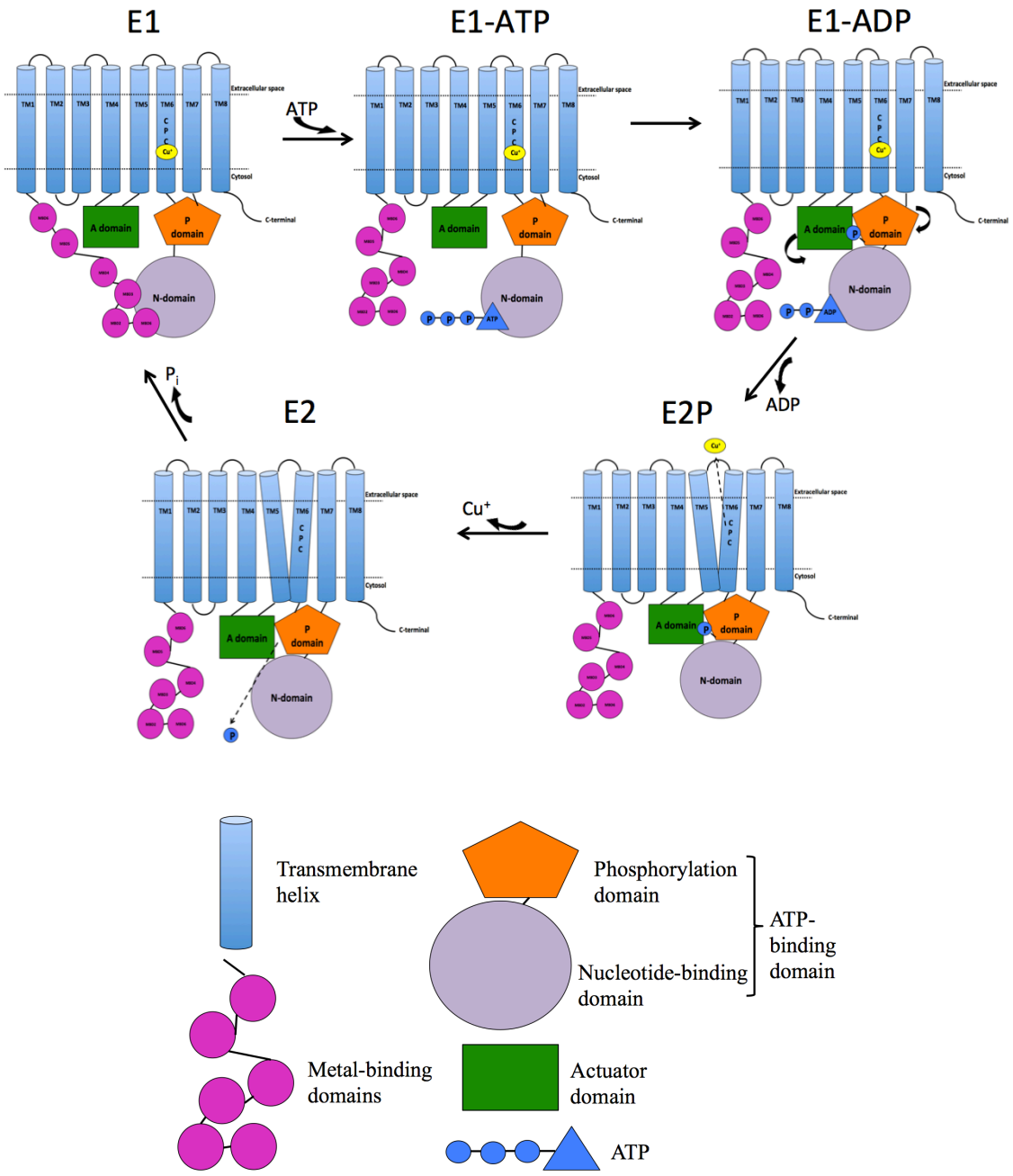

Figure 2.5: The Post-Albers catalytic cycle of ATP7B. Copper binds to the high affinity-binding site in the transmembrane region (E1). ATP binds to the N-domain (E1-ATP). The γ-phosphate of ATP is transferred to the P-domain (E1-ADP). Conformational changes in the cytoplasmic domains create a low-affinity state in the transmembrane region (E1-ADP; black arrows). Copper is released to the other side of the membrane (E2P). A-domain dephosphorylates the γ-phosphate attached to the P-domain, resetting the catalytic cycle (E2).

2.2.2 Role of the metal-binding domains

The cytosolic metal-binding domains are a characteristic feature of heavy-metal transporting ATPases. The structures of individual MBDs in the N-terminal region are highly conserved, but the number of MBDs varies from one or two in bacteria to six in humans. This may suggest a more complex regulatory function in higher order species. Each MBD is approximately 70 amino acids long, with a ferredoxin-like fold (βαββαβ), containing one copy of the signature copper-binding motif, GMXCXXC. Using biochemical (Lutsenko et al., 1997) and biophysical techniques (DiDonato et al., 2000; Wernimont, 2003), it is well established that the MBDs in ATP7B bind copper in the +1 oxidation state. Copper(I) is coordinated between the two cysteine residues in a distorted linear geometry (DiDonato et al., 2000; Ralle et al., 2004). The structures of the individual domains of ATP7B in the apo- and metal-bound forms have been solved (Achila et al., 2006; Banci et al., 2008; Dolgova et al., 2013; Fatemi et al., 2010). In the present work, we have solved the structure of MBD1 using NMR spectroscopy (PDB ID: 2N7Y) (Figure 2.6).

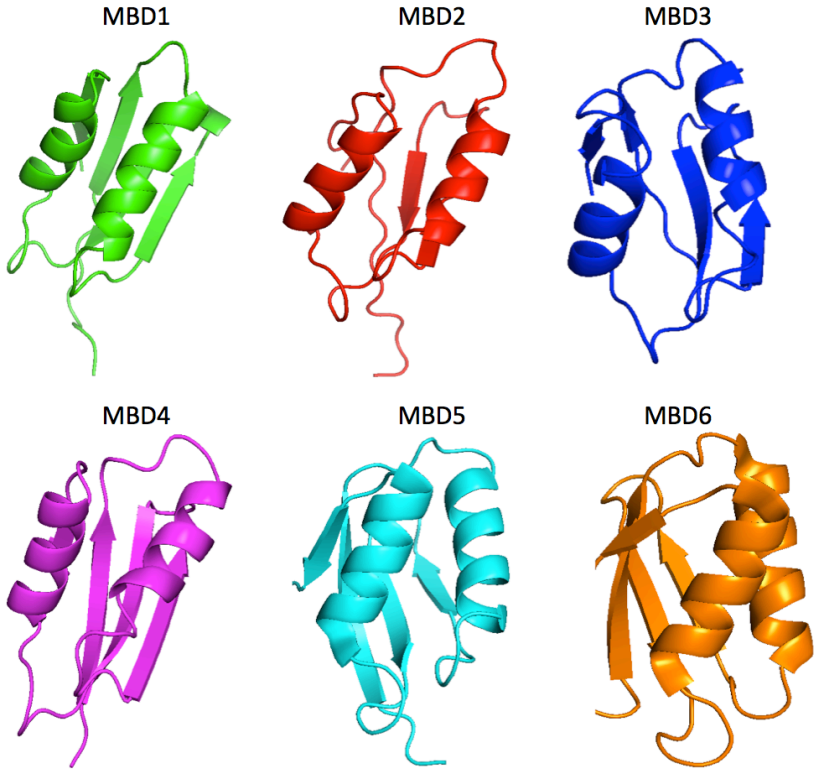

Figure 2.6: The solution structures of all of the metal-binding domains of ATP7B.

The structures of the individual MBDs have been determined, but the arrangement of the individual MBDs within the context of all six MBDs is not well characterized. Although the domain structures are similar, copper chaperone Atox1 preferentially transfers Cu(I) to MBD2 in the context of full-length MBD1-6 (Walker, 2004). Since Cu(I) coordination and affinity are all similar among the MBDs, the preferential transfer of copper to MBD2 may be caused by differences in the amino acid composition on the contact surface of MBD2 and Atox1. Electrostatic interactions between a positively charged patch on Atox1 and a negative charged surface on MBD2 recognizes and correctly orients the two domains for copper transfer (Walker, 2004). Crystal structures of dimeric Atox1 bound to Cu(I), Hg(II), and Cd(II) ions at the CxxC motif show different ligand coordination numbers (Boal and Rosenzweig, 2009a). These structures provide models that represent intermediates in the copper transfer mechanism. X-ray absorption spectroscopy demonstrates that all of the MBDs bind Cu(I) between two sulfur atoms (DiDonato et al., 2000; Ralle et al., 2004). Atox1 binds Cu(I) between two sulfur atoms of the cysteine residues and a possible third exogenous sulfur ligand (Ralle et al., 2004). Ligand-exchange of the cysteine side chains between Atox1 and the MBDs is proposed to be the primary mechanism for inter-domain copper transfer (Figure 2.7). When Atox1-Cu docks to the MBD, the thiol side-chain from the cysteine residue of the MBD donates the third ligand to Atox1-Cu (Figure 2.7B). The N-terminal cysteine residue of the MBD (C18) contributes the third thiol ligand to Atox1-Cu. Once the heterodimer is stabilized by the third ligand, the sulfur bond breaks between Cu(I) and C15 from Atox1 (Figure 2.7C). A sulfur bond is subsequently formed between the C-terminal cysteine residue of the MBD (C21) and Cu(I) (Figure 2.7C). Finally, Cu(I) is coordinated between the two cysteine side-chains in the MBD (Figure 2.7D).

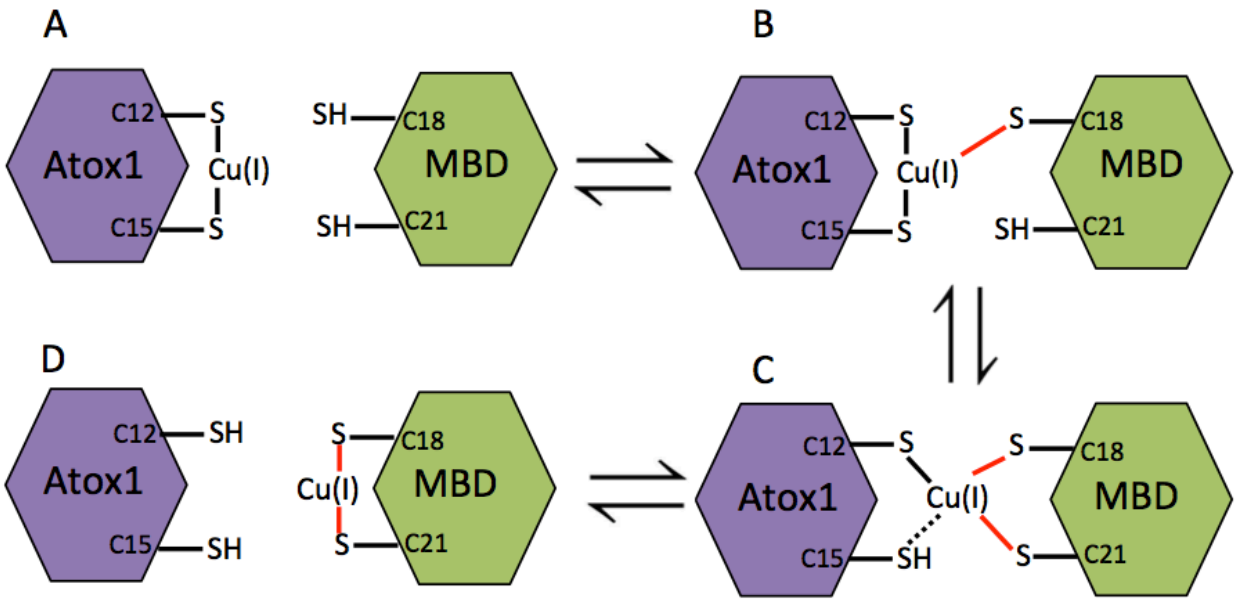

Figure 2.7: The ligand-exchange mechanism for inter-domain copper transfer.

Biochemical studies using site-directed mutagenesis and complementation analysis of various MBD constructs suggest a functional difference between the six MBDs in ATP7B, despite structural similarities between all MBDs. Amino acid sequence analysis has revealed an unusually long linker between MBD4 and MBD5, suggesting two distinct functional groups, one comprising MBD1-4 and the other MBD5-6. Mutational studies have demonstrated that MBD5 or MBD6, the domains closest to the transmembrane helices, are critical for the transport of copper and trafficking of ATP7B (Cater et al., 2004). The first three MBDs were not able to functionally replace MBD4-6, which confirms that the individual MBDs are not functionally equivalent (Cater et al., 2004). MBD1-4 have been suggested to regulate copper transport and trafficking of ATP7B by affecting the accessibility of copper to MBD5 and MBD6 (Huster, 2003). This copper accessibility could be regulated by the interaction of the N-terminal region with ATP-BD (Tsivkovskii et al., 2000). Copper binding to the MBDs decreased the domain-domain interaction with ATP-BD (Tsivkovskii et al., 2000). ATP-BD subsequently binds ATP and initiates the copper transport cycle (Tsivkovskii et al., 2000). Caution must be taken, however, when examining the function of MBDs using MBD deletion constructs, as the absence of specific individual domains may affect the overall fold and function of the entire N-terminal region.

Although extensive functional and structural work has been done with the individual MBDs, the conformation and dynamics of the N-terminal region containing all MBDs are not well characterized. NMR studies using various deletion constructs have also suggested extensive flexibility between the MBDs (Achila et al., 2006; Fatemi et al., 2010). This dynamic mobility may be important for the function of the N-terminal region by facilitating domain-domain interactions and promoting copper transfer to MBD5 or MBD6. The sharp resonances in the ^{1}H-^{15}N HSQC spectrum of MBD1-6 is indicative of a high degree of independent tumbling for the MBDs, suggesting that MBD1-6 has a "beads-on-a-string" conformation (Banci et al., 2009a; Fatemi et al., 2010). However, biochemical studies show that mutations in MBD2 or MBD3 affect copper binding to other MBDs (LeShane et al., 2010). This suggests that inter-domain interactions are important for the regulation of copper transport and trafficking activity of ATP7B (LeShane et al., 2010). Thus, one of our goals was to identify that transient interactions between a specific group of MBDs provide a mechanism for the regulation of ATP7B copper transport and trafficking activity.

2.2.3 Menkes and Wilson disease

Menkes disease (MNKD) is an X-linked recessive disorder caused by mutations in the ATP7A gene. As dietary copper is absorbed, it is transported into the intestinal cells through the apical membrane by hCtr1. ATP7A is localized to the basolateral membrane of intestinal cells and transports copper to the portal blood circulation (Peña et al., 1999). Deleterious mutations in the ATP7A gene inactivate the copper transporter (Figure 2.8). This results in copper accumulation in the enterocyte, which leads to a copper deficiency to peripheral tissues. The lack of copper in the blood renders important copper-dependent enzymes non-functional. For example, peptidylglycine α-amidating monoxygenase (PAM) requires copper as a cofactor to catalyze the conversion of neuropeptides into the active α-amidating peptide form, while tyrosinase requires copper for proper development of skin pigmentation (Lutsenko et al., 2007). Abnormal skin pigmentation and connective tissue disorders are common symptoms for MNKD patients. Disease symptoms present from two to three months of age and, if left untreated, infantile neurological problems and death occur very quickly (Kaler, 2011). Currently, there is no effective treatment option for MNKD, but lifelong subcutaneous and intramuscular copper-

histidine injections have shown to delay severe neurodegeneration and may enhance survival in infants (Kaler, 2011).

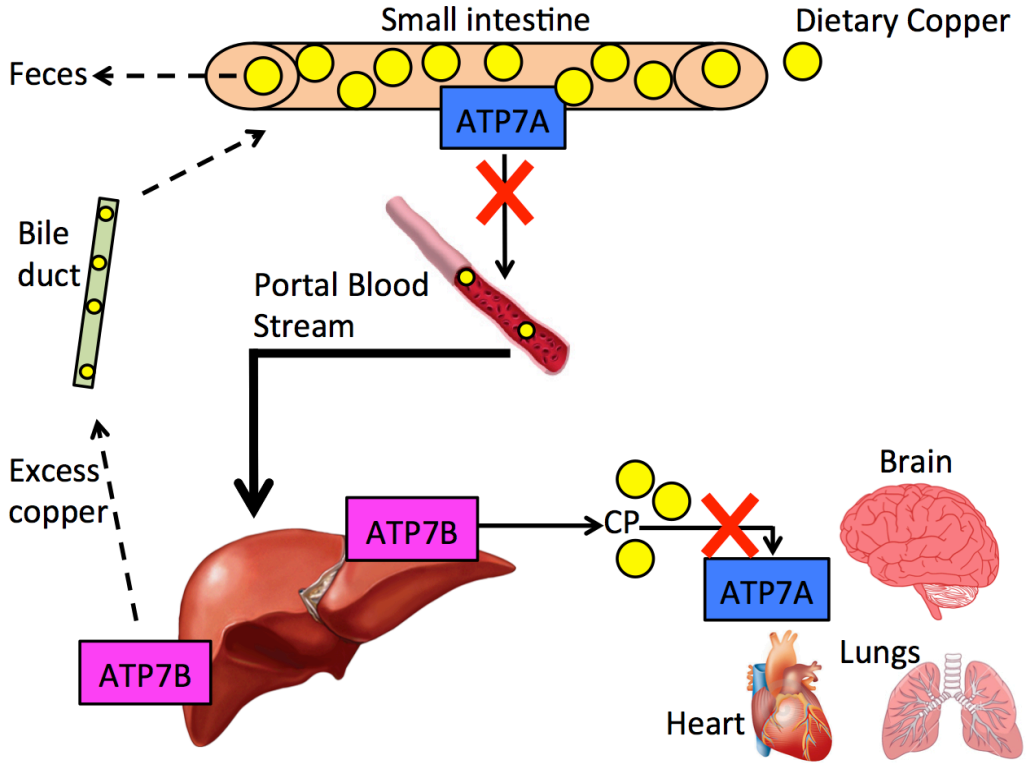

Figure 2.8: Copper distribution in the body of patients with Menkes disease. Dietary copper (*yellow spheres*) is absorbed in the small intestine. Non-functional ATP7A blocks copper transport into the blood circulation, resulting in copper accumulation in the enterocyte. This leads to a copper-deficiency to peripheral tissues. If residual copper is present in the bloodstream, it cannot be transported into tissues that express ATP7A such as the brain, heart, and lungs.

Wilson disease (WD) is an autosomal recessive liver disorder caused by mutations in the ATP7B gene. The lack of copper excretion into bile and defective copper transport into the peripheral blood circulation results in severe copper toxicity (Figure 2.9). The liver and kidneys are the organs that are primarily affected by copper toxicity (Lutsenko et al., 2007). There are a multitude of disease-causing mutations that affect different regions of ATP7B, but the most common mutations are located within the nucleotide-binding domain (N-domain) (Kenney and Cox, 2007) (Figure 2.10). In particular, the H1069Q is the most common mutation, found in approximately 38% of WD patients (Shah et al., 1997). Using solution NMR, the H1069Q mutation has been demonstrated to disrupt tight binding of ATP (Dmitriev et al., 2006). Depending on the mutation, there are other mechanisms that can inactivate ATP7B activity, such

as decreased protein stability (Braiterman et al., 2011), mislocalization (Gupta et al., 2011), and protein truncation (Braiterman et al., 2011). If left untreated, this toxic accumulation results in severe liver disease and eventual death (Schilsky, 2002). Currently, copper chelating agents and zinc therapy are effective treatment options for Wilson disease (Schilsky, 2002). Copper chelating agents such as D-penicillamine, trientine, and tetrathiomolybdate mobilize copper and facilitate its excretion, whereas zinc induces the synthesis of metallothioneins, which sequester copper (Schilsky, 2002).

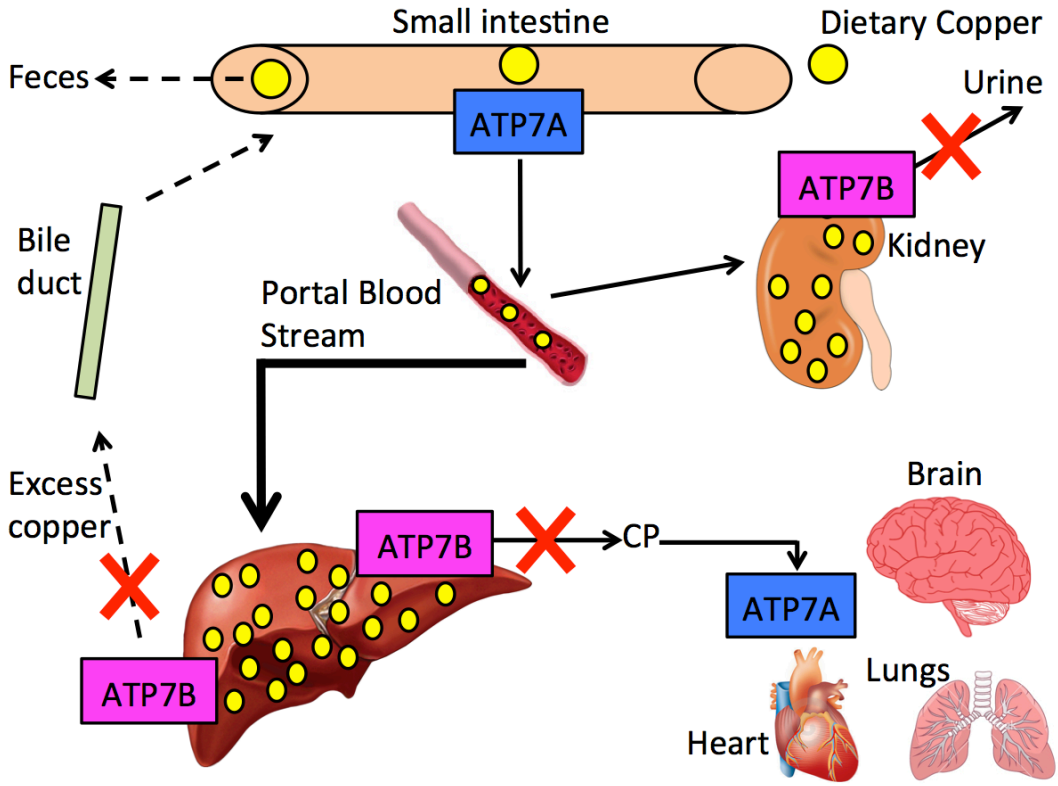

Figure 2.9: Copper distribution in the body of patients with Wilson disease. Dietary copper (*yellow spheres*) is absorbed in the small intestine. ATP7A exports copper from the enterocyte into the blood circulation. Copper-bound to serum proteins are transported primarily to the liver and kidneys. Non-functional ATP7B blocks copper excretion into the bile and prevents copper-incorporation into copper-dependent enzymes such as ceruloplasmin and albumin for peripheral blood circulation.

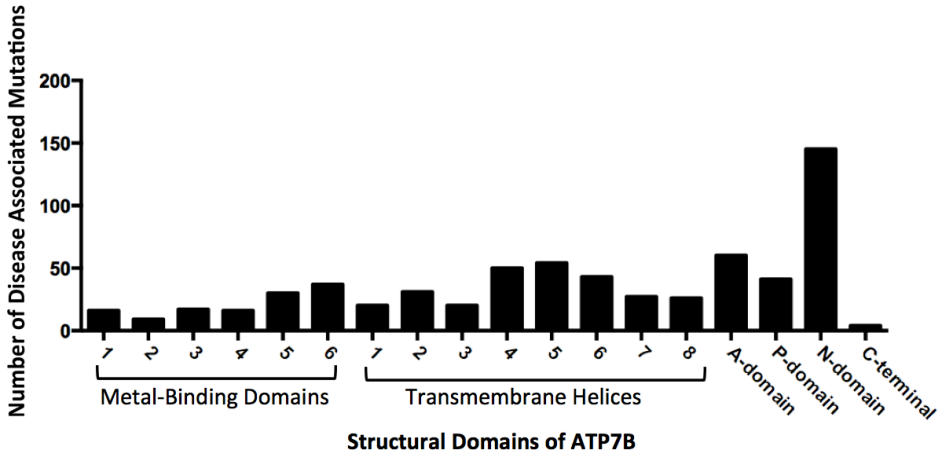

Figure 2.10: Domain distribution of Wilson disease mutations.

2.3 Cisplatin and its mechanism of action

Although ATP7B is involved in maintaining copper homeostasis in the body, overexpression of ATP7B is associated with tumor resistance to cisplatin during chemotherapy. Cisplatin (*cis*-diamminedichloroplatinum, DDP) is a widely used drug for treating testicular, ovarian, stomach, and bladder cancers. It is an effective cancer treatment option, but intrinsic and acquired resistance to DDP are severe problems in cancer chemotherapy. Although the mechanisms of DDP resistance are diverse, there is a strong correlation between DDP resistance and the amount of ATP7B in the cell. To combat DDP resistance, next generation DDP analogs, which include carboplatin and oxaliplatin, have been developed (Figure 2.11). Understanding the mechanisms of DDP resistance will allow strategies to be developed to increase the effectiveness of DDP against specific cancer cells while reducing cell toxicity.

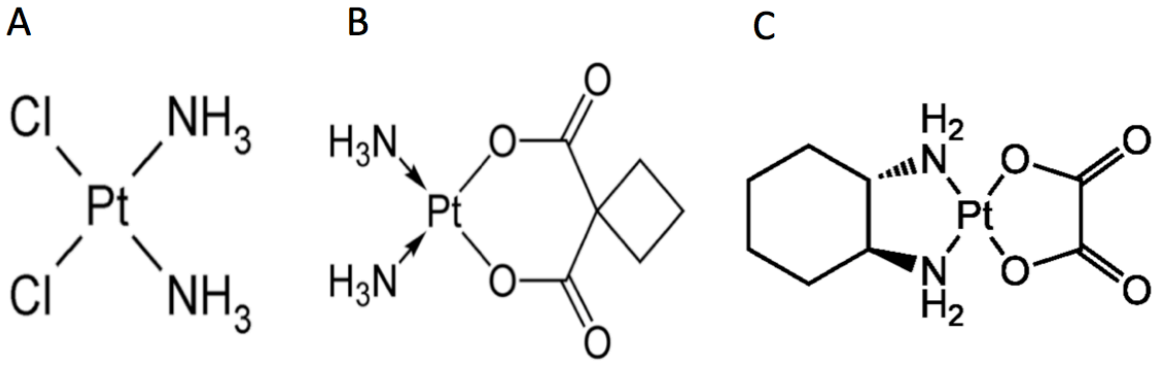

Figure 2.11: Chemical structure of platinum-based drugs. (A) Cisplatin. (B) Carboplatin. (C) Oxaliplatin.

Cisplatin is a neutral, planar Pt(II) complex with two chloride and two ammine ligands oriented in *cis*-configuration (Jamieson and Lippard, 1999). When DDP is intravenously injected into the bloodstream, high chloride concentrations (100 mM) suppress aquation and DDP remains in a neutral state (Figure 2.12). DDP was previously thought to enter the cell by passive diffusion (Binks and Dobrota, 1990). More recent evidence, however, demonstrates that DDP enters the cell by passive transport through hCtr1 (Ishida et al., 2002). Upon entry into the cell, diminished chloride concentrations (20 mM) quickly promote aquation of the first Cl^- ligand. This creates a positively charged intermediate that can form mono-functional platinum adducts with DNA and proteins (Figure 2.12; *purple arrow*). Bi-functional platinum adducts with DNA and proteins can also be formed when aquation of the second Cl^- ligand is induced (Figure 2.12; *green arrow*).

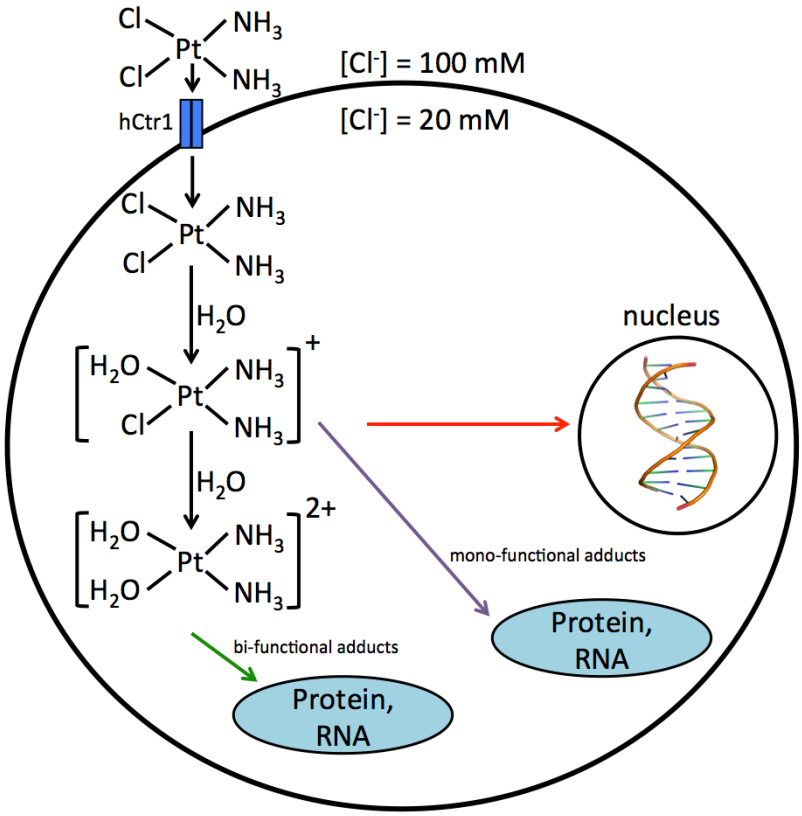

Figure 2.12: Cisplatin reaction chemistry in the cell. When cisplatin enters the cell, it forms a positively charged intermediate that can readily bind to DNA (*red arrow*) and other cellular components (*purple arrow*). When cisplatin loses its second chloride ligand, bi-functional adducts can be formed with other proteins and RNA (*green arrow*).

DDP functions by primarily reacting with DNA in the cell nucleus (Figure 2.12; *red arrows*). DDP binds at the N-7 position of guanine, forming 2-d(GpG) intrastrand crosslinks, which is the most common cisplatin-DNA adduct (Figure 2.13). However, other intra- and inter-strand DNA crosslinks are also present (Fichtinger-Schepman and Van der Veer, 1985). Based on the structures of different cisplatin-DNA adducts, cisplatin binding unwinds and destabilizes the DNA, which creates various DNA distortions near the platination site (Cohen et al., 1979; Coste et al., 1999; Gelasco and Lippard, 1998). These crosslinks prevent DNA transcription and replication, which is particularly effective against rapidly dividing cancer cells. The structural distortions caused by cisplatin binding signals DNA damage and eventually induces apoptosis through various biochemical reactions (Bellacosa, 2001; Nehmé et al., 1997). Although cisplatin is very effective against certain types of cancers, intrinsic and acquired resistance limits its effectiveness.

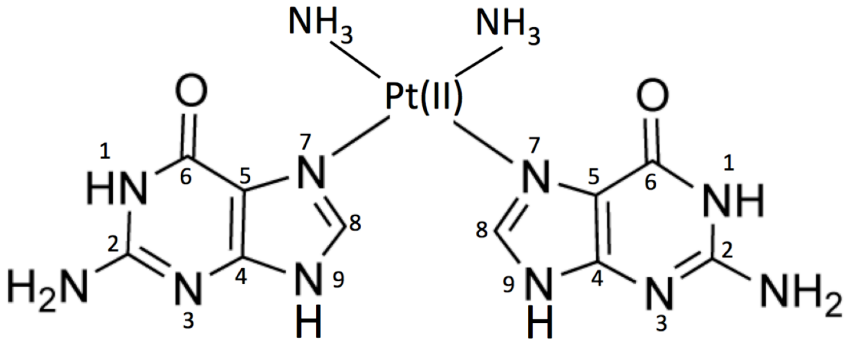

Figure 2.13: Cisplatin binding to DNA forms 1,2-d(GpG) intrastrand crosslinks.

2.4 Copper-transport proteins contribute to the multifactorial mechanism of cisplatin resistance

Cisplatin binds to and reacts with different cellular components, giving rise to multiple pathways of cisplatin resistance in the cell. There are four broad categories for cisplatin resistance, which include reduced cisplatin uptake, drug detoxification in the cytosol, accelerated efflux of cisplatin out of the cell, and increased DNA repair (Figure 2.14).

DNA is the primary target for cisplatin binding (Figure 2.14; *blue arrow*). Effective DNA repair mechanisms are required for preventing the formation of DNA-platinum adducts. The nucleotide excision repair (NER) system is primarily responsible for repairing DNA lesions

and has been shown to be associated with cisplatin resistance (Jung and Lippard, 2007). At a platinum lesion, stalled RNA polymerase II acts as a signal to recruit different NER proteins. After a complex of DNA repair proteins are formed, helicases unwind the double-stranded DNA, and an endonuclease excises 24-32 nucleotides in which the platinum lesion is located (Jung and Lippard, 2007). It was demonstrated that xeroderma pigmentosum cells, which have components defective in NER is five to ten times more sensitive to cisplatin than normal fibroblast cells (Furuta et al., 2002). Additionally, a two- to three-fold increase in the mRNA levels of xeroderma pigmentosm complementation group A (XPA) was associated with cisplatin resistance in ovarian cancer cell lines (States and Reed, 1996). XPA is a key component in the NER pathway that recognizes DNA lesions (States and Reed, 1996).

Elevated levels of intracellular glutathione have also been associated with cisplatin resistance (Figure 2.14; *orange arrow*). Binding of cisplatin to gluthathione forms Pt-$(GS)_2$ complexes (Ishikawa and Ali-Osman, 1993). These complexes prevent platinum from reaching the nucleus and reacting with DNA. Additionally, Pt-$(GS)_2$ can also be actively transported out of the cell by the GS-X pump (Kurokawa et al., 1995). A two-fold increase in the concentration of GSH inside the cell increases the GS-X pump activity, resulting in decreased cisplatin accumulation (Kurokawa et al., 1995).

Different cisplatin resistance mechanisms mediated by various copper transport proteins have been proposed. The passive copper transporter, hCtr1, was demonstrated to mediate the uptake of cisplatin into the cell (Figure 2.14; *green arrow*) (Ishida et al., 2002). By deleting the *CTR1* gene in both yeast and mouse cell lines, a decrease in cisplatin accumulation was observed (Ishida et al., 2002). This decreased cisplatin-DNA adduct formation and increased cisplatin resistance. However, the precise mechanism for cisplatin uptake by hCtr1 is still unknown. Since cisplatin has a larger diameter than Cu(I), it may be not transported directly through the hCtr1 channel. Rather, cisplatin may bind to extracellular motifs at the plasma membrane and trigger hCtr1 internalization by macropinocytosis (Figure 2.14; *pink arrow*) (Holzer and Howell, 2006). The distinct copper and cisplatin uptake mechanisms of hCtr1 have been supported by fluorescence resonance energy transfer (FRET) experiments (Sinani et al., 2007). It was

demonstrated that specific Ctr1 mutants defective in copper transport enhanced cisplatin accumulation, whereas a copper transport active mutant did not accumulate cisplatin.

The copper chaperone Atox1 was demonstrated to mediate cisplatin resistance using different mechanisms. The deletion of Atox1 decreased cisplatin influx by preventing macropinocytosis and internationalization of hCtr1 (Safaei et al., 2009). It was suggested that the direct interaction of Atox1 with the C-terminal region of hCtr1 facilitates the polyubiquitination of hCtr1, resulting in the degradation of the copper transporter (Safaei et al., 2009). Therefore, reduced Atox1 expression levels in specific cancer cells may lead to cisplatin resistance. Additionally, structural studies have demonstrated that cisplatin binds to the CxxC copper-binding motif in Atox1 (Boal and Rosenzweig, 2009b; Palm et al., 2011). Cisplatin-induced unfolding of Atox1 was observed *in vitro* at a high cisplatin to protein ratio, which is unlikely to exist in the cell (Palm et al., 2011). The unfolding of Atox1 caused by cisplatin binding would stop cisplatin transport in the cytoplasm and prevent platinum from entering the nucleus to exert its toxic effect. Lastly, our studies have demonstrated that cisplatin can hijack the Atox1 copper transport pathway (Dolgova et al., 2013). Similarly to copper, Atox1 can bind and transfer cisplatin to the MBDs of ATP7B (Figure 2.14; *purple arrow*) (Dolgova et al., 2013). This Atox1-ATP7B interaction may be an important pathway for cisplatin detoxification in the cell.

Copper transporter ATP7B has also been associated with tumor resistance to cisplatin (Figure 2.14; *red arrow*). It was demonstrated that cells with higher expression levels of ATP7B were resistant to cisplatin chemotherapy (Komatsu et al., 2000; Nakayama et al., 2002; 2004). The mRNA levels of ATP7B were also elevated in oral squamous carcinoma resistant cell lines (Yoshizawa et al., 2007). In the same cell line, there was no correlation between cisplatin resistance and the expression levels of other copper proteins (Yoshizawa et al., 2007). Interestingly, the silencing of ATP7B using siRNA increased cisplatin cytotoxicity by 10-fold in resistant cells (Yoshizawa et al., 2007). The active transport of platinum across the cell membrane by ATP7B has been suggested to be the primary mechanism of cisplatin resistance (Safaei et al., 2007). However, low transport rates at physiological pH and high substrate

specificity of ATP7B for copper suggests that active extrusion is unlikely to be a major mechanism of cisplatin resistance *in vivo*.

An alternative mechanism to active transport involves sequestering cisplatin in the metal-binding domains of ATP7B. A previous study in our lab demonstrated that cisplatin is sequestered at the metal-binding domains (Dolgova et al., 2009). Protein expression of the first four metal-binding domains (MBD1-4) protected *E. coli* cells from the toxic effects of cisplatin (Dolgova et al., 2009). MBD1-4 was entirely cytosolic demonstrating that active transport is not required for cisplatin resistance associated with ATP7B. One of our goals in this thesis was to investigate the mechanism of cisplatin detoxification by the metal-binding domains of ATP7B.

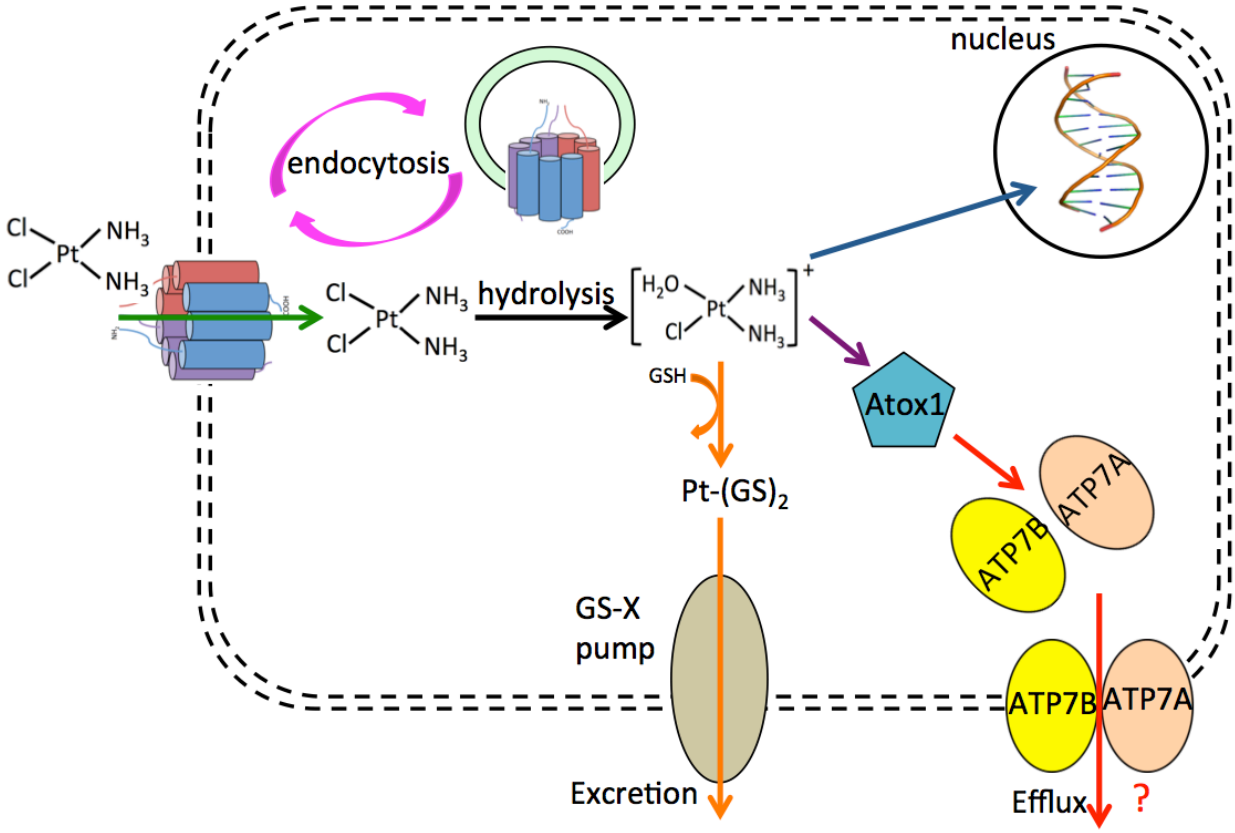

Figure 2.14: Proposed mechanisms of cisplatin resistance. Cisplatin enters the cell through hCtr1 either by facilitated diffusion through the transmembrane pore (*green arrow*) or by macropinocytosis (*pink arrows*). When cisplatin enters the cytosol, it can bind to different acceptors. Cisplatin binding to glutathione forms Pt-$(GS)_2$ complexes that can be excreted out of the cell by the GS-X pump (*orange arrows*). Atox1 also binds cisplatin (*purple arrow*) and delivers platinum to ATP7A and ATP7B. A fraction of cisplatin escapes detoxification and reaches DNA in the nucleus (*blue arrow*).

2.5 Nuclear magnetic resonance spectroscopy techniques to study protein structure and dynamics of metal-binding domains

2.5.1 Heteronuclear Single Quantum Coherence (HSQC)

Nuclear magnetic resonance (NMR) spectroscopy is a powerful method for studying the structure and dynamics of proteins. Advancements in magnet design, pulse sequences, isotopic labeling, and data processing computer software packages make it more efficient to solve the structures of smaller proteins, such as the metal-binding domains of ATP7B, by NMR. NMR is also an effective method for determining the metal-binding sites and contact surfaces of multi-domain proteins by chemical shift perturbation analysis. More importantly, however, NMR is the most powerful method for studying protein dynamics. Protein dynamics have provided functional insights into the highly mobile N-terminal region of ATP7B. Understanding the conformation of the N-terminal region has helped us identify a specific group of MBDs that function in the regulation of ATP7B copper transport and trafficking activity.

NMR relies on the magnetic properties of individual nuclei for studying and solving three-dimensional protein structures at atomic resolution. Spin is a quantum property that is related to the intrinsic angular momentum of a nucleus and is described by the quantum number *I*. However, in order for a nucleus to be NMR detectable, it must have a non-zero value of *I*. Typically, the nuclei used in protein structure determination have a spin of ½. These isotopes include ^{1}H, ^{15}N, and ^{13}C. Since the natural abundance of ^{15}N and ^{13}C is low, isotopic enrichment is typically used for protein NMR studies.

Similar to other forms of spectroscopy, NMR relies on a transition between two different energy states, a ground and an excited state. In an external magnetic field (B_0), the magnetic moment of a nucleus ($I = ½$) will either orient parallel or anti-parallel to B_0, which corresponds to a lower or higher energy state, respectively (Figure 2.15). The spin population difference between the energy states is given by the Boltzmann distribution. A slight excess of spins will be oriented parallel to the B_0 field, which creates a net magnetization (M_o) vector along the B_0 field (Figure 2.15A). A radiofrequency (RF) pulse is applied to induce the transition of the nuclei from the ground to higher energy states. When the M_0 vector rotates from the z-axis onto

the x-y plane, the net magnetization vector gives rise to an observable NMR signal (Figure 2.15B). The free induction decay (FID) is the time-dependent NMR signal that reflects the resonance frequency of a nucleus (Figure 2.15C).

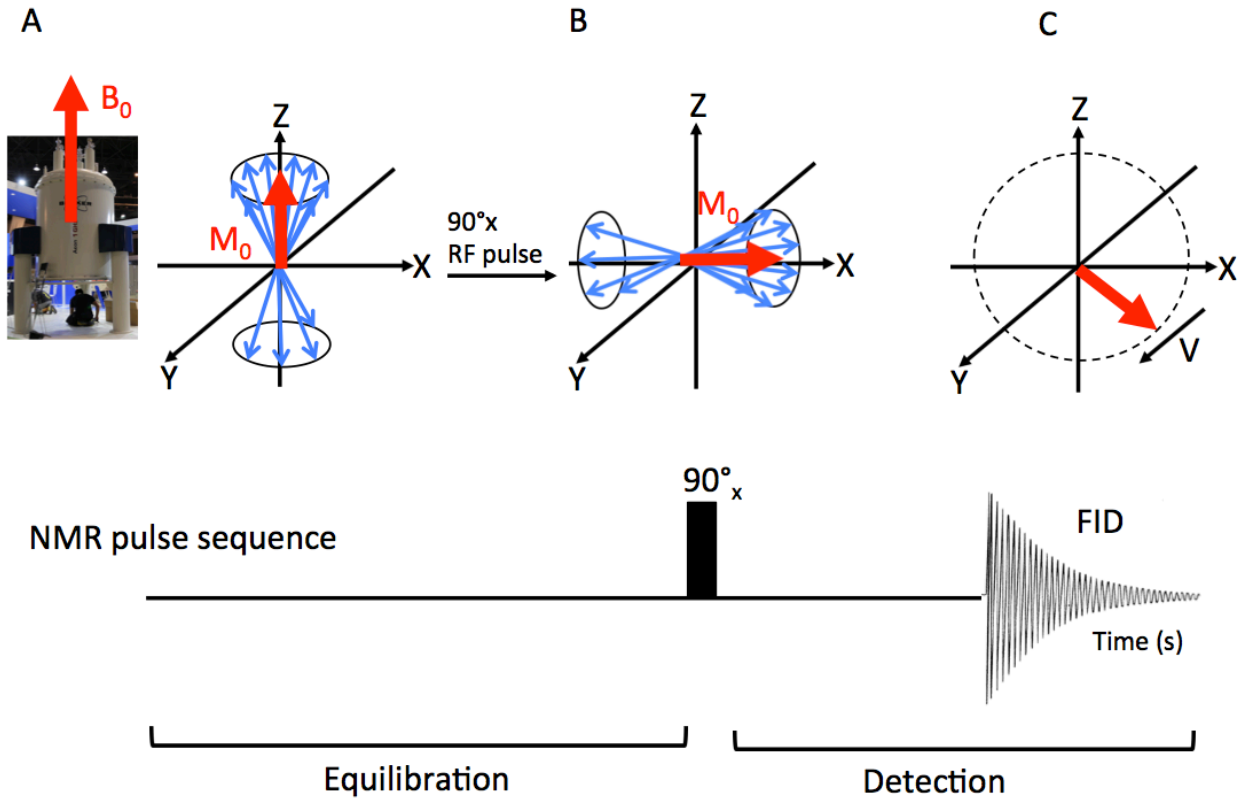

Figure 2.15: The effect of an external magnetic field on an ensemble of spins. (A) At equilibrium, there is a slight excess of spins in the low energy state, causing the magnetization vector to orient parallel with the B_0 field. (B) An RF pulse rotates the spins onto the x-y plane. (C) After the RF pulse is applied, the spins precess around the x-y plane in a time-dependent manner. The frequency of an individual nuclei precessing around the x-y plane is recorded as an FID.

The absorption of energy by a particular nucleus is dependent on a characteristic precession frequency, also known as the Larmor frequency:

$$\omega_0 = -\gamma B_0, \tag{2.4}$$

where ω_0 is the resonance frequency of a nucleus, γ is the gyromagnetic ratio, and B_0 is the strength of the external magnetic field. The gyromagnetic ratio (γ) is defined by the ratio of the magnetic moment of the nucleus to its angular momentum. This reflects the strength of the NMR signal for a particular type of nucleus. Nuclei in proteins are subject to different electron density configurations, which change the effective magnetic field the nucleus experiences in the

external magnetic field. This changes the resonance frequency for each chemically distinct nucleus:

$$\omega = -\gamma(B_0 - B_i), \tag{2.5}$$

where ω is the specific resonance frequency of a nucleus, B_0 is the strength of the external magnetic field, and B_i is the change in magnetic field. This difference in resonance frequency between the nuclei is called the chemical shift (δ). Chemical shift is measured in parts per million (ppm) and compares the resonance frequency of a nucleus (υ_{sample}) to the resonance frequency of a well-established standard (υ_{ref}):

$$\delta \text{ (ppm)} = \frac{\upsilon_{sample} - \upsilon_{ref}}{\upsilon_{ref}} \times 10^6 \tag{2.6}$$

The chemical shift scale is independent of the external magnetic field, which allows direct comparison between spectra recorded at different magnetic field strengths.

The most routinely used experiment in protein NMR is the 2D ^{1}H, ^{15}N-heteronuclear single quantum coherence (HSQC). The 2D ^{1}H-^{15}N HSQC spectrum is often considered the NMR fingerprint of a protein because each spectrum shows the signal from a backbone amide group, or a side chain group of glutamine, asparagine, arginine, or tryptophan in the protein sequence (Figure 2.16). Protons have very high sensitivity because of the much larger gyromagnetic ratio than ^{15}N. Therefore, to maximize the sensitivity of the ^{15}N signal, magnetization is transferred from ^{1}H to ^{15}N by an NMR technique called polarization transfer (Morris and Freeman, 1979). Magnetization is subsequently transferred from ^{15}N back to ^{1}H to maximize signal detection sensitivity. The 2D ^{15}N-HSQC spectrum is often suitable for smaller proteins, but the resolution is often not sufficient for larger proteins (>25 kDa).

The transverse relaxation optimized spectroscopy (TROSY) technique is often used for recording the spectra of larger proteins. The information content is identical to the HSQC, except that TROSY has improved spectral resolution. In a backbone amide group, the hydrogen and nitrogen atoms are J-coupled. J-coupling is the interaction of two nuclei mediated through electrons in the chemical bonds. Nuclei that are J-coupled should produce four peaks in the HSQC spectrum (Figure 2.17A). In a typical ^{1}H, ^{15}N-HSQC spectrum (Figure 2.16), decoupling is applied during detection, which merges four peaks into one single peak (Figure 2.17B). The

TROSY technique specifically selects for the multiplet component with the narrowest linewidth (Figure 2.17C). As a result, the TROSY technique is particularly advantageous for large proteins with significant peak overlap.

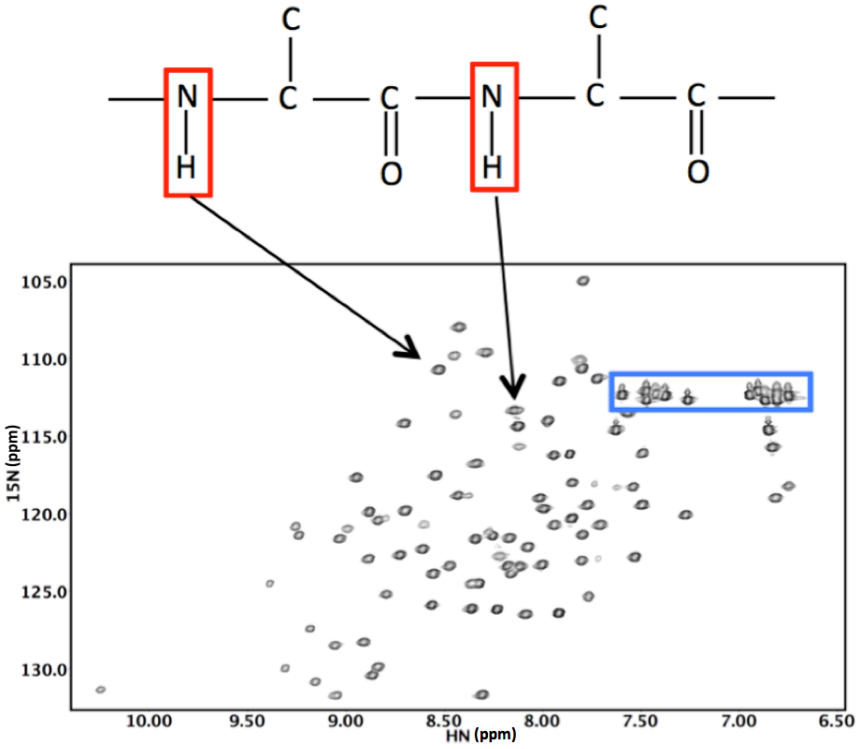

Figure 2.16: ^{1}H, ^{15}N-HSQC spectrum of MBD1. Each peak in the spectrum corresponds to a unique backbone amide group or a side chain amide group of glutamine, asparagine, arginine, or tryptophan in the protein sequence (*blue square*).

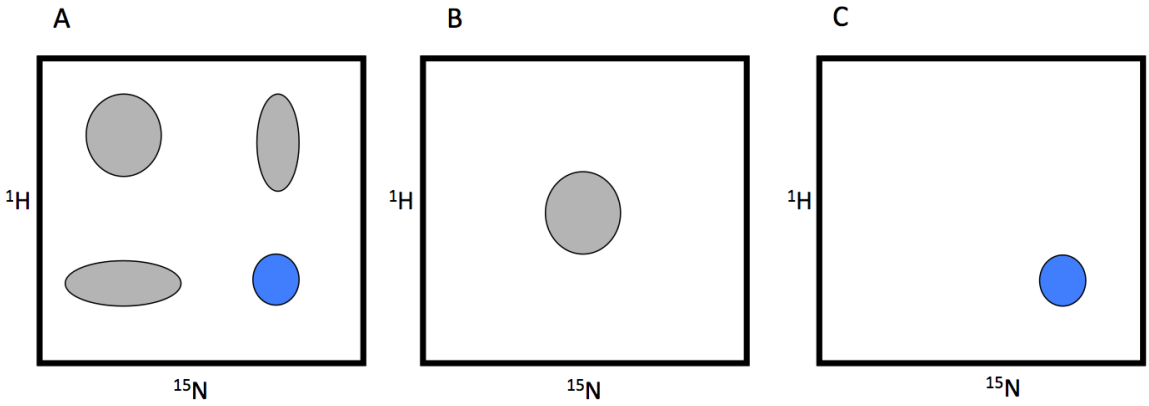

Figure 2.17: The difference between an HSQC or TROSY experiment on an NMR signal. ^{1}H, ^{15}N spectra for one residue in a (A) non-decoupled HSQC, (B) decoupled HSQC and (C) TROSY.

2.5.2 NMR relaxation

Relaxation is a fundamental process where the excited nuclear spins return to their equilibrium state. NMR relaxation is induced by the interaction and fluctuation of local magnetic fields. Relaxation is used in different aspects of NMR spectroscopy such as transfer of magnetization to nearby atoms and protein dynamics. The two mechanisms of NMR relaxation are longitudinal (R_1) and transverse (R_2) relaxation. The relaxation rates are the inverse of the relaxation times according to the equations:

$$R_1 = 1/T_1 \text{ and } R_2 = 1/T_2. \tag{2.7}$$

Longitudinal (spin-lattice) relaxation releases energy to the external environment, causing the population of the nuclei in the excited state to return back to equilibrium. This relaxation process only affects the z-axis (M_z) (Figure 2.18A). Transverse (spin-spin) relaxation is a process that is caused by the magnetic fields of interacting spins. Immediately after excitation, the spins are precessing coherently in the x-y plane (Figure 2.17B). Over time, coherence is lost and the spins become dephased (Figure 2.18B; *blue arrows*). Since longitudinal relaxation restores magnetization on the z-axis (M_z) and transverse relaxation affects the magnetization vector in the x-y plane (M_{xy}), these relaxation mechanisms are treated as independent processes. The Bloch equations calculate the net magnetization of the nuclear spins under the influence of relaxation:

$$\frac{dM_z}{dt} = \frac{M_0 - M_z}{T_1} \tag{2.8}$$

$$\frac{dM_x}{dt} = -\frac{M_x}{T_2} \tag{2.9}$$

$$\frac{dM_y}{dt} = -\frac{M_y}{T_2} \tag{2.10}$$

Experimentally, T_1 determines the time required before a RF pulse can be applied to the nuclei again, whereas T_2 determines the time it takes for the signal to decay.

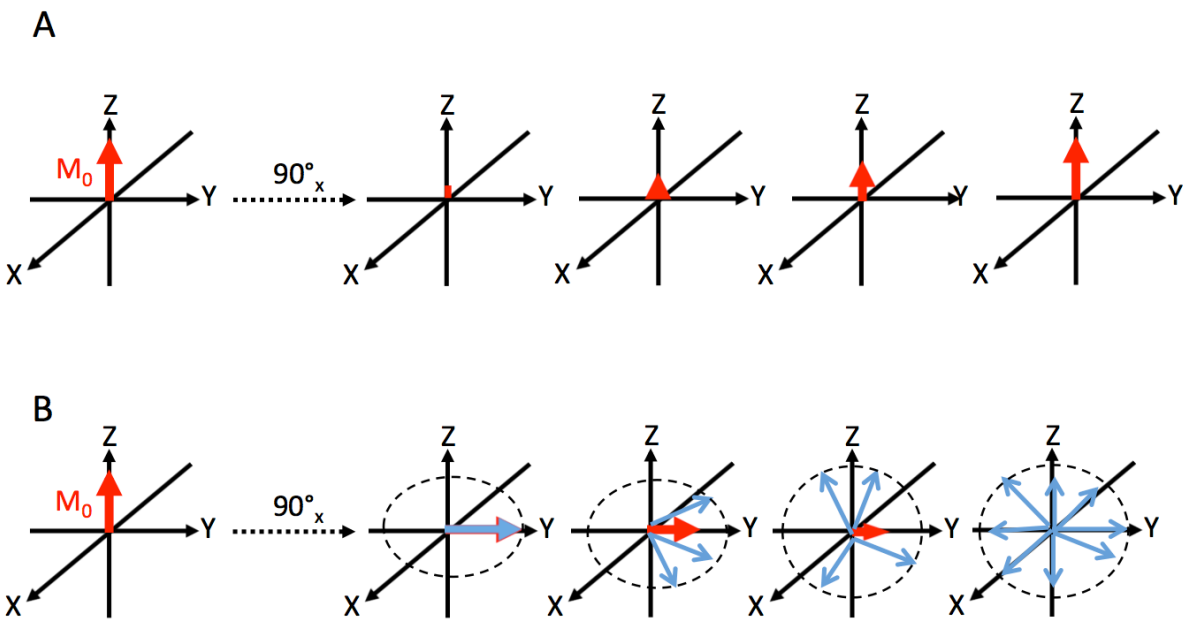

Figure 2.18: The effect of relaxation on the magnetization vectors after an RF pulse. (A) Longitudinal and (B) transverse relaxation of magnetization vectors after a 90° RF pulse.

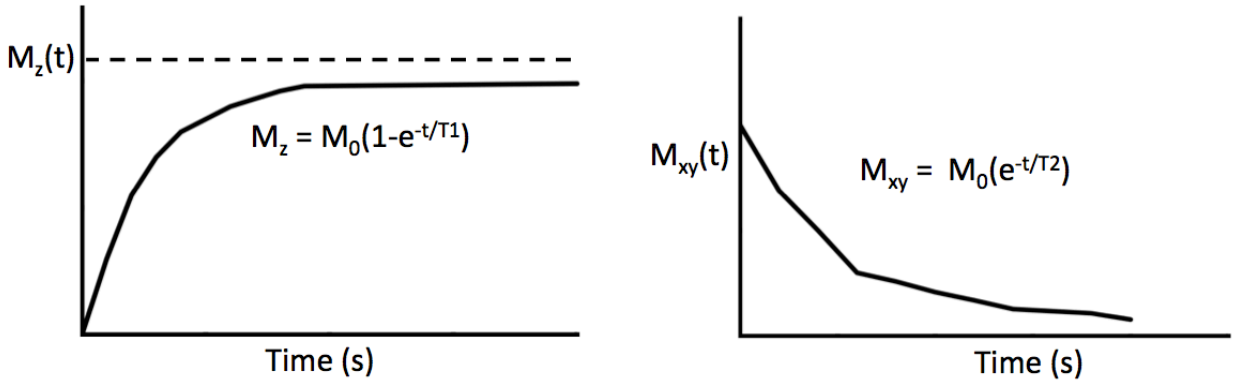

Figure 2.19: Time-dependent net magnetization for longitudinal (left) and transverse relaxation (*right*).

As molecules become larger, the transverse relaxation rate increases. After excitation, the amplitude of the FID is at a maximum because the nuclei are precessing coherently in the x-y plane. Larger proteins, however, will decay back to their equilibrium at a much a faster rate than smaller proteins (Figure 2.20). A faster transverse relaxation rate means there is less time to detect the signal, causing peaks in the spectra to broaden out and disappear. Therefore,

transverse relaxation determines the linewidth of the NMR signal and is the primary determinant of spectral resolution.

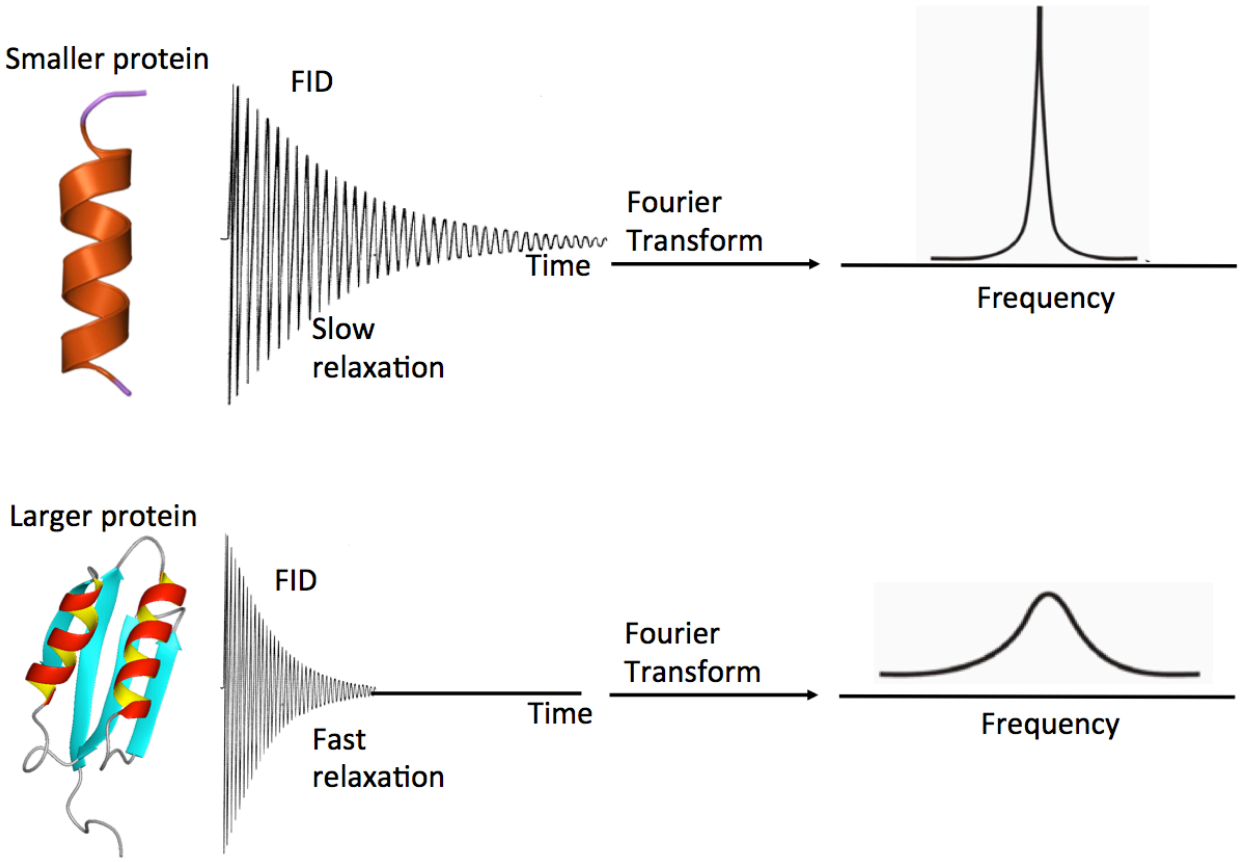

Figure 2.20: The effect of protein size on the decay rate of the FID and the resulting linewidth of a peak. Smaller proteins have slower decaying FIDs, which lead to narrow linewidths in the spectrum. The FIDs of larger proteins decay quickly, resulting in a broad peak.

NMR relaxation is dependent on molecular motion and, thus, is an accurate indicator of protein dynamics. Protein dynamics are measured from R_1, R_2, and ^1H, ^{15}N heteronuclear NOE experiments (Kay et al., 1989). The relaxation rates are obtained by fitting the exponential R_1 and R_2 decay curves from the peak volumes or intensities of the backbone amide groups, in a series of 2D ^1H-^{15}N HSQC spectra recorded with increasing relaxation delays. Since the ^1H, ^{15}N heteronuclear NOE has a defined distance between the two atoms; increased motion about the NH bond vector is measured by a decreased NOE intensity. By measuring the R_1, R_2, and heteronuclear NOE values of the backbone amide groups, the correlation time (τ_c) of the protein can be calculated (Kay et al., 1989). This represents the overall tumbling of the molecule and the calculated value is the time it takes the molecule to rotate one radian in solution.

2.5.3 Backbone and side-chain chemical shift assignments

Three-dimensional experiments are commonly used for assigning the backbone residues of proteins. These experiments require isotopic labeling with ^{15}N and ^{13}C. A 3D experiment spreads the NMR signal observed from a 2D plane (Figure 2.21A) into a 3D dataset with three correlated chemical shifts (Figure 2.21B). Separating the correlated chemical shift of ^{1}H, ^{15}N, and ^{13}C for a specific amino acid residue reduces spectral overlap and backbone assignment ambiguity. In many common backbone assignment experiments, magnetization is transferred to different backbone atoms that are connected through one or several covalent bonds (Figure 2.22).

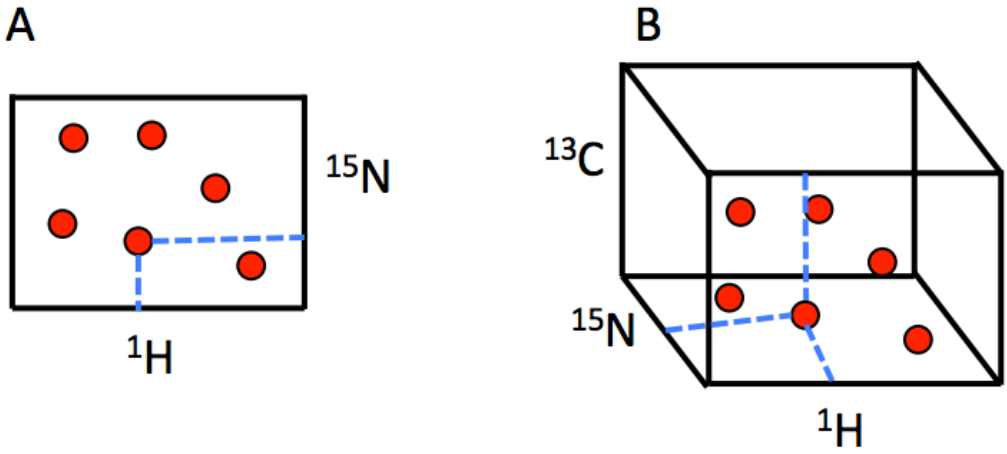

Figure 2.21: Visualization of a (A) 2D plane into a (B) 3D dataset for chemical shift assignments.

Amino acid residues are identified by connecting different spin systems from various backbone assignment experiments. Inter-residue and intra-residue connectivities can be distinguished by using these pairs of experiments: HNCO/HN(CA)CO, HNCACB/HN(CO)CACB, and HNCA/HN(CO)CA (Figure 2.22) (Gardner and Kay, 1998). For example, the HNCA experiment connects the backbone amide group to the alpha carbons of both the same ($C\alpha_i$) and the previous ($C\alpha_{i-1}$) residue in the amino acid sequence (Figure 2.23B). Using the HNCA experiment, as an example, sequential residues are assigned by connecting the $C\alpha_{i-1}$ of the current residue (K50) to the $C\alpha_i$ of the preceding residue (V49). The HNCO experiment contains carbonyl carbon chemical shifts for only the previous (i-1) residue and the HN(CA)CO experiment contains carbonyl carbon chemical shifts both the i and i-1 residue. The HN(CO)CACB experiment contains α- and β-carbons for i-1 residue and the HNCACB contains alpha and beta carbons for both the i and i-1 residues.

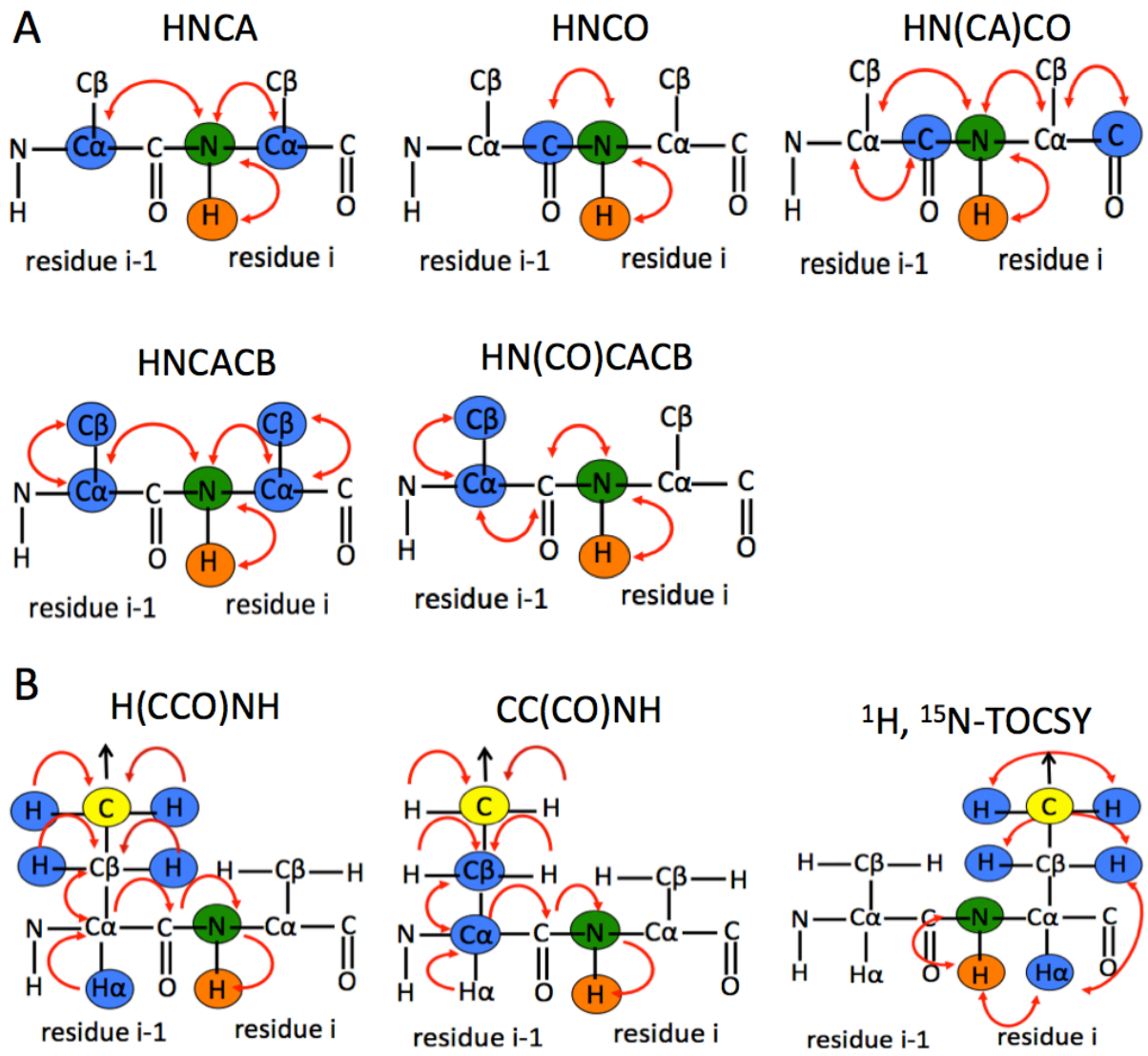

Figure 2.22: Magnetization transfer scheme for the (A) backbone and (B) side-chain assignment experiments. All the backbone 3D experiments used in our work start with magnetization transfer from the backbone hydrogen to nitrogen and then to the desired heteronucleus. Magnetization is subsequently transferred back to hydrogen along the same pathway for detection. H(CCO)NH and CC(CO)NH starts with magnetization transfer from the side-chain protons to the attached carbons, and then on to the nitrogen and backbone hydrogen. ^{1}H, ^{15}N-TOCSY starts with magnetization transfer between the hydrogen atoms. Magnetization is subsequently transferred to nitrogen then back to the hydrogen atoms for detection. For the side-chain experiments, the carbon atom (*yellow*) indicates connectivities that go beyond Cβ.

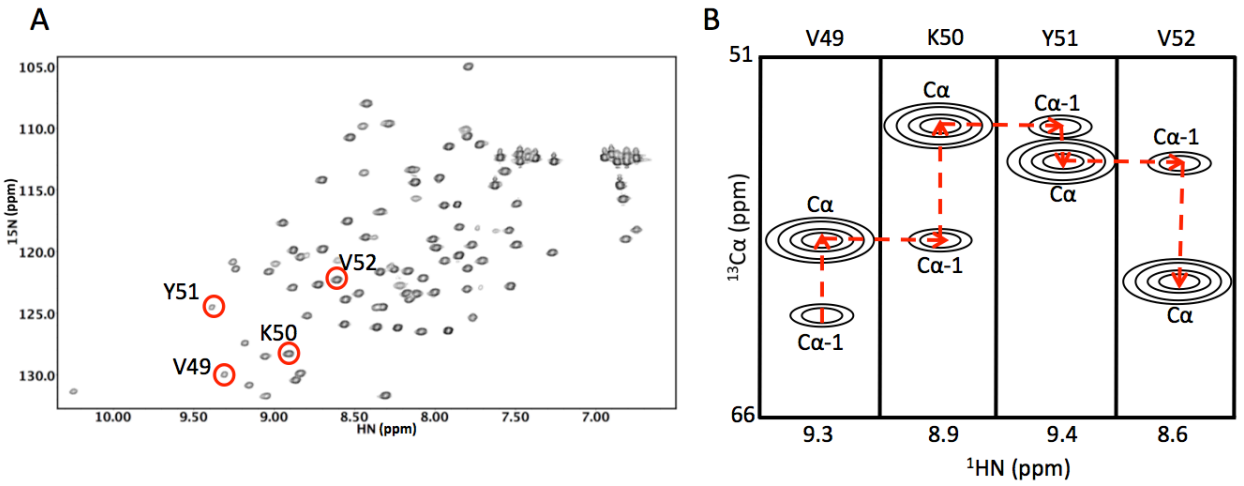

Figure 2.23: The sequential assignment of residues using the 3D HNCA experiment. (A) 2D ^{1}H, ^{15}N-HSQC plane of MBD1. (B) ^{1}H, ^{13}Cα-2D strips for the residues circled in the 2D HSQC in (A). The inter- and intra-residue Cα are shown as crosspeaks in the 2D strips. The inter-residue Cα has weaker peak intensity than the intra-residue Cα.

Three-dimensional side-chain experiments are used to assign the side-chain hydrogen and carbon chemical shifts of the corresponding amino acids (Figure 2.22B). Based on the number and values of distinct hydrogen and carbon chemical shifts for each amino acid residue, side-chain assignment experiments can also be used as a tool to verify the sequential backbone assignment. The standard side-chain assignment experiments are CC(CO)NH, H(CCO)NH, and ^{15}N-TOCSY-HSQC (Gardner and Kay, 1998). The CC(CO)NH experiment identifies the side-chain carbon chemical shifts of the previous residue (i-1), whereas the H(CCO)NH experiment identifies the side-chain hydrogen chemical shifts of the previous residue (i-1). The ^{15}N-TOCSY-HSQC experiment identifies the side-chain hydrogen chemical shifts of the current residue and is used in conjunction with the H(CCO)NH experiment.

2.5.4 Chemical shift perturbation mapping

Since chemical shifts are highly sensitive probes of the chemical environment, the ligand-binding site can be determined by mapping the chemical shift changes of the assigned residues in a series of 2D ^{15}N-HSQC or TROSY spectra. Chemical shift perturbation (CSP) analysis requires the addition of an unlabeled ligand to an isotopically labeled ^{15}N protein, or vice versa. The unlabeled ligand is titrated at increasing ratios until ligand binding to the ^{15}N protein is complete (Figure 2.24). The combined chemical shift changes are commonly calculated according to the following equation:

$$\Delta\delta_{combined} = [(\Delta\delta^2_H + \Delta\delta^2_N/25)/2]^{1/2}, \quad (2.11)$$

where $\Delta\delta_{NH}$ and $\Delta\delta_N$ are the chemical shift changes of the amide proton and nitrogen, respectively. A scaling factor for the ^{15}N chemical shift was applied to account for the differences in spectral widths between ^{1}H and ^{15}N resonances (Garrett et al., 1997; Grzesiek et al., 1996; Byerly et al., 2002). CSP can reveal important structural information about the binding surface and possible conformational changes within the protein.

NMR spectroscopy can detect ligand- or protein-protein interactions ranging from the millimolar to sub-nanomolar affinities. The ligand-binding affinity can be estimated by analyzing the chemical exchange regime the affected residues undergo. Chemical exchange is a dynamic process where an individual nucleus interconverts between two distinct chemical environments (Göbl et al., 2014). Residues can undergo three different types of exchange processes: fast, intermediate, and slow exchange. Fast exchange is associated with weak binding, usually in the millimolar range. In the fast exchange regime, only one peak is observed, and its coordinate is given by the weighted average of the chemical shifts of the free and ligand-bound state (Figure 2.24A). Intermediate exchange is usually correlated with micromolar affinities and is observed by the broadening of peaks and sometimes complete signal disappearance (Figure 2.24B). Slow exchange is correlated with tight binding and is manifested by two distinct peak signals corresponding to the free and bound states (Figure 2.24C).

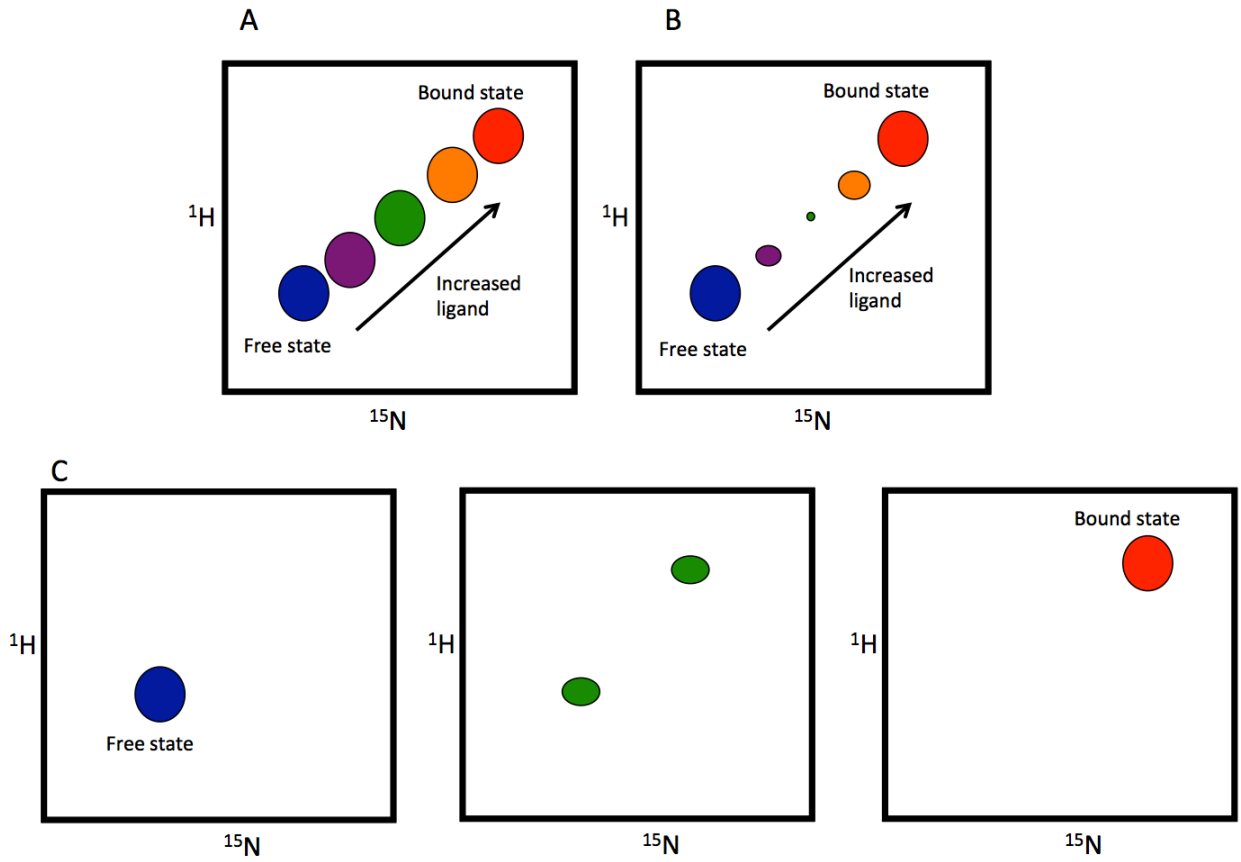

Figure 2.24: The chemical shift progression of one residue based on the different chemical exchange regimes. The ^{15}N-labeled protein goes from a free (*blue circle*) to a bound state (*red circle*). (A) In the fast exchange regime, peaks gradually shift to a new location as ligand is added. (B) In the intermediate exchange regime, peaks gradually shift to a new location and lose peak intensity as ligand is added. (C) In the slow exchange regime, the free and bound states are both observed until complete binding is reached.

2.5.5 NMR structure calculation

NMR structure determination involves using a set of experimentally derived restraints to calculate an ensemble of energy-minimized structures (Figure 2.25). The initial step for all NMR structure calculations is to identify the chemical shifts for as many chemically distinct ^{1}H, ^{15}N, and ^{13}C nuclei as possible. This is accomplished by assigning the amino acid residues through sequential backbone and side-chain experiments (Figure 2.22). Chemical shifts values are often correlated with protein secondary structure (Wishart et al., 1992), because each type of secondary structure has distinct ranges of ϕ and ψ dihedral backbone angles, as seen in the Ramachandran plot.

Dihedral angle restraints can be predicted on the basis of chemical shift values using the software program TALOS-N (Shen et al., 2013). TALOS-N compares the chemical shift values of HA, Cα, Cβ, CO, N, and NH for a given residue to the chemical shift values from a protein database.

Hydrogen bonds in protein secondary structure prevent efficient exchange of amide protons with the surrounding solvent. Therefore, hydrogen bonded amide protons can be identified by measuring hydrogen-deuterium (H/D) exchange rates (Figure 2.26). To measure H/D exchange rate, water in the sample is replaced with deuterium oxide (D_2O), followed by recording successive 2D ^{15}N-HSQC experiments. NMR peaks of amide protons that rapidly exchange with the D_2O solvent lose intensity at a faster rate because deuterium (^{2}H) is not observable in proton (^{1}H) NMR. By plotting the peak volumes as a function of time for each residue and extracting the exchange rate from the exponential decay curve, hydrogen bonded amide protons can be accurately identified.

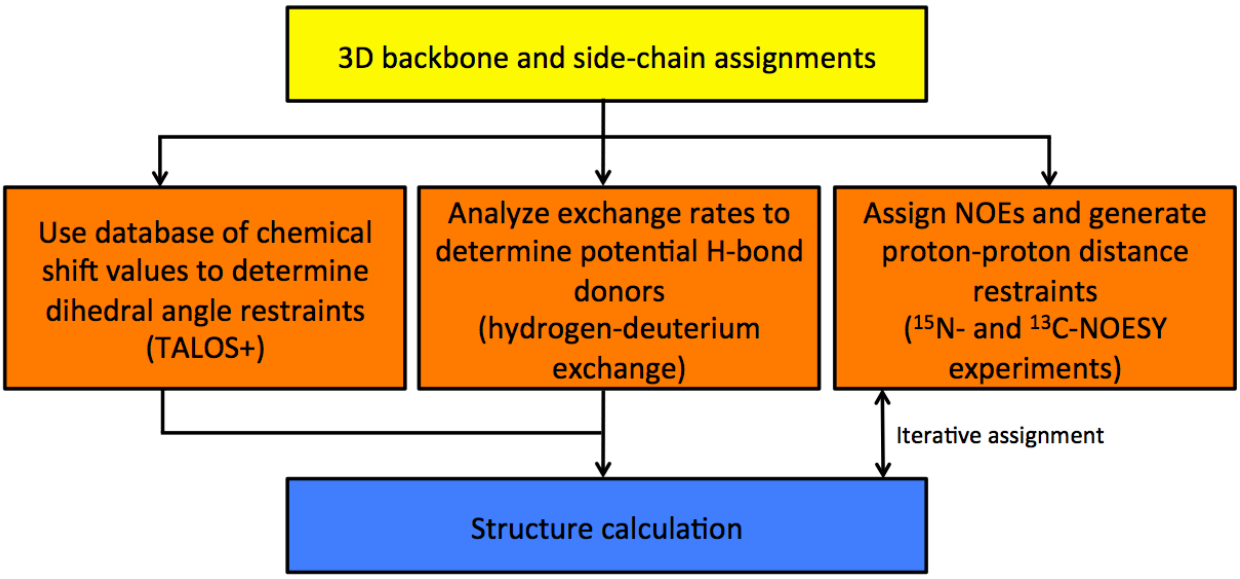

Figure 2.25: Protein structure determination by NMR spectroscopy. Chemical shift assignment for the backbone and side-chain amino acids provide restraints for structure calculation.

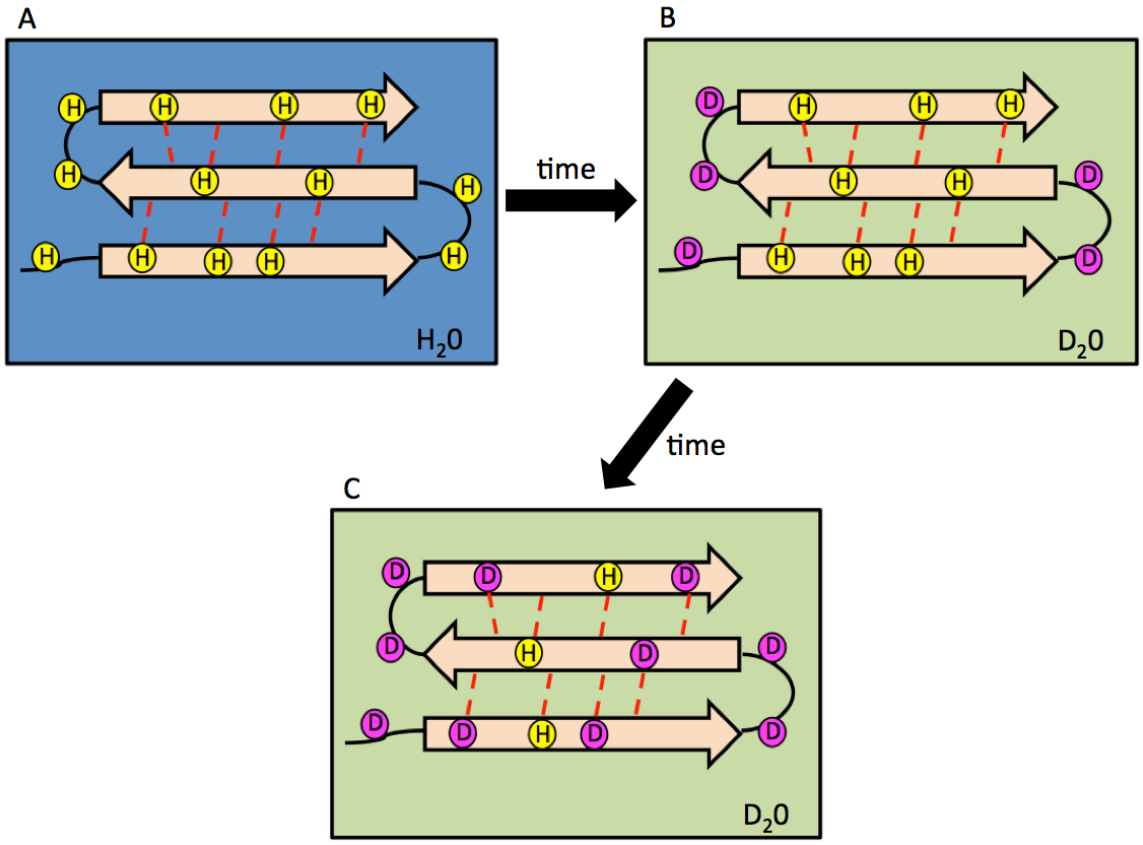

Figure 2.26: The process of hydrogen-deuterium exchange for analyzing residues involved in hydrogen bonding. (A) The anti-parallel β-sheet is dissolved in protonated (^1H) buffer and (B) diluted into buffer containing D_2O (^2H_2O). Labile protons rapidly exchange with the surrounding D_2O. (C) Amides involved in hydrogen bonding are protected from the deuterium solvent and will exchange more slowly with the surrounding solvent.

The most important type of restraints in NMR structure determination is distance restraints. The nuclear Overhauser effect (NOE) is a phenomenon that transfers magnetization from one nucleus to another through space (Overhauser, 1953). The NOE is first achieved by irradiating a population of nuclei until it reaches saturation. As the saturated population of atoms relaxes back to its equilibrium, magnetization is transferred to nearby atoms. For structure determination, in particular, the NOE is used to derive distance restraints between two hydrogen atoms in space (Wüthrich, 1989). The NOEs are a source of geometric information and can measure a range of distances for protons that are close together in three-dimensional space, even if they are far apart in the primary sequence. NOEs can be used to calculate distances because the NOE peak volume is proportional to $1/r^6$, where r is the distance between the two protons (Williamson, 2006). Since the observed NOEs decrease rapidly as the distance increases, the

practical detection limit between two protons is 5-6 Å. Although the NOE peak volumes translate into interproton distances, it is not a precise measurement, and commonly NOE-derived upper distance limits are used instead of precise distances. Strong NOEs reflect protons close together and weak NOEs reflect protons farther apart in space. Three-dimensional ^{15}N- and ^{13}C-NOESY experiments are used to measure NOE distance restraints (Gardner and Kay, 1998).

The preliminary NMR solution structure is subsequently refined against a set of structural restraints containing chemical shift assignments, dihedral angle restraints, and NOE distance restraints. The goal of NMR structure calculations is to find a global energy minimum for an ensemble of structures. Molecular dynamics in torsion angle space (TAD) with simulated annealing is the most widely used algorithm for calculating NMR structures and is implemented in popular programs such as CYANA and XPLOR-NIH (Güntert, 1998; Schwieters et al., 2006; Stein et al., 1997). This algorithm starts with an ensemble of random polypeptide chain conformations and a simulated annealing protocol is applied to each starting conformation. The simulated annealing procedure heats the system to a very high temperature and applies fixed values to covalent bond lengths and angles, while allowing rotation about the single bonds. As the temperature decreases in the SA protocol, inconsistent NOEs may trap the protein conformation in a local energy minimum. Kinetic energy is applied to the system to escape such energy wells in order to reach a global energy minimum. A target function describing the energy of the system is applied during structure calculations (Güntert, 1998). The target function contains experimental terms such as distance restraints measured from NOE experiments and theoretical terms such as van der Waals interactions. It determines whether the quality of the overall structure satisfies the experimentally determined distance and dihedral angle restraints. The target function increases when the structure deviates from the experimental data and violates physical parameters such as van der Waals interactions. Therefore, a minimized target function commonly generates protein structures at a global energy minimum.

To validate that the calculated NMR structures are correct, distance and dihedral angle restraint violations are analyzed. NOE violations are manually assessed in an iterative manner to determine whether the distance restraints should be adjusted (Spronk et al, 2004). The quality of the dihedral angle restraints in secondary structures is compared to the Ramachandran plot

(Spronk et al., 2004). A lower backbone root-mean-square deviation (RMSD) indicates improvement in the precision of the NMR structure. The Protein Structure Validation Software Suite (PSVS) (Bhattacharya et al., 2006) integrates several software programs such as PROCHECK (Laskowski et al., 1993) and MolProbity (Lovell et al., 2003) to assess the quality of an NMR structure.

2.6 Nanobodies as probes to analyze dynamics and conformation of MBD1-6 in ATP7B

2.6.1 Structural features of nanobodies

The N-terminal region of ATP7B is a large multi-domain protein that is highly dynamic. It consists of six MBDs that are connected by flexible protein linkers. Solving the structure of MBD1-6 at atomic resolution using traditional methods such as NMR and X-ray crystallography is challenging. Highly mobile proteins cannot be crystallized because of insufficient crystal contacts. Crystallization chaperones can force MBD1-6 into a stable conformation (Rasmussen et al., 2011), however, these may not be physiologically relevant. On the other hand, solving the structure of MBD1-6 by NMR using the traditional NOE method may not be very accurate. NOE assignment ambiguity and the lack of long-range inter-domain NOEs are two major problems for solving the NMR structure of MBD1-6. However, NMR is a powerful method that can provide important dynamic information in various timescales. Protein dynamics may help us gain insight into the conformation of MBD1-6 and identify possible transient interactions between the individual MBDs. In our studies, we have used nanobodies to probe the backbone dynamics of MBD1-6. A nanobody is a single-domain antibody fragment, which binds to the target protein with high affinity and specificity (Muyldermans, 2013). It is characteristic of conventional antibodies but is much smaller in size. Large proteins that bind to MBD1-6 lead to fast relaxation, producing broad NMR linewidths and diminished spectral quality. The binding of conventional antibodies (150 kDa) or Fab fragments (50 kDa) to isotopically labeled MBD1-6 would completely deteriorate the quality of the 2D ^{1}H-^{15}N HSQC spectrum, providing no useful structural or dynamic information. On the other hand, the small size of a nanobody is particularly advantageous in NMR studies because the binding of a nanobody can change the structure or dynamics of specific individual MBDs without adversely decreasing the overall quality of the NMR spectra (Huang et al., 2014; Dmitriev et al., 2016).

The conventional immunoglobulin G (IgG) antibody consists of two heavy and two light chains that are each 50 kDa and 25 kDa, respectively (Muyldermans, 2013) (Figure 2.27A). These chains are connected together by disulfide bonds and non-covalent interactions, forming a 150 kDa protein complex. The antigen binding properties are defined by the complementarity-determining regions (CDRs) of the variable heavy and light chains. The large size of the antibody has prompted the development of smaller antibody derivatives. The Fab fragment is

approximately 50 kDa and contains two variable domains and a truncated heavy chain (Figure 2.27A). A single-chain fragment (scFV) was later developed that contains two variable domains, which are connected by a peptide linker. Removal of the variable light chain in the scFv exposes a large hydrophobic surface that causes aggregation and poor solubility (Davies and Riechmann, 1994; Ward et al., 1989). The search for a small antibody derivative with optimal biochemical properties led to heavy-chain antibodies.

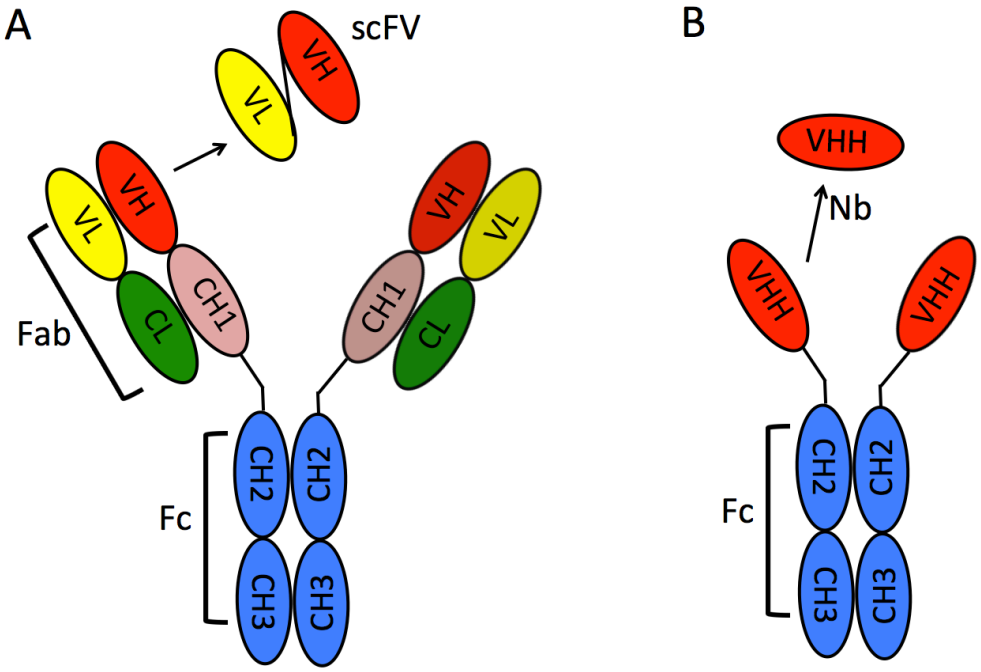

Figure 2.27: Structural organization of (A) conventional IgG antibodies and (B) heavy-chain antibodies. The smallest antibody derivative from conventional and heavy-chain antibodies is scFV and nanobody, respectively.

Heavy-chain antibodies (HCAbs) are found only in the *Camelidae* family (camels, llamas, and alpacas) and sharks. These HCAbs are structurally similar to IgG, except that they lack the light chains (Muyldermans, 2013) (Figure 2.27B). Since the isolated variable domain of HCAbs (VHH) does not contact any other domain in the antibody molecule, its surface is hydrophilic, and it does not aggregate in solution. The unique properties of the VHH have spawned a new type of antibody derivative called a nanobody.

A nanobody is an isolated, recombinant-produced variable domain of the heavy-chain antibody. The core structure of a nanobody is composed of β-sheets, with the CDRs forming the

antigen-binding site (Desmyter et al., 1996) (Figure 2.28). A significant difference between the structure of camel VHH and the VH domains from human and mouse is the length of CDR3 (Desmyter et al., 1996). The average length of the CDR3 is longer for camel VHH than the human and mouse CDR3. Therefore, the nanobody CDR3 protrudes much farther from the surface of the core structure, which allows nanobodies to recognize epitopes that are unattainable with conventional antibodies (Figure 2.28). Nanobodies are advantageous over conventional antibodies because of their small size (12-15 kDa), ease of recombinant expression, high solubility, and binding specificity.

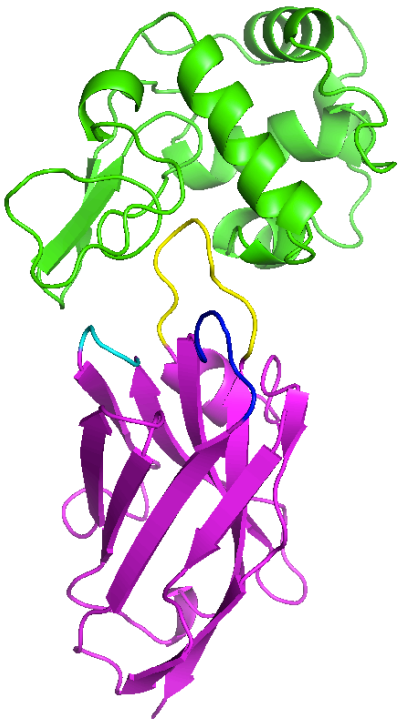

Figure 2.28: The crystal structure of a nanobody (magenta) bound to lysozyme (green). The CDR1-3 loops are shown in blue, cyan, and yellow, respectively.

2.6.2 Nanobody production and selection

A detailed protocol for producing and selecting nanobodies has been published (Pardon et al., 2014) (Figure 2.29), and is briefly described here using MBD1-6 as an example. Nanobodies for our work were generated in the laboratory of Dr. Serge Muyldermans at Free University of Brussels. We have selected nanobodies that specifically bind to MBD1-6. First, MBD1-6 was purified using affinity and ion-exchange chromatography (Figure 2.29A). MBD1-6 was used as

an antigen for immunization in alpaca (Figure 2.29B). As the immune response matured, mRNA was extracted from isolated peripheral blood lymphocytes and used to generate the cDNA library of the VHH by reverse transcription (Figure 2.29B). The VHH cDNA library was subsequently used for selecting nanobodies by phage display, using MBD1-6 as an immobilized antigen (Figure 2.29C). Multiple rounds of panning were performed to enrich for target-specific nanobodies. The selected nanobodies were expressed in *Escherichia coli* with a histidine tag for one-step purification by Ni-NTA affinity chromatography (Figure 2.29D).

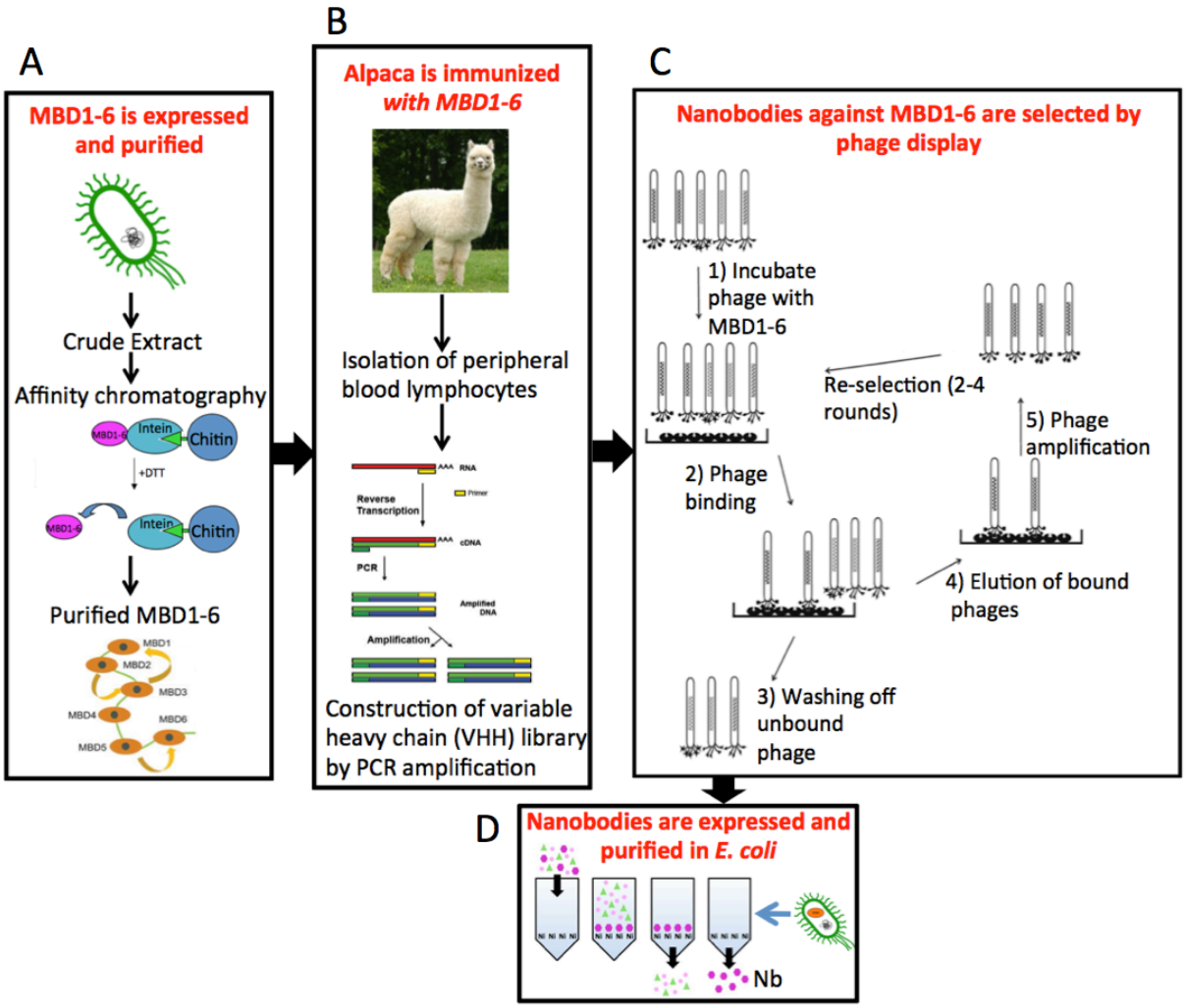

Figure 2.29: Production and selection of nanobodies. (A) MBD1-6 is expressed and purified by affinity and anion-exchange chromatography. (B) Alpaca is immunized with MBD1-6 and blood lymphocytes are obtained. The mRNA is isolated to generate the cDNA library of the VHH. (C) Phage display selects for nanobodies against MBD1-6. (D) Nanobodies are expressed in *E. coli* and purified by Ni-NTA chromatography.

3 Materials and Methods

3.1 Generation of protein constructs in the pTYB12 expression vector

Recombinant DNA corresponding to the open reading frame of metal-binding domain 1 of ATP7B was cloned into the pTYB12 expression vector (New England Biolabs). The pTYB12 vector is designed to fuse the N-terminus of the target protein to a self-cleavable intein tag that attaches to the chitin-binding domain (Chong et al., 1997) (Figure 3.1). The chitin-binding domain in the expressed fusion protein attaches to chitin beads, allowing a single-step purification process (Chong et al., 1997). The addition of DTT induces the self-cleaving activity of the intein, which releases the target protein from the CBD-intein tag (Chong et al., 1997).

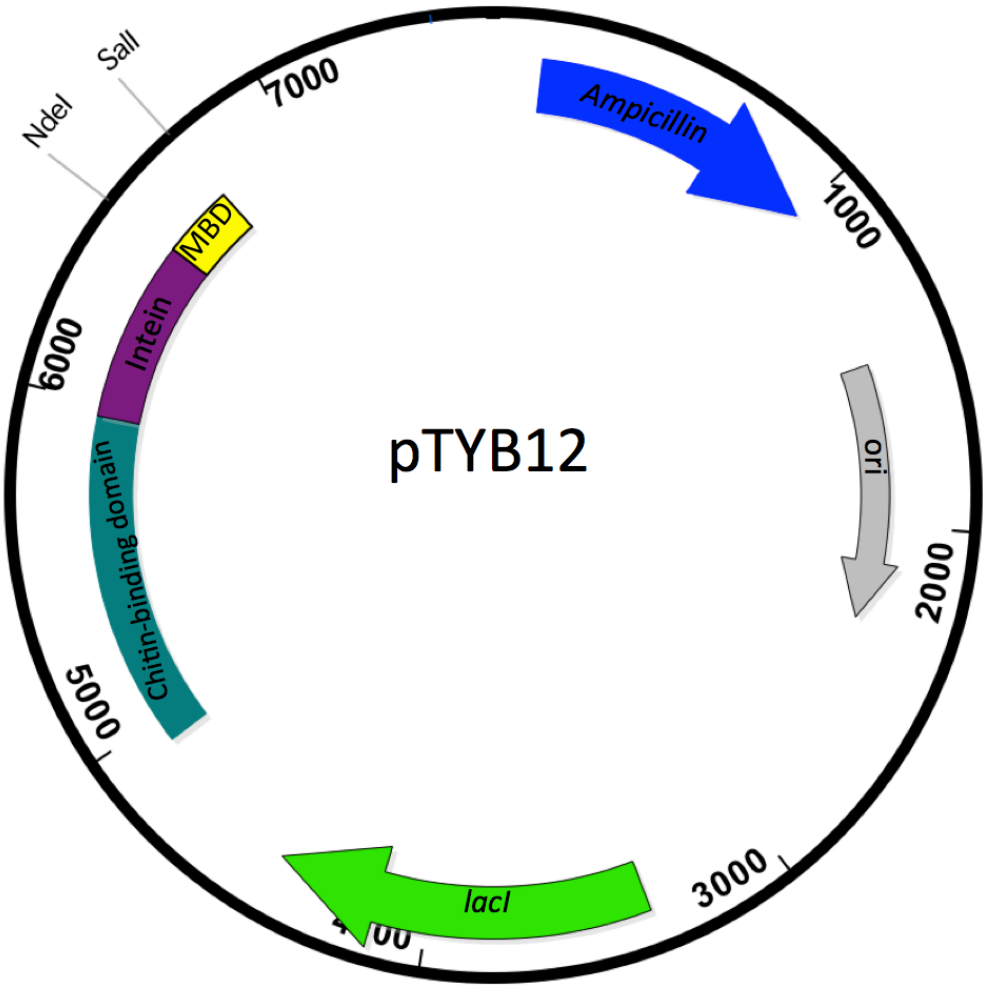

Figure 3.1: Map of pTYB12-MBD expression vector. The MBD target gene (*yellow*) is inserted in-between the *NdeI* and *SalI* restriction sites and fused with the intein tag (*purple*). The intein tag is attached to the chitin-binding domain (*turquoise*). The plasmid is ampicillin resistant (*blue*) and expression is controlled by the IPTG-inducible lac promoter (*green*).

Dr. Natasha Dolgova previously designed the vectors that were used for expressing some of the proteins used in this work, and as starting points for generating expression vectors for others. The pTYB12 fusion construct containing MBD1-6 (pND11) was used as a template for cloning pCY_MBD1, pCY_MBD4, pCY_MBD1-3, and pCY_MBD5-6 (Table 3.1). The mutant SxxS MBD1-4 (pND8) was used as a template for cloning pCY_MutMBD1. Mutant G875R-A-domain (pND23) was used in site-directed mutagenesis as a template for cloning the wild-type G875 A-domain. The original hTrx1 plasmid (pET-3a-hTrx1) was a gift from Dr. David Sanders (Department of Chemistry; University of Saskatchewan) and was used as a template to sub-clone hTrx1 into the pTYB12 expression vector (pCY_hTrx1).

Table 3.1: Summary of the plasmids used for expression and purification.

Plasmid Name	Target Expression Product	Description
pND11	MBD1-6	Encodes MBD1-6 of ATP7B
pND8	Mutant SxxS MBD1-4	Encodes MBD1-4 of ATP7B with serine substitutions (CxxC → SxxS)
pND23	G875R-A-domain	Encodes A-domain with R875 point mutation
pET-3a-hTrx1	hTrx1	Encodes human thioredoxin
Derivative plasmids from pND and pET vectors		
pCY_MBD1	MBD1	Encodes MBD1 of ATP7B
pCY_MutMBD1	MBD1	Encodes mutant SxxS-MBD1 of ATP7B
pCY_MBD4	MBD4	Encodes MBD4 of ATP7B
pCY_hTrx1	hTrx1	Encodes human thioredoxin
pCY_MBD1-3	MBD1-3	Encodes MBD1-3 of ATP7B
pCY_MBD5-6	MBD5-6	Encodes MBD5-6 of ATP7B
pCY-Gly875_Adom	A-domain	Encodes Gly875 variant of A-domain

Single colonies were selected, used to inoculate 5 mL LB media containing 100 μg/mL ampicillin, and grown overnight at 37 °C with shaking at 220 r.p.m. All the plasmids were isolated from DH5α *E. coli* cultures using a QIAprep Spin Miniprep Kit (Qiagen) and eluted with 30 μL sterile water. Plasmids were stored at -20 °C.

All restriction exonucleases were supplied by New England Biolabs. DNA restriction reactions were set up in 20 μL volumes with 0.5 – 2.0 μg of plasmid DNA, 5 U of each

restriction enzyme, and 2 μL of the appropriate 10 x NEB reaction buffer. All PCR fragments incorporated 5'-*NdeI* and 3'-*SalI* restriction sites into the recombinant PCR product with the following primers (Table 3.2). Both the pTYB12 vector and the desired PCR fragment were digested with *NdeI* and *SalI* restriction enzymes with incubation at 37 °C for 30 minutes. The digested vector and PCR fragment were gel purified using the QIAquick gel extraction kit (Qiagen).

Ligation reactions were set up in 20 μL volumes. Each reaction contained 50 ng vector DNA, 80 ng inset DNA, 2 μL of 10 x T4 DNA ligase buffer, and 400 U of T4 DNA ligase (NEB). Ligation mixtures were incubated overnight at 16 °C. The resulting constructs were verified by automated DNA sequencing and transformed into *E. coli* BL21(DE3) cells for protein expression.

Competent *E. coli* BL21(DE3) competent cells were prepared using $CaCl_2$ transformation. Fifty microliters of competent cells were incubated with 0.3 μg plasmid DNA for 30 minutes on ice. The cells were then heat shocked for 45 seconds at 42 °C and incubated on ice for ten minutes. The cells were then transferred into 200 μL of LB media and incubated at 37 °C for one hour with shaking at 550 r.p.m. The cells were then plated on LB agar containing 100 μg/μL ampicillin and incubated overnight at 37 °C.

Table 3.2: List of primers used in cloning.

Primer Name	Sequence	Description
CY-MBD1F	5'- GAGCATATGCAGGTGGCCACCAGCACAGTC - 3'	Forward primer for metal-binding domain 1
CY-MBD1R	5' - CCAGTCGACTTATTCTGCAATGCTGGCCTCGA - 3'	Reverse primer for metal-binding domain 1
CY-MBD4F	5' - GAGCATATGACATGCAGTACCACTCTGATTGCC - 3'	Forward primer for metal-binding domain 4
CY-MBD4R	5' - GTGGTCGACTTAAGAAACGACTGAAGCCTCAAATCCC - 3'	Reverse primer for metal-binding domain 4
CY-hTrxF	5' - GAGCATATGGTGAAGCAG ATCGAGAGCAAGACTGC - 3'	Forward primer for human thioredoxin
CY-hTrxR	5' - CGCGTCGACTTAGACTAATTC ATTAATGGTGGC - 3'	Reverse primer for human thioredoxin
pAM-R1n	5' - CCAGTCGACTTATTCTGCAATGCTGGCCTCGA - 3'	Reverse primer for metal-binding domain 3
ND-4028F	5' - (P)CACTGTAATTGCGGGGTCTATAAA TGC - 3'	Forward primer for A-domain (Gly875)
ND-4027R	5' - (P)CTTCCGGGTTTCTTAGTGACTGG - 3'	Reverse primer for A-domain (Gly875)
CY-MBD56F	5' - GAG CAT ATG GCA CCG CAG AAG TGC TTC TTA - 3'	Forward primer for metal-binding domain 5-6
CY-MBD56R	5'- CCA GTC GAC TTA CTG GGC CAG GGA AGC ATG - 3'	Reverse primer for metal-binding domain 5-6

3.2 Purification of Atox1 and metal-binding domains of ATP7B

The *E. coli* BL21(DE3) strain with a desired pTYB12 expression vector was grown in a shaking incubator and the expressed protein was purified using the following procedure. Six litres of *E. coli* BL21(DE3)/pTYB12 cell culture were grown at 37 °C in Luria broth to OD_{600} of 0.6-0.8 and pelleted by centrifugation at 6,000 x g. The bacteria was re-suspended in M63 minimal medium supplemented with 0.5 mg/L $FeSO_4$, 0.3% glucose, and 100 mg/L ampicillin (Elbing and Brent, 1998). For experiments that require isotopically enriched ^{15}N and ^{13}C protein, M63 minimal media was supplemented with $^{15}NH_4Cl$ and ^{13}C-D-glucose as the sole nitrogen and carbon sources, respectively (Cambridge Isotopes). Expression of the proteins was induced by the addition of 500 μM isopropyl β-d -1-thiogalactopyranoside (IPTG) followed by incubation at 16 °C for 16-20 hours. Cells were harvested by centrifugation at 6,000 x g for 15 minutes at 4 °C.

Cells were homogenized and disrupted using a cell disruptor (Constant Systems Limited) at 35 kpsi. The cell extract was centrifuged at 27,000 x g for 45 minutes, the supernatant was collected and subjected to chitin-affinity chromatography. The column was loaded with 30 mL of chitin beads and equilibrated with three bed volumes of wash buffer (50 mM Tris-HCl pH 8.2, 500 mM NaCl). The supernatant was applied to the column at a rate of 0.5-1 mL/min. Then the column was washed with 30 bed volumes of wash buffer at an unrestricted gravity flow rate, followed by 3 bed volumes of cleavage buffer (50 mM Tris-HCl pH 8.2, 150 mM NaCl, 50 mM DTT). The column was then incubated for 2-3 days at 4 °C. The proteins were eluted with 3 bed volumes of cleavage buffer in 10 mL fractions and dialyzed overnight against 50 mM Tris-HCl pH 8.2 and 50 mM NaCl to remove excess DTT from the eluted protein.

Additional purification of MBD1-6 after chitin-affinity chromatography was performed by anion-exchange chromatography. The protein sample was loaded on a 5 mL HiTrap Q column (GE Healthcare), equilibrated with 10 column volumes of Buffer A (50 mM Tris-HCl pH 8.2, 50 mM NaCl, and 5 mM DTT). The column was washed with 10 column volumes of Buffer A and eluted using a linear concentration gradient of 50-500 mM NaCl in Buffer A.

Protein purity was determined using sodium dodecycl sulfate polyacrylamide gel electrophoresis (SDS-PAGE).

3.3 Nanobody expression and purification by Ni^{2+}-affinity chromatography

E. coli WK6 cells with the pHEN6c expression vector were grown at 37 °C in TB media to OD_{600} of 0.6-0.9 (Pardon et al., 2014). The growth media was supplemented with 1 mM $MgCl_2$, 0.1% (w/v) glucose, and 100 μg/mL ampicillin (Pardon et al., 2014). Nanobody expression was induced with 1 mM IPTG followed by incubation at 28 °C for 16-20 hours. The nanobodies are expressed with a secretion signal that targets the nanobodies to the periplasm for easy purification and disulfide bond formation.

Cells were centrifuged at 9,000 x g for 15 minutes at room temperature, re-suspended in 15 mL of TES (0.2 M Tris pH 8.0, 0.5 mM EDTA, and 0.5 M sucrose), shaken for 1 hour on ice, diluted with 30 mL of TES/4, and incubated for an additional 1 hour on ice. The periplasmic proteins were collected by centrifugation at 10,000 x g for 30 minutes at 4 °C and purified using Ni-NTA resin (Pardon et al., 2014).

3.4 NMR experiments and data analysis

3.4.1 NMR sample preparation

For all NMR experiments, samples contained 50 mM HEPES pH 7.4, 50 mM NaCl, 5 mM TCEP, 1 mM DSS, and 10% (v/v) D_2O, unless otherwise specified. All HSQC experiments, except for structure determination, were recorded at 298 K on a 600 MHz Bruker NMR spectrometer at Saskatchewan Structural Sciences Centre (SSSC), University of Saskatchewan, with a T_1 relaxation delay of 1.1 seconds. The spectrometer was equipped with either a triple-resonance Cryoprobe with z-axis pulse field gradients or a TXI microprobe. TROSY (Pervushin et al., 1997) and transverse relaxation experiments (Zhu et al., 2000) for MBD1-6 were acquired at 310 K on a 900 MHz Varian NMR spectrometer at the National Magnetic Resonance Facility at Madison (NMRFAM), University of Wisconsin. This spectrometer was equipped with a triple-resonance cold probe with z-axis gradients, unless otherwise specified.

All data were processed using NMRPipe (Delaglio et al., 1995). The HSQC, TROSY, and NMR transverse relaxation experiments were analyzed using NMRView (Johnson, 2004).

3.4.2 Monitoring protein-protein interactions and metal-binding and -transfer by chemical shift perturbation analysis

Metal-binding to Atox1 or MBD2.

Purified protein was incubated with 10 mM EDTA for 30 minutes on ice. MBD2 was then dialyzed twice against 50 mM HEPES pH 7.4, 50 mM NaCl, and 0.6 mM TCEP for a total of eight hours and twice again against degassed 50 mM HEPES pH 7.4, 50 mM NaCl. The protein was dialyzed for a total of 16 hours. A cisplatin stock concentration of 4.5 mM was freshly prepared in degassed NMR buffer and was added to either Atox1 or MBD2 at a molar ratio of 1:1.

Atox1-MBD2 and MBD2-GSH, -hTrx1, and hGrx1 cisplatin transfer experiments.

Unlabeled Atox1 was pre-treated with cisplatin, as described above, at a 1:1 molar ratio. Unlabeled Atox1-Pt was concentrated to 0.5 mM, added to ^{15}N-labeled MBD2 at a molar ratio of 1:1, and then a series of 2D ^{15}N-HSQC spectra were recorded. For the reverse transfer experiment, unlabeled *apo*-Atox1 was added at a 2:1 molar ratio to ^{15}N MBD2-Pt.

The return of MBD2-Pt back to the apo form was examined in the presence of GSH, hTrx1, or hGrx1. MBD2 was reacted with cisplatin, added to unlabeled hTrx1 or hGrx1 at a 1:1 molar ratio, and a series of 2D ^{15}N-HSQC spectra were recorded. For the MBD2-GSH cisplatin transfer experiments, residual TCEP was removed from MBD2-Pt by gel filtration on a Superdex-200 column in a buffer containing 50 mM HEPES pH 7.4 and 50 mM NaCl. GSH was then added to the protein to a final concentration of 5 mM.

Concentration of the MBD2-Pt complex was calculated according to the following equation:

$$[\text{MBD2-Pt}] = [\text{MBD2}_{\text{total}}]*V_{Pt}/(V_{apo} + V_{Pt}), \quad (3.1)$$

where $[\text{MBD2}_{\text{total}}]$ is the total MBD2 concentration in the NMR sample, and V_{Pt} and V_{apo} are peak volumes of the backbone amide signal in the platinum-bound and apo form, respectively, in the ^{1}H, ^{15}N-HSQC spectrum recorded at a given time after the addition of cisplatin, carboplatin, GSH, hGrx1, or hTrx1. G27 was the reporter group for measuring the peak volume of MBD2-Pt in the presence of cisplatin, carboplatin, and GSH, whereas G15 was used for measuring the peak volume of MBD2-Pt in the presence of hGrx1 and hTrx1.

Interaction between MBD1, MBD2, and MBD3 and molecular modeling.

Domain-domain interactions using chemical shift perturbation analysis were performed using three pairs of isolated MBDs: MBD1-MBD2, MBD1-MBD3, and MBD2-MBD3. To determine contact surfaces between the individual MBDs, both the unlabeled and ^{15}N-labeled forms of MBD1, MBD2, and MBD3 were purified. For each ^{15}N-labeled protein, the unlabeled partner protein was added at a 1:1 molar ratio to a final protein concentration of 150 μM. A 2D ^{15}N-HSQC spectrum was recorded before and after the addition of the unlabeled protein to measure chemical shift changes. The chemical shift changes of the isotopically labeled protein were submitted as docking restraints in the program, HADDOCK (de Vries et al., 2010). 1000 initial structures were generated by rigid-body docking using ambiguous distance restraints and the 200 lowest energy structures were subsequently refined with simulated annealing (de Vries et al., 2010). A final cycle with explicit water refinement was used and ten clusters were generated based on the backbone RMSD of all the atoms in the complex. These final clusters were ranked according to the sum of interaction energies as reported by the HADDOCK program (de Vries et al., 2010) and the cluster with the most negative HADDOCK score was selected to represent the MBD1-MBD3 interaction surface.

3.4.3 Chemical shift assignment and structure determination of MBD1

Backbone chemical shift assignments for MBD1 were made from HNCO, HNCA, HNCACB, HN(CA)CO, and HN(CO)CACB (Gardner and Kay, 1998). Side-chain assignment experiments were done using H(CCO)NH, CC(O)NH, AND ^{1}H, ^{15}N-TOCSY (Gardner and Kay, 1998). The parameters for the backbone- and side-chain experiments for the structure calculation of MBD1 are listed in Table 3.3. All of the chemical shift assignment experiments were performed at 298 K on a Bruker NMR spectrometer operating at 750 MHz ^{1}H Larmor frequency (NMRFAM) and the backbone chemical shifts were assigned using CARA (Keller, 2005). The assignments have been deposited at BioMagResBank (accession no. 25827). Peak tables and distance restraints were generated using the program, PONDEROSA (Lee et al., 2011), from 3D ^{1}H, ^{15}N-NOESY and 3D ^{1}H, ^{13}C-NOESY experiments. NMRFAM-SPARKY (Lee et al., 2015) was used in conjunction with PYMOL (DeLano, 2005) in PONDEROSA-C/S to manually validate NOE distance restraints and assignments (Lee et al., 2014). The structure was calculated using the PONDEROSA-X option in PONDEROSA-C/S, which is an XPLOR-NIH based structure calculation software package (Schwieters, et al., 2006). The structural ensemble of MBD1 consists of the 20 best structures chosen from a total of 100 structures, based on the lowest energy and fewest violations. The atomic coordinates have been deposited at the Protein Data Bank (ID code 2N7Y).

Hydrogen bond distance restraints for MBD1 were derived from H/D exchange measurements. MBD1 was transferred from the standard NMR buffer to the same buffer (50 mM HEPES pH 7.4, 50 mM NaCl, and 5 mM TCEP) prepared in 100% D_2O using a NAP-5 desalting columns (GE Healthcare). A series of ^{1}H-^{15}N HSQC experiments were recorded immediately after buffer exchange over a period of 12 hours and the peak volume change was measured as a function of time.

Table 3.3: Acquisition parameters for the NMR structure determination experiments for MBD1.

Experiments	Dimension of acquired data			Spectral width (ppm)			Number of scans
	t_1	t_2	t_3	F_1	F_2	F_3	
HNCO	64 (^{13}C)	96 (^{15}N)	2048 (^{1}H)	15	40	16	8
HNCA	112 (^{13}C)	96 (^{15}N)	2048 (^{1}H)	15	40	16	8
HNCACB	160 (^{13}C)	96 (^{15}N)	2048 (^{1}H)	40	40	16	8
HN(CA)CO	64 (^{13}C)	96 (^{15}N)	2048 (^{1}H)	15	40	16	16
HN(CO)CACB	160 (^{13}C)	96 (^{15}N)	2048 (^{1}H)	55	40	16	8
H(CCO)NH	128 (^{13}C)	48 (^{15}N)	2048 (^{1}H)	16	40	16	16
CC(O)NH	128 (^{13}C)	64 (^{15}N)	2048 (^{1}H)	75	40	16	16
^{1}H-^{15}N TOCSY HSQC	164 (^{13}C)	40 (^{15}N)	2048 (^{1}H)	12	40	16	16
^{15}N-NOESY	256 (^{13}C)	96 (^{15}N)	2048 (^{1}H)	11	40	16	8
^{13}C-NOESY	256 (^{13}C)	80 (^{15}N)	2048 (^{1}H)	14	75	16	8

3.4.4 Transverse relaxation studies of nanobody-binding and Atox1-Cu transfer to MBD1-6

To prepare samples for NMR relaxation analysis, nanobodies were added in equimolar ratios to MBD1-6. Unlabeled Atox1 was pretreated with Cu(I) at a 1:1 molar ratio and subsequently added to MBD1-6 at a 6:1 molar ratio. Longitudinal (R_1) relaxation, transverse relaxation (R_2), and heteronuclear ^{15}N{^{1}H}-NOEs were only measured for nanobody-free and R50-bound MBD1-6. To determine the R_1 relaxation rates of the individual domains, several spectra were collected with different relaxation delays ranging from 0 to 1200 ms. For the R_2 relaxation rates of the individual domains in each experiment, several ^{1}H-^{15}N HSQC spectra were collected with different relaxation delays ranging from 0 to 140 ms (Zhu et al., 2000) (Table 3.4). The relaxation rates were extracted using NMRView (Johnson, 2004) by exponentially fitting the peak intensities to a series of ^{1}H, ^{15}N-TROSY spectra. The

heteronuclear $^{15}N\{^{1}H\}$-NOE values were determined from the ratio of peak intensities measured with and without proton saturation.

Dr. Sergiy Nokhrin calculated the correlation times (τ_c) of the individual metal-binding domains in apo- and R50-bound MBD1-6 from the relaxation rates and ^{1}H-^{15}N heteronuclear NOE data using the TENSOR V2 program (Dosset et al., 2000).

Table 3.4: Acquisition parameters for the MBD1-6 transverse relaxation experiments.

R_2 relaxation of ^{15}N MBD1-6	**Type of relaxation experiment**	**Dimension of acquired data**		**Spectral width (ppm)**		**Number of Experiments**	**Relaxation delays (ms)**
		t_1	**t_2**	**F_1**	**F_2**		
Apo MBD1-6	R_1	256 (^{15}N)	2048 (^{1}H)	33	16	7	0, 100, 180, 340, 500, 800, 1200
	R_2	256 (^{15}N)	2048 (^{1}H)	33	16	7	10, 20, 40, 60, 80, 110, 140
R50	R_1	256 (^{15}N)	2048 (^{1}H)	33	16	7	0, 100, 180, 340, 500, 800, 1200
	R_2	256 (^{15}N)	2048 (^{1}H)	33	16	7	10, 20, 40, 60, 80, 110, 140
1R1	R_2	256 (^{15}N)	2048 (^{1}H)	33	16	7	10, 20, 30, 40, 50, 70, 100
Apo Atox1	R_2	256 (^{15}N)	2048 (^{1}H)	33	16	8	10, 20, 30, 40, 60, 80, 100, 120
Atox1-Cu	R_2	256 (^{15}N)	2048 (^{1}H)	33	16	8	10, 20, 30, 40, 60, 80, 100, 120

3.5 Domain orientation studies of MBD1-3 using Small Angle X-ray Scattering

MBD1-3 was expressed and purified, as described above. Size-exclusion chromatography on a Superdex 75 column was performed to remove protein aggregates. MBD1-3 was dialyzed in SAXS buffer (50 mM HEPES pH 7.4, 50 mM NaCl, and 5 mM TCEP) for 36-48 hours. MBD1-3 data was collected on a Bruker NANOSTAR spectrometer with a Bruker

Turbo rotating Cu-anode x-ray source (NMRFAM). The dialysis buffer scattering signal was subtracted from the MBD1-3 scattering signal. The optimal scattering signal was recorded with 2.0 mg/mL of MBD1-3. Scattering data was analyzed using PRIMUS (Konarev et al., 2003) and other programs from the ATSAS software package (Petoukhov et al., 2012). DAMMIF (Franke and Svergun, 2009) was used to generate 10 independent *ab initio* dummy atom models from the experimental SAXS data.

3.6 Other analytical methods

3.6.1 SDS-PAGE

SDS-PAGE was performed as described by Schägger and von Jagow (Schägger et al., 1988). The stacking gel layer contained 3% acrylamide and the separating gel contained 10% acrylamide.

3.6.2 Protein determination by the BCA method

Protein concentration determination was carried out as previously described (Smith et al., 1985). BSA standard curves ranging from 0 μg – 50 μg per sample were conducted with each assay.

4 Results

4.1 Preliminary NMR studies and the strategy for the structural analysis of MBD1-6.

Currently, there is no high-resolution structure of the entire N-terminal region, encompassing all of the copper-binding domains. The structures of several individual MBDs, including MBDs 2 through 6, have been solved using NMR (Achila et al., 2006; Banci et al., 2008; Dolgova et al., 2013) and the copper binding affinities for each domain have been determined (K_a = 2.2 x 10^{-10} to 6.0 x 10^{-10} M^{-1}) (Yatsunyk and Rosenzweig, 2007). Each domain consists of a ferredoxin-like fold (βαββαβ), where the characteristic copper-binding CxxC motif is in a loop region between β1-strand and α1-helix. Copper binding to each domain does not induce significant conformational changes of the individual domain, only affecting the region in and adjacent to the copper-binding motif (Achila et al., 2006; Banci et al., 2008). However, this effect can be relayed along the protein backbone and cause significant structural rearrangements to other parts of MBD1-6 (DiDonato et al., 2000). Therefore, the overall spatial organization of MBD1-6 and the interactions between specific MBDs are critical for understanding ATP7B transport and regulation.

The ^{1}H, ^{15}N HSQC spectrum of MBD1-6 is well resolved for a protein with a molecular weight of 66 kDa (Banci et al., 2009a; Fatemi et al., 2010). The observed narrow linewidths suggest that the individual MBDs are highly dynamic. This observation is consistent with the high mobility of the MBD in the bacterial Cu^{+}-ATPase structure (Gourdon et al., 2011). By extension, this suggests that the six MBDs in ATP7B, which are connected by flexible linkers, are also highly dynamic and not amenable to X-ray crystallography.

Our goal was to investigate the conformation of full-length MBD1-6 and identify transient interactions between groups of MBDs using multi-dimensional and transverse relaxation NMR. Recombinant MBD1-6 was successfully expressed in the pTYB12 vector. We have optimized the purification of ^{15}N MBD1-6 using chitin-affinity chromatography followed by anion-exchange chromatography (Figure 4.1B). This purification process produced a yield of 0.4 mg/L cell culture with a protein purity of 95%. MBD1-6 produced a well-resolved ^{1}H, ^{15}N TROSY spectrum and the sample was stable for several days at a protein concentration of 160 μM at pH 7.4.

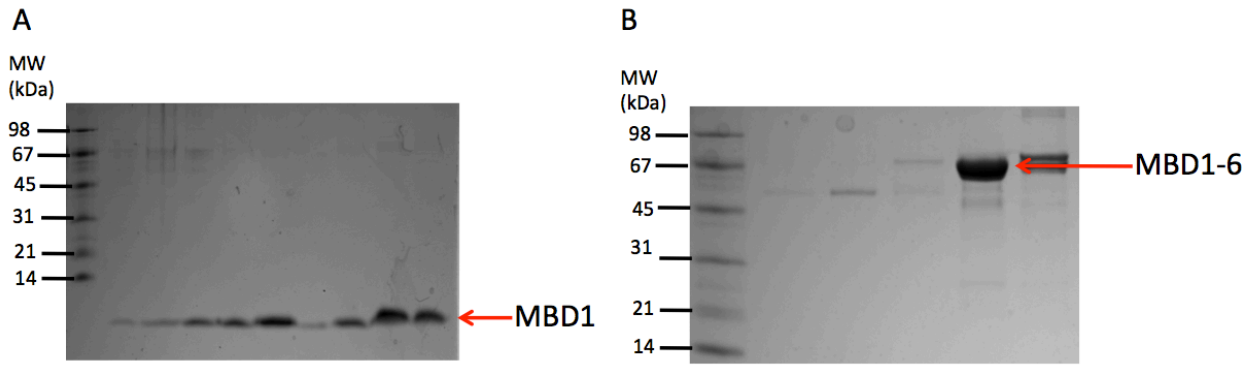

Figure 4.1: Purification of the metal-binding domains. Eluted fractions of purified (A) MBD1 purified by chitin-affinity chromatography and (B) MBD1-6 after chitin-affinity and anion-exchange chromatography. Protein fractions were analyzed by 10% SDS-PAGE and stained with Coomassie R250. The molecular weight of MBD2 is 8 kDa and MBD1-6 is 66 kDa.

The narrow linewidths in the spectrum imply that the individual MBDs in the full-length N-terminal region are highly dynamic. This suggests that MBD1-6 represents a "beads-on-a-string" model, with each MBD rotating independently from the others. Having obtained a high quality ^{1}H, ^{15}N-TROSY spectrum of MBD1-6 at 900 MHz, we assigned approximately 68% of the peaks using a previously established chemical shift assignment of ATP7B MBD1-6 (Banci et al., 2009a) (Figure 4.2). However, the first step in investigating the dynamics of MBD1-6 was to solve the structure of MBD1, the only domain whose structure was still missing.

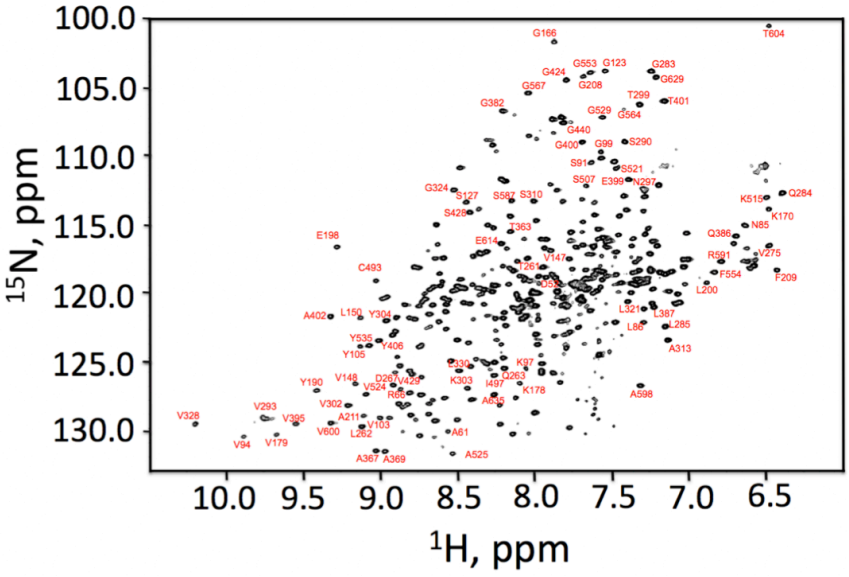

Figure 4.2: ^{1}H, ^{15}N-TROSY spectrum of MBD1-6 recorded at 900 MHz with some sequential assignments shown.

4.2 NMR structure of the metal-binding 1 of ATP7B

We solved a high-resolution structure of MBD1 using multi-dimensional NMR. MBD1 was purified by chitin-intein affinity chromatography to a 95% purity, producing a yield of ~1 mg/L of cell culture (Figure 4.1A). This purification protocol produced a folded protein based on the well-dispersed amide signals in the ^{1}H, ^{15}N-HSQC spectrum (Figure 4.3). Using standard triple resonance backbone and side-chain experiments with ^{13}C, ^{15}N-labeled MBD1, we assigned 72 out of 76 non-proline backbone residues (Figure 4.3). The unassigned backbone residues were A1, Q5, T17, and L58 (Figure 4.4B). Based on the structure of MBD2 of ATP7B (Dolgova et al., 2013), these residues were predicted to be located in flexible regions of the protein. The lack of backbone amide signal for these residues may be caused by increased chemical exchange with the surrounding solvent.

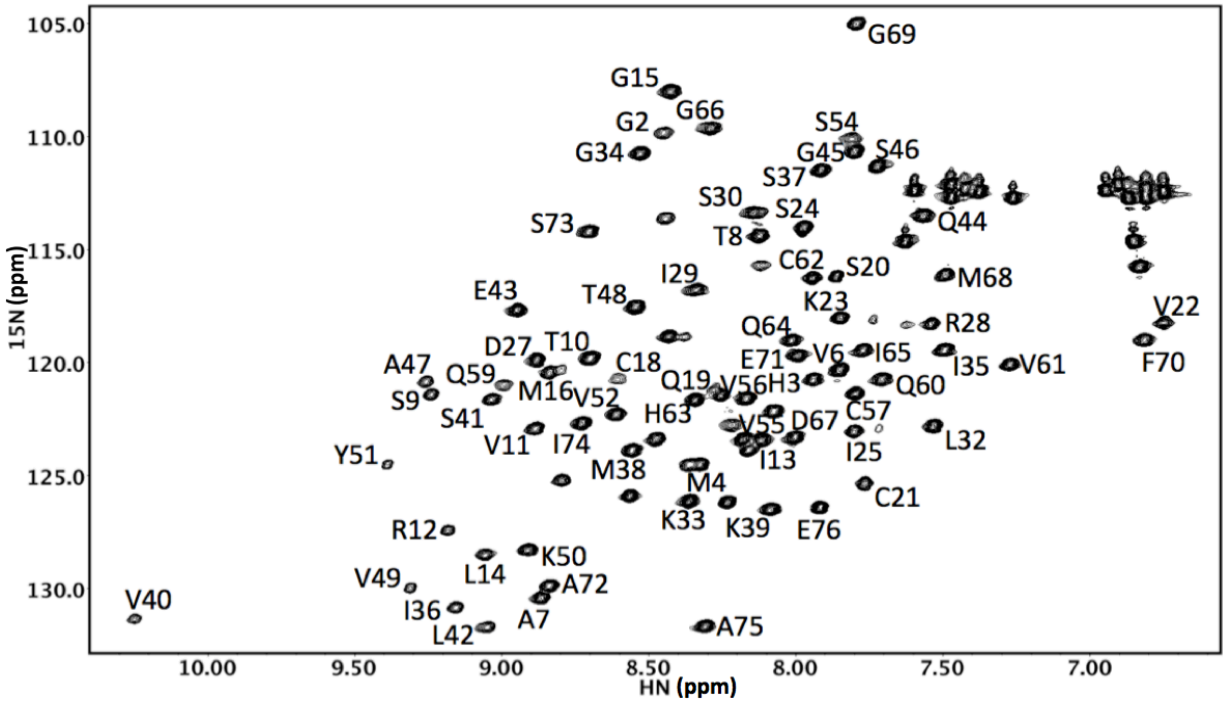

Figure 4.3: ^{1}H, ^{15}N-HSQC spectrum of ATP7B MBD1 with the backbone amide assignments shown.

The secondary structural elements of MBD1 were predicted by Talos-N (Shen and Bax, 2013) (Figure 4.4C). Since chemical shifts are strongly correlated with local secondary structure, Talos-N uses the ^{1}Hα, ^{15}N, ^{13}Cα, ^{13}Cβ, and ^{13}C' chemical shifts from a protein database to predict the values for the backbone ϕ and ψ dihedral angles (Shen and Bax, 2013). MBD1 forms the characteristic ferredoxin fold (βαββαβ), which is consistent with the other

MBDs of ATP7B (Achila et al., 2006; Banci et al., 2008; Dolgova et al., 2013; Fatemi et al., 2010) and ATP7A (Banci et al., 2004; DeSilva et al., 2005).

When at least 85% of the backbone and side-chain residues were assigned, the solution structure was calculated by incorporating assigned NOESY peak volumes of atoms from 3D ^{15}N- and ^{13}C-NOESY experiments. After several iterations of preliminary structure calculations, 48 hydrogen bond restraints were included in the structure calculation from hydrogen-deuterium (H/D) exchange experiments to help stabilize the secondary structures. The final solution structure of MBD1 was determined using 628 distance restraints obtained from automated NOE peak picking from 3D ^{15}N- and ^{13}C-NOESY experiments (Lee et al., 2011) and 119 dihedral angle restraints from Talos-N (Shen and Bax, 2013) (Figure 4.4A). The MBD1 structure was calculated using Xplor-NIH from the NMR structure determination package, PONDEROSA C/S (Lee et al., 2014). Xplor-NIH calculates protein structures by simulated annealing using torsion angle/rigid body dynamics. After energy minimization with explicit water refinement, the average backbone RMSD between the 20 calculated structures was 0.15 Å. Table 4.1 reports on the structural statistics and restraint violations of the final structural ensemble of MBD1 validated by the Protein Structure Validation Software Suite (Bhattacharya et al., 2006).

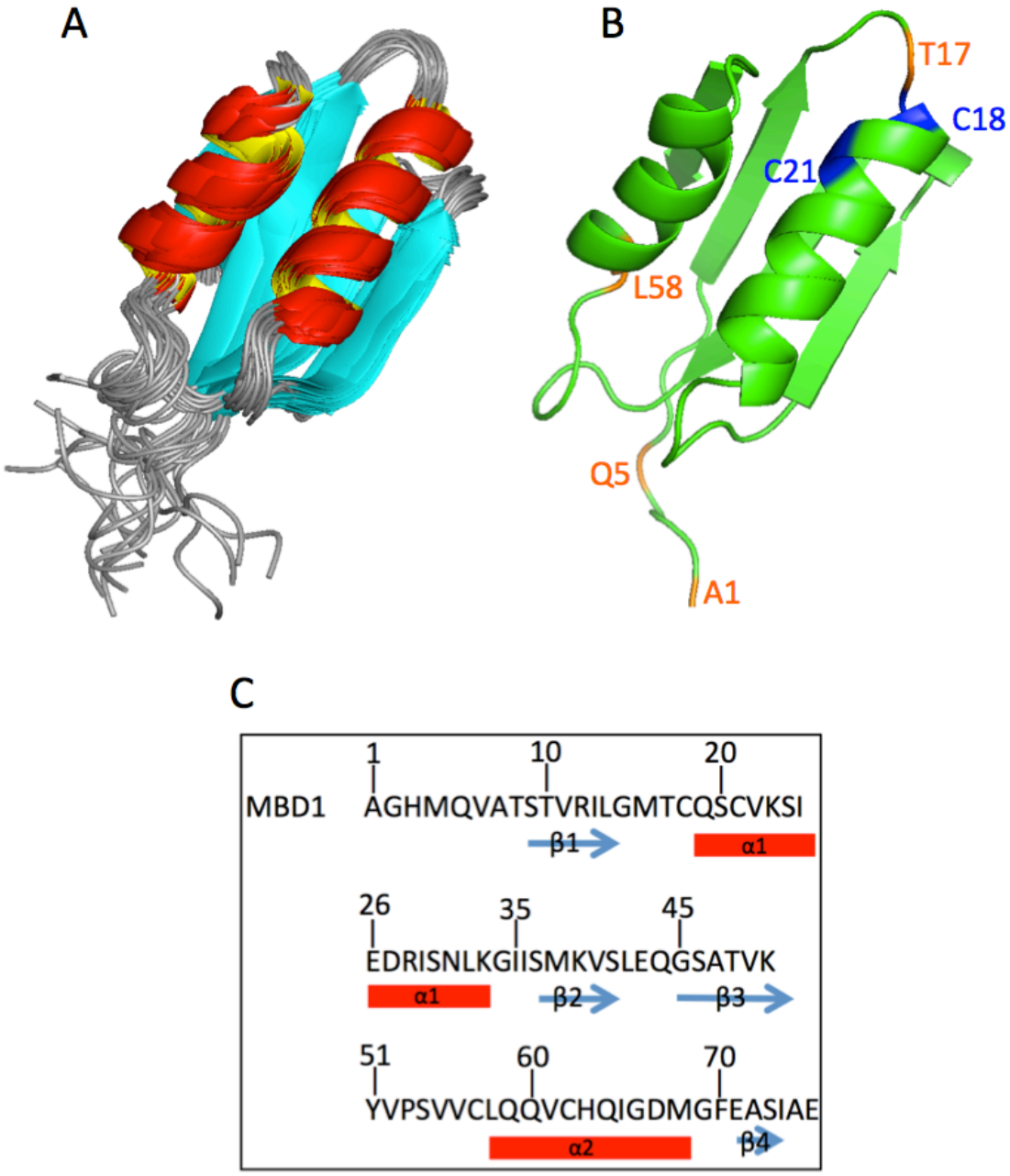

Figure 4.4: Structure determination of MBD1. (A) The structural ensemble of MBD1 with the α-helices in red-yellow and the β-sheets in blue. (B) Ribbon diagram showing the CxxC motif (*blue*) and the location of the unassigned backbone residues (*orange*). (C) Amino acid sequence of MBD1 with secondary structural elements shown.

Table 4.1: Statistics for the structure calculation of MBD1.

Parameter	Value
Total number of NOE distance restraints	628
Intra-residue	305
Sequential (|i – j| = 1)	143
Medium range (|i – j| < 5)	49
Long range (|i – j| > 5)	91
Hydrogen bond restraints	40
Dihedral angle constraints	119
Phi (ϕ)	54
Psi (ψ)	65
RMSD for bond angles (°)	0.6
RMSD for bond lengths (Å)	0.008
RMSD from experimental restraints	
NOE (Å)	0.016 ± 0.002
Dihedral angles (°)	0.452 ± 0.008
Mean NOE violations larger than 0.25 Å	0
Maximum NOE violation (Å)	0.27
Average RMSD to the mean (Å)	
Backbone	0.15
All heavy atoms	0.24
PROCHECK Z-scores (ϕ an ψ/all dihedral angles)	1.14/1.12
MolProbity clash score/Z-score	13.88/-0.86
Ramachandran plot summary from PROCHECK (%)	
Residues in most favorable regions	97.3
Residues in additionally allowed regions	2.7
Residues in disallowed regions	0.0
Ramachandran plot summary from MolProbity (%)	
Residues in most favorable regions	99.4
Residues in additionally allowed regions	0.6
Residues in disallowed regions	0.0
Average number of angle constraint per conformer (>5°)	0

We analyzed the Cu(I) binding residues of MBD1, which aided in the assignment of unknown backbone amides for MBD1. Copper(I) chloride was titrated at various ratios into ^{15}N-labeled MBD1, and Cu(I) binding was monitored by chemical shift perturbation analysis. Consistent with the other MBDs, Cu(I) binds to MBD1 in the slow exchange regime, which indicates a tight binding affinity (Figure 4.5; top left). To assess the structural effects of Cu(I) binding on MBD1, the combined ^{1}H-^{15}N chemical shift changes were quantified as a function of amino acid residue (Figure 4.5; middle left) and mapped onto the solved NMR structure (Figure 4.5; bottom). Consistent with the other MBDs, Cu(I) binding to MBD1 caused significant chemical shift changes in the CxxC motif and a few adjacent residues (Figure 4.5; bottom left). However, comparing the effects of copper binding to MBD2, copper binding to MBD1 also affected residues in the N-terminal region of α2.

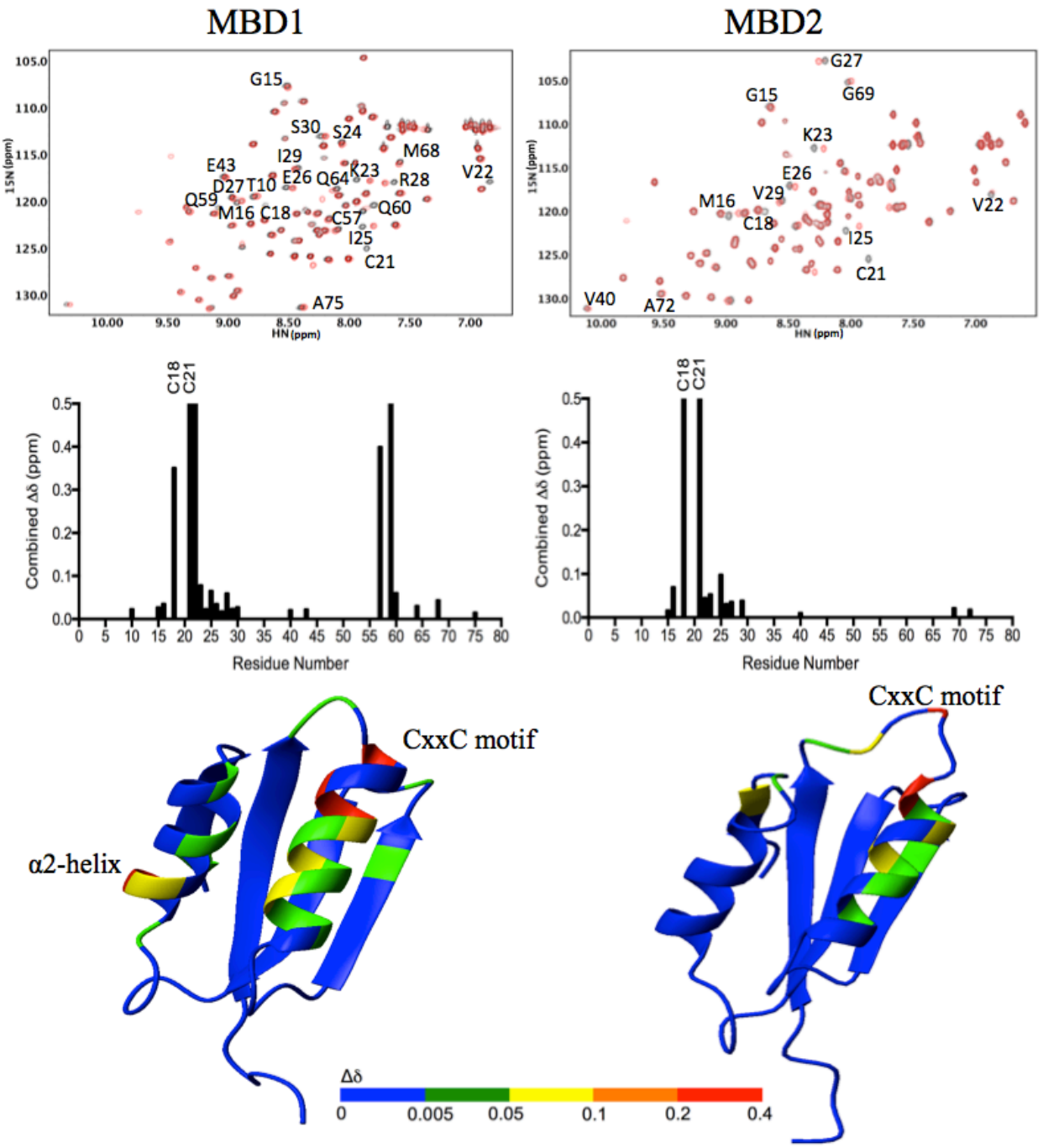

Figure 4.5: Copper binding to MBD1 (left) and MBD2 (right) analyzed by ^{1}H, ^{15}N-HSQC spectroscopy. (Top) Overlay of apo- (black) and copper-bound (red) MBD1 and MBD2 with assignments of peaks showing significant copper-dependent chemical shift changes; (Middle) Combined chemical shift changes caused by copper binding as a function of amino acid residue number. (Bottom) Regions of the MBD1 and MBD2 structure affected by copper binding.

4.3 Transient interactions of metal-binding domains revealed by nanobody binding.

4.3.1 Identification of nanobody-binding sites in MBD1-6

In order to understand the molecular mechanism of copper acquisition and regulation of ATP7B, we analyzed MBD1-6, the protein construct with all six MBDs. Although NMR is often limited to smaller proteins compared to X-ray crystallography, it can provide important information on protein dynamics. We characterized the dynamics of MBD1-6 by measuring the NMR relaxation parameters: spin-lattice relaxation (R_1), transverse relaxation (R_2), and heteronuclear NOE. Using these NMR relaxation parameters, we calculated a correlation time (τ_c) for each MBD. The correlation time is the average time it takes a molecule to rotate one radian (Reddy and Rainey, 2010). For a compact globular protein, the correlation time is approximately proportional to its molecular weight (Reddy and Rainey, 2010).

Previous biochemical studies using AxxA mutant variants of MBD2 or MBD3 demonstrated a total loss of copper binding in MBD1-6 (LeShane et al., 2010). This result suggests that inter-domain communication of the MBDs regulates the conformation and function of the entire N-terminal region. However, the NMR data offer a different conclusion from the biochemical studies. The narrow peaks in the ^{1}H, ^{15}N TROSY spectrum of MBD1-6 indicate independent tumbling of the individual MBDs. This suggests that MBD1-6 represents a "beads-on-a-string" model. The rotational correlation times (τ_c) of the individual MBDs in the context of MBD1-6 range from 5.52 ns to 7.83 ns (Table 4.3). These values are more consistent with independent tumbling of isolated MBDs than a compact globular protein of 66 kDa, which would have a τ_c of ~30 to 40 ns (Dayie et al., 1996). We hypothesized that these domain-domain interactions observed in biochemical studies are transient.

To identify possible domain-domain interactions, nanobodies were used to probe the backbone dynamics of MBD1-6 (Figure 4.6). Nanobodies are 12-15 kDa recombinant single-domain antibodies derived from the heavy-chain antibodies found in the *Camelidae* species (see section 2.6.1) (Muyldermans, 2013). We have identified the binding sites for a panel of nanobodies against MBD1-6. Using established NMR chemical shift assignments and chemical shift perturbation analysis, we characterized a total of 16 nanobodies that bind to MBD1-6 and determined that 3 nanobodies bind to MBD3, 13 nanobodies to MBD4 (Table 4.2), and none to

any other MBDs. We subsequently estimated the nanobody-binding affinities using NMR by analyzing the chemical exchange of the MBD residues affected by nanobody binding. Residues that are involved in nanobody binding can either undergo slow, intermediate, or fast exchange (see section 2.5.4). Slow exchange is correlated with tight binding (K_D < 1 μM) and is manifested by two distinct peak signals, corresponding to the free- and ligand-bound forms in the NMR spectrum. In contrast, fast exchange is associated with weak binding (K_D > 100 μM). In the fast exchange regime, only one peak is observed. Intermediate exchange is correlated with a moderate binding affinity (K_D ~ 1-100 μM) and is observed by the broadening of peaks and even complete signal disappearance. The nanobodies against MBD3 have a moderate to tight binding affinity, whereas nanobodies against MBD4 show a wide range of binding affinities (Table 4.2).

Since complete MBD1-6 was used for immunization, the original cDNA library should contain nanobodies against all the MBDs of MBD1-6. However, in the initial selection process, only nanobodies against MBD3 or MBD4 were isolated. This may suggest that MBD3 and MBD4 are more exposed in full-length MBD1-6, leading to higher immunogenicity of these domains.

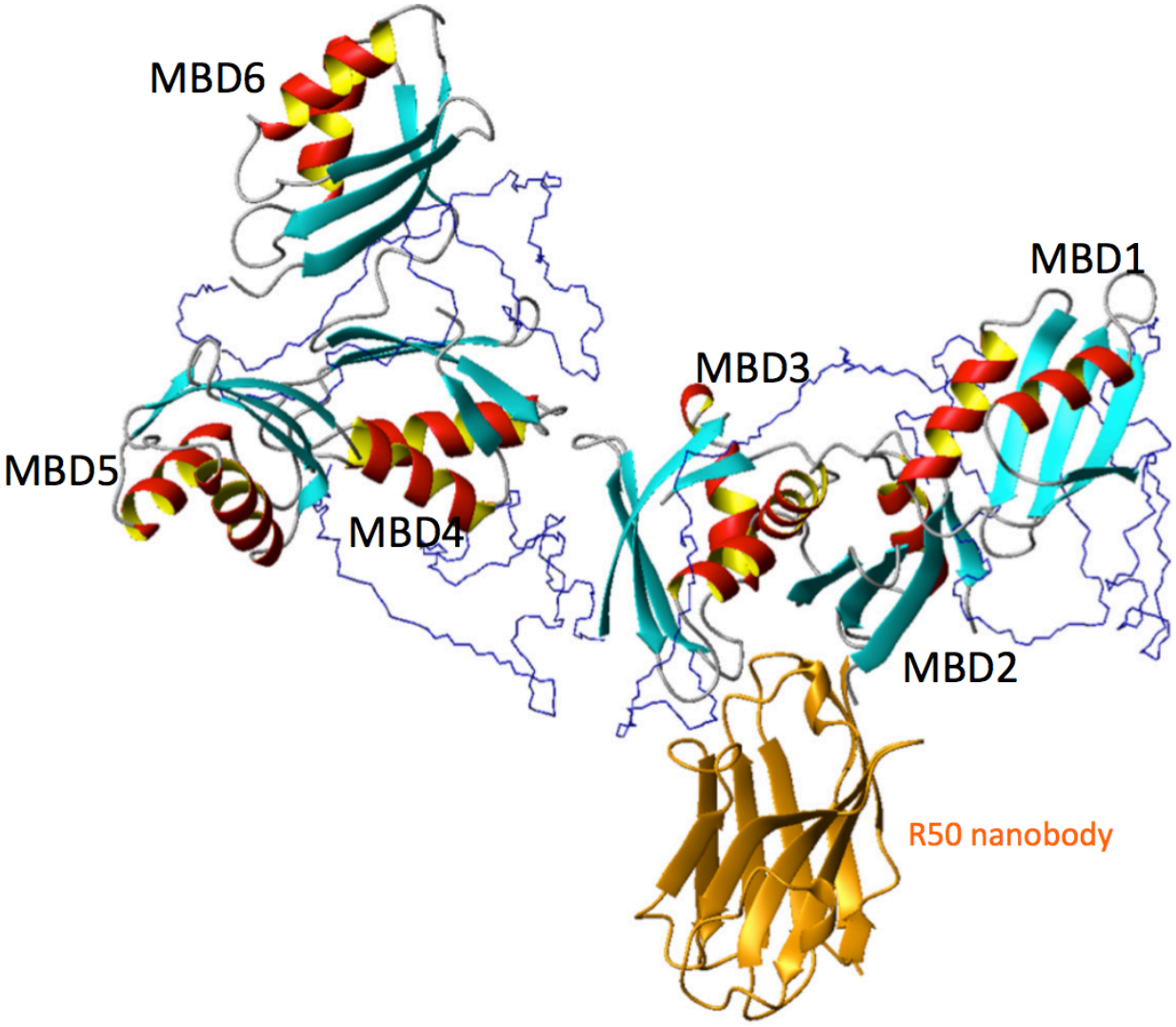

Figure 4.6: A model for the panel of nanobodies that were generated against MBD1-6.

Table 4.2: Summary of nanobody properties. Nanobodies are divided into groups based on the target domain (MBD3 or MBD4) and binding affinity (tight, K_D < 1 μM; moderate, K_D ~ 1-100 μM; weak, K_D > 100 μM).

Nanobody Group	Nanobody	Target Domain	Binding Affinity
1	R50	MBD3	Tight
	2R1	MBD3	Moderate
	2R16	MBD3	Moderate
2	1R1	MBD4	Tight
	1R15	MBD4	Tight
	1R20	MBD4	Tight
3	5A51	MBD4	Moderate
	4A19	MBD4	Moderate
	2R2	MBD4	Moderate
	2R26	MBD4	Moderate
	2R54	MBD4	Moderate
	2R28	MBD4	Moderate
4	R21	MBD4	Weak
	2R7	MBD4	Weak
	2R8	MBD4	Weak
	2R27	MBD4	Weak

Chemical shift perturbation analysis was also used to determine the specific nanobody-binding site on the target MBD. In the ELISA assay, the R21 nanobody bound to apo- and copper-bound ATP7B equally well, whereas the R50 nanobody showed a preference for copper-bound ATP7B (*data not shown*). In our analysis, we determined the specific binding epitopes of two nanobodies, R50, against MBD3 (Fig 4.7A) and R21, against MBD4 (Fig 4.7B). The R50 nanobody caused chemical shift changes mostly in the C-terminal region of α1 and the adjacent loop connecting α1 to β2 of MBD3 (Fig 4.7C). In contrast, R21 nanobody binding to MBD4 caused small chemical shift changes in the loop connecting β2 and β3 (Fig 4.7D). Since R21 nanobody binding to MBD4 was weak, we did not use it for subsequent relaxation studies.

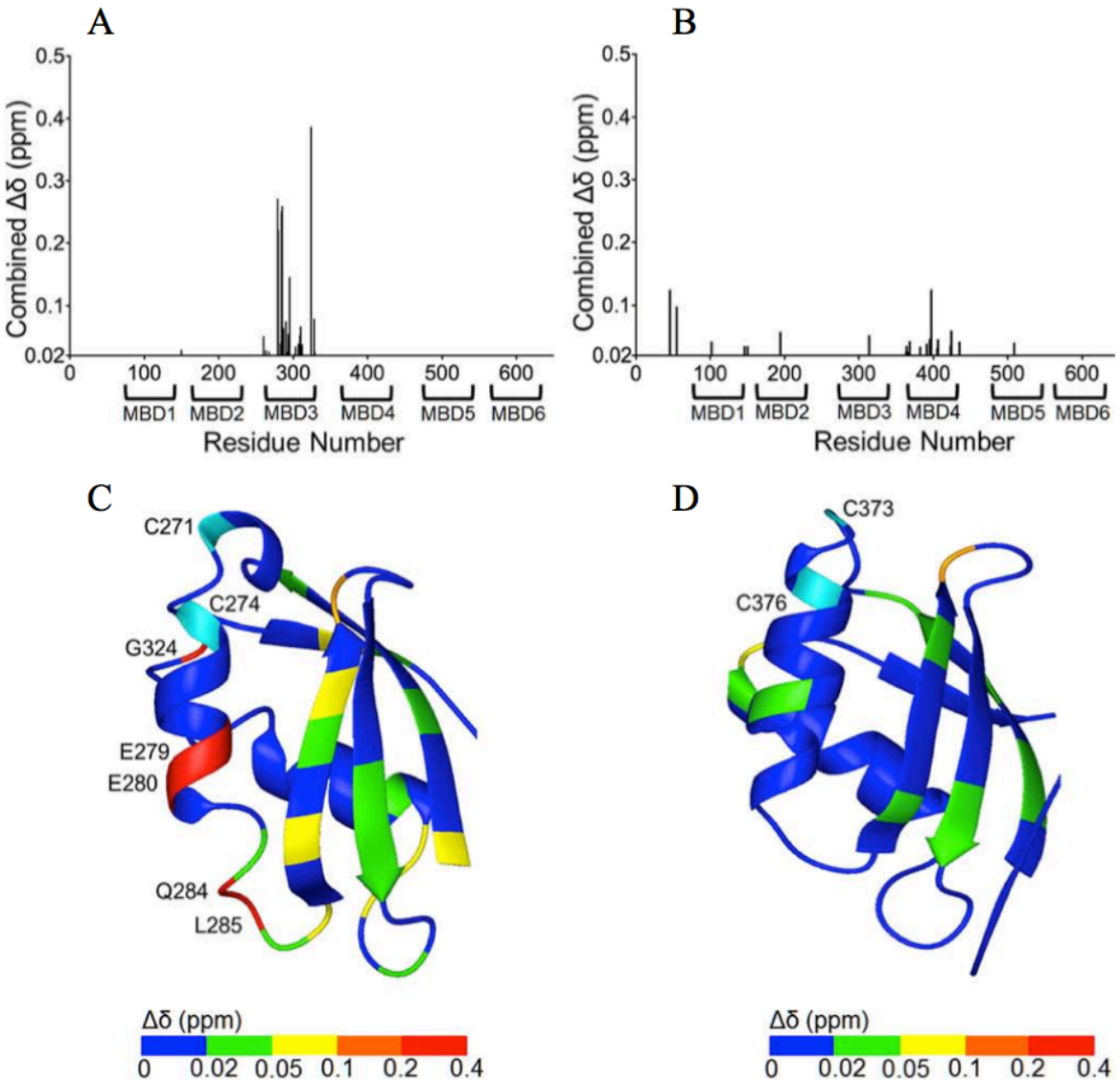

Figure 4.7: Binding sites of the R50 and R21 nanobodies. Chemical shift changes caused by (A) R50 and (B) R21 nanobody binding to MBD1-6 as a function of amino acid residue number. Regions of (C) MBD3 and (D) MBD4 that are affected by R50 and R21 nanobody binding, respectively.

4.3.2 Nanobody binding to MBD3 and MBD4 caused distinct effects on MBD1-6 dynamics.

We used nanobodies to probe the backbone dynamics of MBD1-6 to gain insight into the dynamics and inter-domain interactions of the MBDs. For these studies, we selected two high-affinity nanobodies, one that binds to MBD3 (R50), and the other to MBD4 (1R1). Transverse relaxation is influenced by the molecular motions of surrounding spins and hence, is an accurate indicator of protein dynamics (Reddy and Rainey, 2010). We measured the difference in transverse relaxation rates (R_2) of each individual domain in the context of full-length MBD1-6 in the free- and nanobody-bound forms (Figure 4.8A). In the presence of R50, the transverse relaxation rate of MBD3 increased, which is consistent with the increased molecular mass of the MBD3-nanobody complex (Figure 4.8B). Unexpectedly, the relaxation rates of MBD1-2 significantly decreased, whereas MBD4-6 remained relatively unaffected. This indicates that transient interactions exist between MBD1, MBD2, and MBD3 and that these interactions were disrupted by R50 binding to MBD3, increasing the mobility of MBD1 and MBD2. In contrast, 1R1 significantly decreased the mobility of MBD4 and a lesser extent to the other MBDs (Figure 4.8A). This suggests that the slower tumbling of nanobody-bound to MBD4 partially propagated to the other domains of ATP7B (Figure 4.8B).

The measurements of transverse relaxation suggest a differential effect of nanobodies on MBD mobility. This was confirmed by calculating the τ_c for each individual MBD from the R_2 and R_1 measurements (Table 4.3). If MBD1-6 (66 kDa) was a compact globular protein, the expected τ_c MBD would be ~30-40 ns. In contrast, if MBD1-6 represented a "beads-on-a-string" model, the expected τ_c for each individual MBD in the context of MBD1-6 would be similar to the τ_c measured for isolated MBDs, around ~4.5-6 ns (Anastassopoulou et al., 2004; Banci et al., 2008; Fatemi et al., 2010; Huang et al., 2014). The correlation times that we calculated for the individual MBDs in the context of full-length MBD1-6 ranged from 5.5 ns to 7.8 ns. This indicates that the dynamics of the individual MBDs are largely independent. However, the τ_c for MBD1 (7.83 ns), MBD2 (7.5 ns), and MBD5 (7.19) were slightly higher than those of isolated MBDs. This may indicate that inter-domain interactions could be involved. We also observed differences in tumbling times for the individual domains that were affected by R50 nanobody

binding. When the R50 nanobody binds, the τ_c of MBD3 increased from 6.3 ns to 8.26 ns, which is consistent with increased molecular mass. In contrast, the τ_c of MBD1 and MBD2 decreased from ~7.5 ns to 5.5 ns, which is consistent with increased motional freedom. The calculated τ_c values agree with the transverse relaxation behavior described for the individual MBDs.

Table 4.3: The correlation times of the individual metal-binding domain in the context of MBD1-6.

Domain	Structure PDB	Correlation time (τ_c), ns	
		Free	+R50
MBD1	2N7Y	7.83 ± 0.32	5.65 ± 0.11
MBD2	2LQB	7.65 ± 0.35	5.63 ± 0.18
MBD3	2ROP	6.37 ± 0.28	8.26 ± 0.68
MBD4	2ROP	5.97 ± 0.26	5.44 ± 0.08
MBD5	2EW9	7.19 ± 0.24	6.94 ± 0.19
MBD6	2EW9	5.52 ± 0.08	5.17 ± 0.08

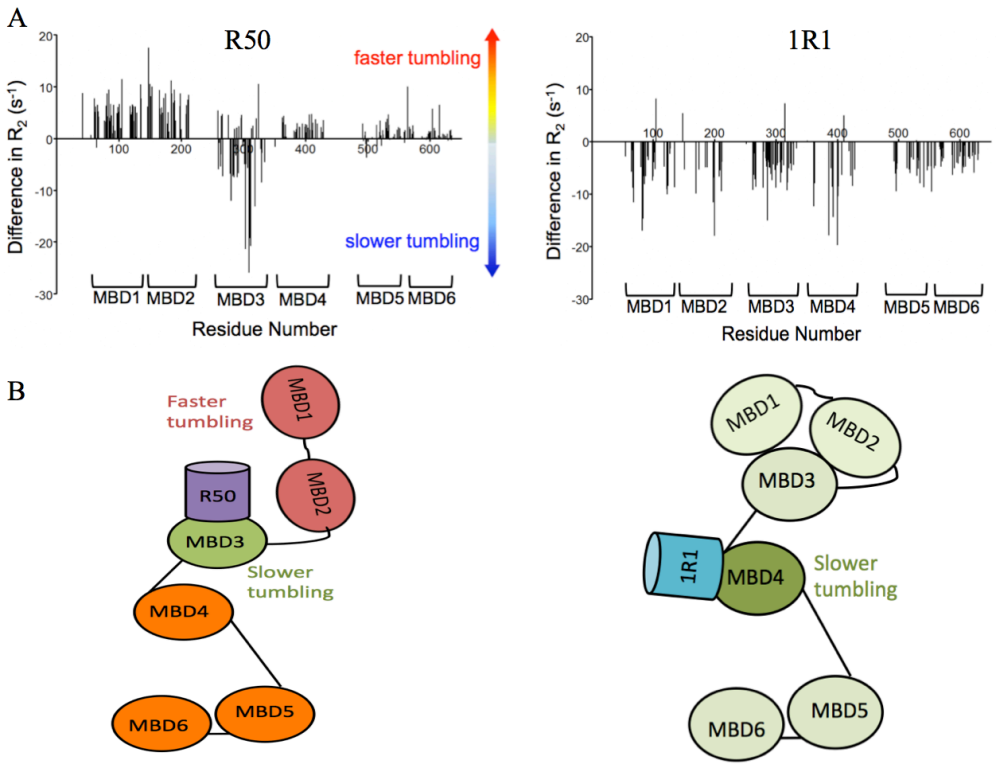

Figure 4.8: Transverse relaxation rate of MBD1-6 bound to R50 or 1R1 nanobody. The difference between the transverse relaxation rates R_2 in the absence and presence of the R50 and 1R1 nanobody plotted as a function of residue sequence number. (B) Model of MBD1-6 indicating the change in dynamics of the individual MBDs when R50 or 1R1 nanobody binds.

4.4 MBD1-3 adopts a unique S-shaped conformation

Transverse relaxation studies of MBD1-6 with the R50 nanobody have demonstrated correlated dynamics of MBD1-3 that were distinct from the rest of the N-terminal region. We propose that the N-terminal region of ATP7B is composed of two sets of correlated domains, MBD1-3 and MBD5-6. The solution structure of MBD5-6 is connected by a short-linker of four amino acids and NMR relaxation measurements indicate that MBD5-6 tumbles as a rigid dumbbell (Achila et al., 2006). Since the copper-binding sites of MBD5 and MBD6 face away from each other, copper transfer between these domains is not likely. An alternative mechanism would involve copper transfer from MBD1-3 to MBD5-6. However, there is currently no structural or dynamic information for MBD1-3. We hypothesized that transient interactions exist within MBD1-3. If MBD1-3 (29 kDa) is a compact globular protein, the expected τ_c would be ~15-17 ns. In contrast, if the dynamics of MBD1-3 are completely independent, the expected τ_c would be ~4.5-6 ns, similar to those of isolated MBDs. The calculated τ_c of the individual MBDs in MBD1-3 range from 6.37 ns to 7.83 ns (Table 4.3). These values are slightly higher than those of isolated MBDs, which may suggest that the individual MBDs in MBD1-3 are highly mobile with some inter-domain interactions involved. This increased mobility is supported by the narrow resonances in the ^{1}H-^{15}N HSQC spectrum of MBD1-3 (Figure 4.9). Therefore, we used a combination of SAXS and molecular modeling as preliminary experiments to analyze the conformation of MBD1-3.

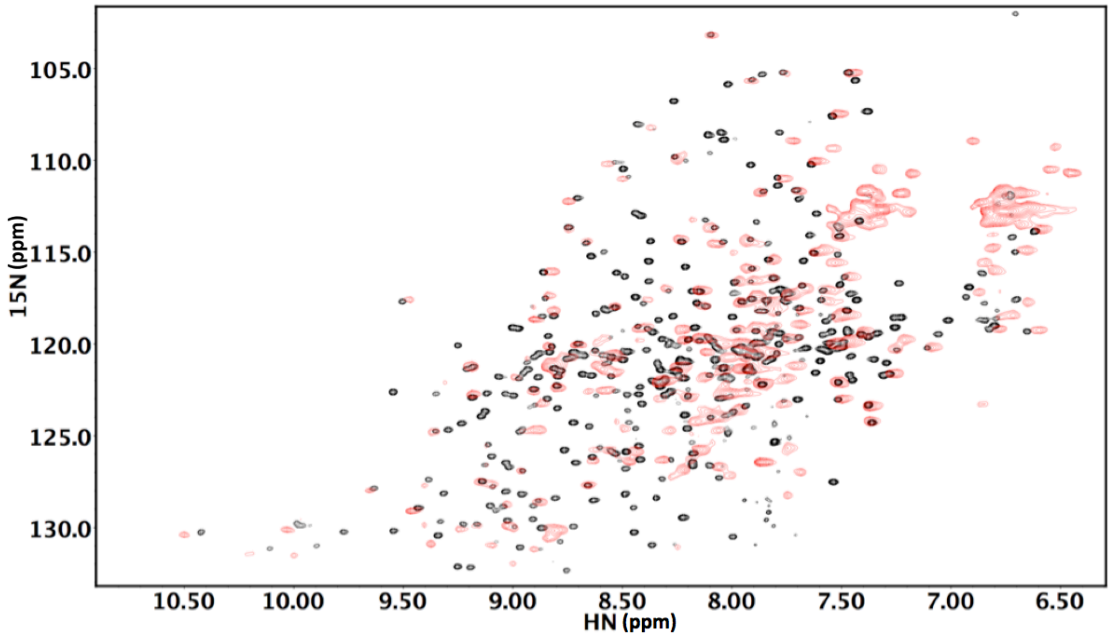

Figure 4.9: ^{1}H-^{15}N overlay of MBD1-6 TROSY spectrum (*black*) recorded at 900 MHz and MBD1-3 HSQC spectrum (*red*) recorded at 600 MHz.

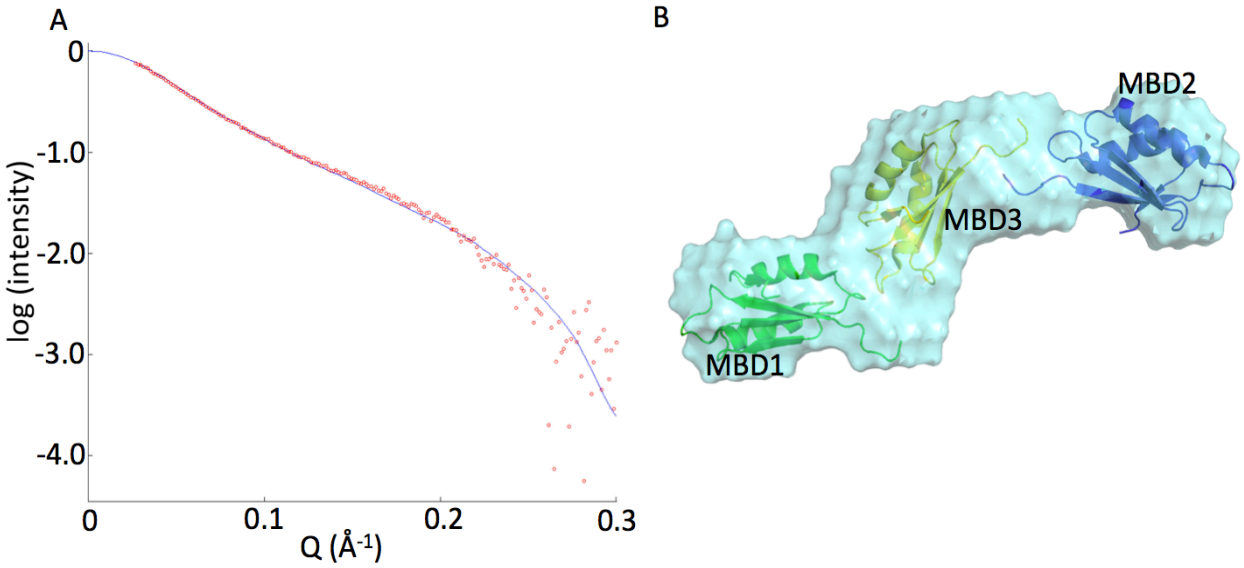

Figure 4.10: The envelope of MBD1-3 determined by SAXS. (A) The buffer-subtracted 1D scattering curve of apoMBD1-3. (B) The surface representation of MBD1-3 generated from *ab initio* modeling. The structures of individual MBD1-3 were manually fitted into the surface representation, based on the experimental nanobody relaxation data and chemical shift perturbation analysis.

SAXS is a low-resolution technique that was used to determine the overall shape of MBD1-3 in solution state. The optimal scattering data was collected on a monodisperse sample

for apoMBD1-3 at 2.0 mg/mL. The Guinier region was extracted from the 1D scattering curve and measured a radius of gyration (R_g) of 31.4 Å (Figure 4.10A). From the 1D scattering curve, *ab initio* modeling showed that the overall fold of MBD1-3 is S-shaped (Figure 4.10B). We manually fitted the positions of the MBDs based on the interpretation of correlation time changes observed in the nanobody experiments. In the absence of R50 nanobody, the correlation times for MBD1 and MBD2 were ~7.7 ns. When the R50 nanobody was bound to MBD3, the τ_c for both MBD1 and MBD2 decreased to ~5.6 ns, which is close to the τ_c of 4.5 ns observed for an isolated MBD. This suggests that MBD1 and MBD2 do not interact with each other, but each of them interacts with MBD3. To map contacts between the domains, we analyzed pairwise domain interactions by NMR and molecular modeling.

Domain-domain interactions between metal-binding domains 1, 2, and 3 were determined using chemical shift perturbation analysis. Chemical shifts are highly sensitive indicators of the changes in the chemical environment of a given spin. To analyze the contact surface of MBD1-3, we purified MBD1, MBD2, and MBD3 in both the unlabeled and ^{15}N-labeled form. We measured chemical shift changes in the ^{1}H, ^{15}N-HSQC spectrum of each MBD caused by the addition of each of the other two MBDs in the unlabeled form. For example, we recorded the ^{1}H, ^{15}N-HSQC spectra of MBD1 with no addition, and either unlabeled MBD2 or unlabeled MBD3. We observed reciprocal interaction between MBD1 and MBD3. The interaction between MBD1 and MBD3 mainly affected the residues in the CxxC copper-binding motif. Additionally, the copper-binding residues of ^{15}N MBD2 were affected by the interaction of unlabeled MBD1 or MBD3. Surprisingly, unlabeled MBD2 caused no changes in the spectrum of ^{15}N-MBD1 or ^{15}N-MBD3 (Table 4.4). We were not able to use MBD2 in our molecular modeling because of the lack of consistent chemical shift perturbation data in our preliminary experiments.

We used NMR chemical shift perturbation data to dock MBD1 and MBD3 using HADDOCK, a molecular modeling program that uses experimental data at the protein-protein interface to drive the docking of two proteins (de Vries et al., 2010). Based on the docked model, the cysteines in the copper-binding motif appear to be in close proximity to each other (Figure 4.11). This close proximity of the copper-binding sites has been suggested to determine

the oxidation state and conformation of the entire N-terminal region (LeShane et al., 2010). This molecular model of MBD1-MBD3 also agrees with our S-shaped envelope that we measured with SAXS. HADDOCK was not used for the domain pair MBD1-MBD2 because our NMR relaxation data suggest that interactions between these two domains are negligible. In addition, the domain pair MBD2-MBD3 was not modeled because of insufficient restraints.

Table 4.4: Domain-domain interactions were analyzed by ^{1}H, ^{15}N NMR spectroscopy. Affected residues in the ^{15}N partner protein were recorded and used an input in the program, HADDOCK.

Domain-Domain interactions		**Affected Residues**
Labeled partner (^{15}N)	**Unlabeled partner (^{14}N)**	
MBD1	MBD2	Not observed
MBD1	MBD3	G15, C18, Q19, C21, V22, V40, L42, C57, Q60
MBD2	MBD1	C18, C21, V22, S23
MBD2	MBD3	C18, C21, V22, S23
MBD3	MBD1	R15, C21, C24, L45
MBD3	MBD2	Not Observed

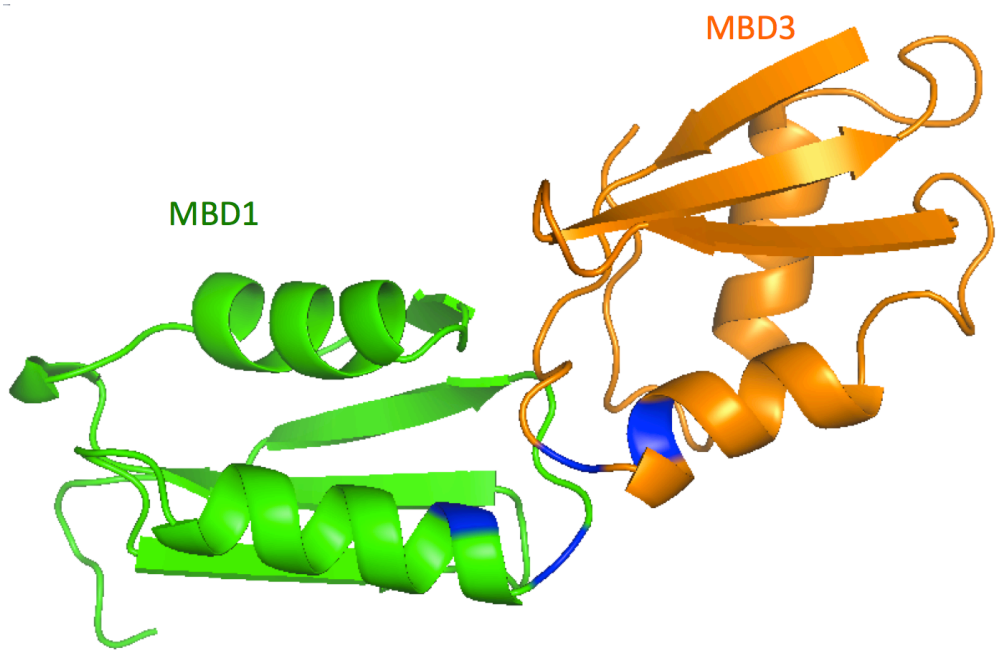

Figure 4.11: The molecular docking of MBD1 (*green*) and MBD3 (*orange*). The copper-binding motifs are highlighted (*blue*).

4.5 Interaction with Atox1-Cu changes domain dynamics and disrupts MBD1-MBD2 association.

4.5.1 Atox1 does not require copper to interact with the metal-binding domains.

Atox1 is a chaperone that delivers copper to the MBDs of ATP7B in the cell and has been shown to regulate copper transport activity of ATP7B. Atox1 was shown to bind and transfer Cu(I) specifically to MBD2 in the context of full-length MBD1-6 (Walker, 2004). To determine whether Cu(I) was required for Atox1 to interact with the MBDs, we investigated the interaction of *apo*-Atox1 with MBD1-6. Unlabeled Atox1 was added at a 6:1 molar ratio to ^{15}N-MBD1-6. Based on the lack of distinct chemical shift changes in the ^{1}H, ^{15}N-TROSY spectrum, stable binding of *apo*-Atox1 to MBD1-6 was not observed (Figure 4.12). Rather, we used NMR relaxation to determine whether the mobilities of specific MBDs changed in the presence of *apo*-Atox1. We measured the difference in transverse relaxation rates (R_2) of the individual MBDs in the absence and presence of *apo*-Atox1. We demonstrate that the addition of *apo*-Atox1 significantly increased the relaxation rates of MBD1 and MBD2, and a lesser extent to other MBDs (Figure 4.13). The large decrease in mobility for MBD1 and MBD2 indicate Atox1-MBD interaction and is consistent with an increased molecular mass of the complex. Since Atox1 can dock and transfer Cu(I) specifically to MBD2 (Walker, 2004), it can be hypothesized that MBD2 is also the main target of *apo*-Atox1.

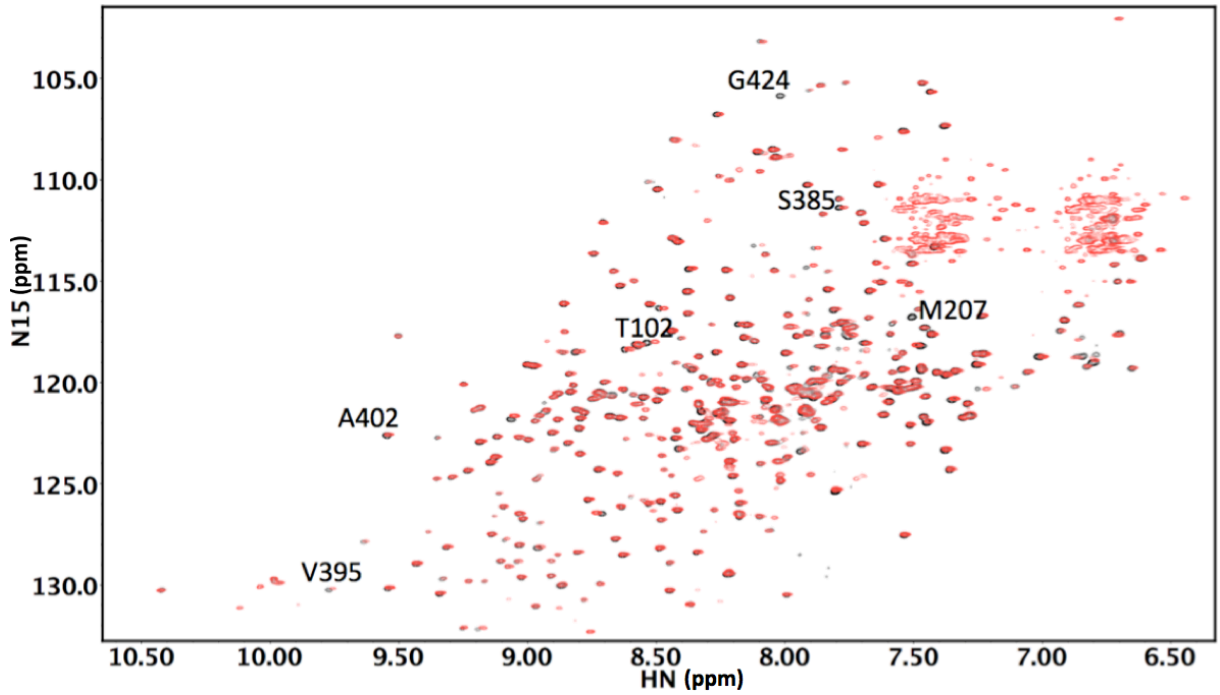

Figure 4.12: Interaction of *apo*-Atox1 with MBD1-6 analyzed by ^{1}H, ^{15}N-HSQC spectroscopy. Overlay of ^{15}N MBD1-6 in the absence (*black*) and presence (*red*) of *apo*-Atox1. The labeled residues in the spectrum crrespond to free MBD1-6.

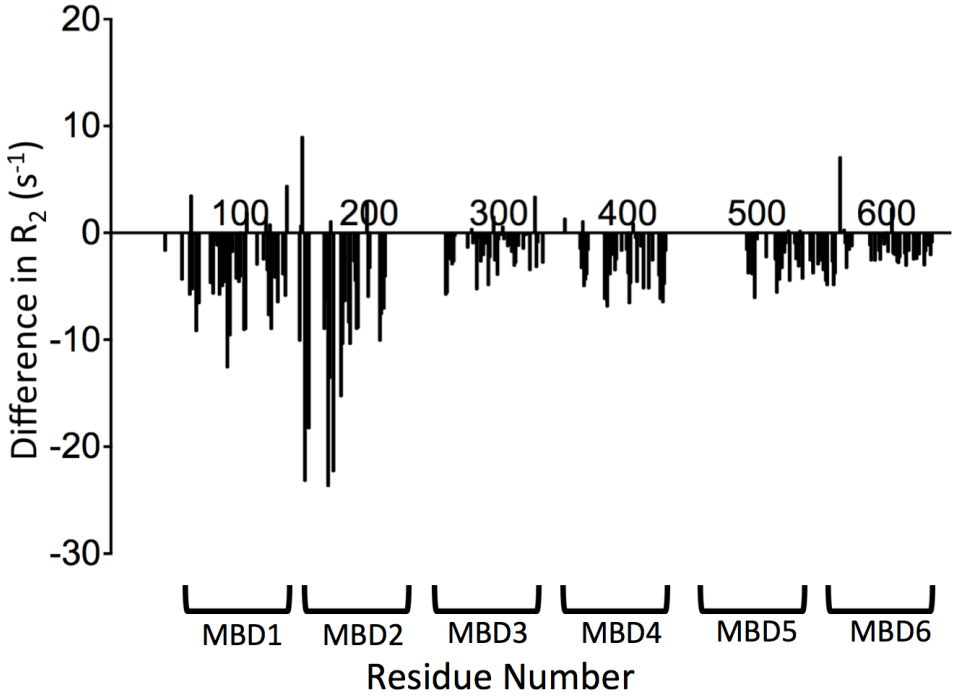

Figure 4.13: Transverse relaxation rate of MBD1-6 bound to *apo*-Atox1. The difference between the transverse relaxation rates R2 in the absence and presence of *apo*-Atox1 plotted as a function of residue sequence number.

4.5.2 Copper(I) transfer from Atox1 to MBD1-6 increases mobility of MBD1-3.

We have used nanobodies to probe the backbone dynamics of MBD1-6. We hypothesized that transient interactions exist between MBD1-3 and that Cu(I) transfer from Atox1 to MBD2 disrupts these weak inter-domain interactions, in a similar mechanism to R50 nanobody binding to MBD3. To test the Cu(I)-dependent conformational changes in MBD1-6, unlabeled Atox1 was pre-treated with Cu(I) at an equimolar molar ratio and subsequently added to MBD1-6 at a 6:1 molar ratio. We observed several chemical shift changes in MBD1-6, confirming that Cu(I) was transferred from Atox1 to MBD1-6 (Figure 4.14A). The changes in MBD dynamics were measured using NMR relaxation analysis. We measured the difference in transverse relaxation rates (R_2) of the individual MBDs in the absence and presence of Atox1-Cu. We demonstrate that the transfer of Cu(I) from Atox1 to MBD1-6 caused differences in the dynamics of individual MBDs. The transfer of copper from Atox1 to MBD1-6 caused increased mobility of MBD1 and MBD2, and to a lesser extent of MBD3, whereas the mobility of MBD4-6 remained relatively unaffected (Figure 4.14B). These results support our hypothesis that transient interactions between MBD1-3 are disrupted when Cu(I) is transferred from Atox1 to MBD2. The copper-dependent conformational changes in the MBD1-3 domain group may be the first step of the regulatory mechanism of copper transport and trafficking activity. These changes are then relayed to the other cytosolic domains of ATP7B.

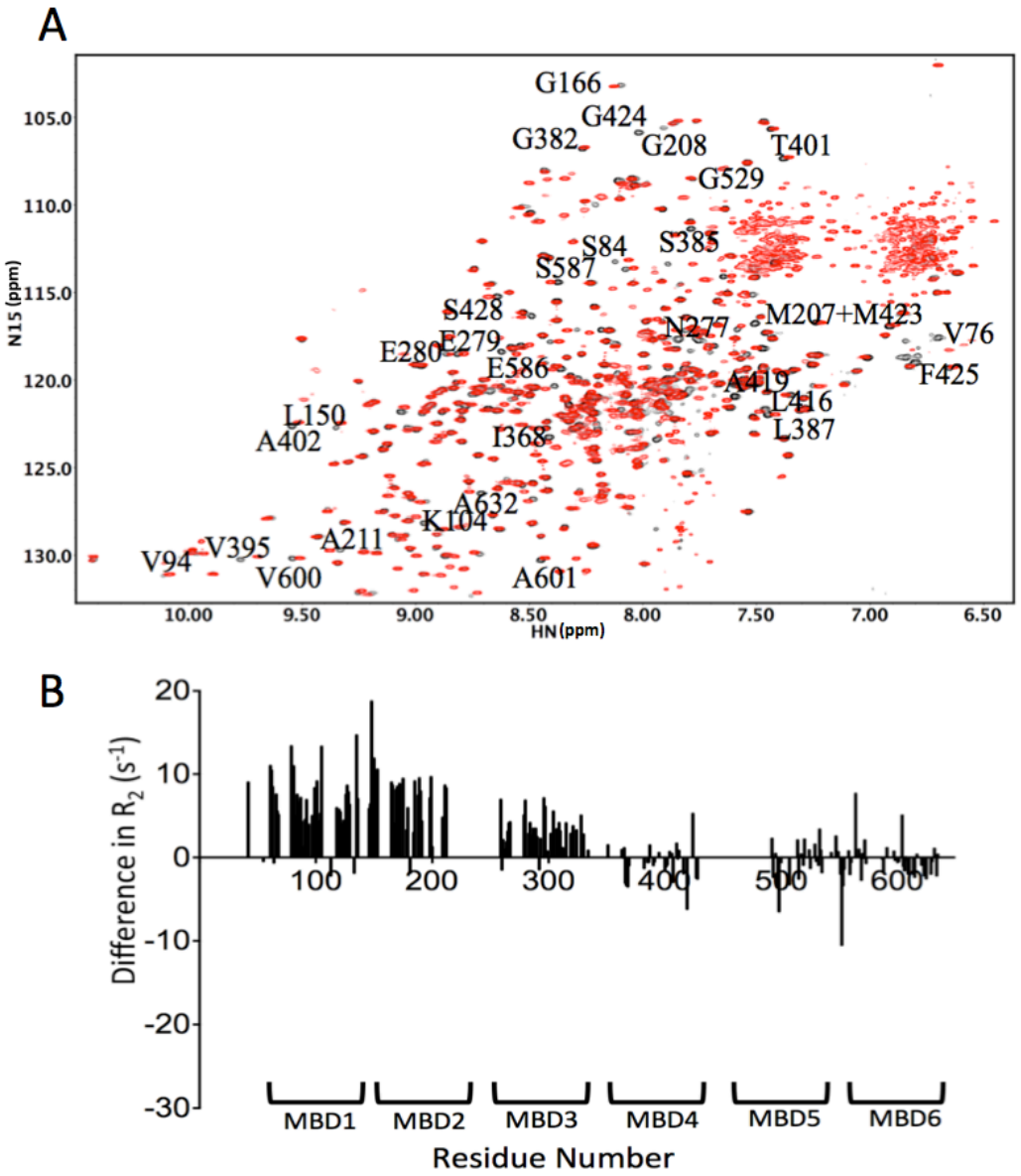

Figure 4.14: Interaction of Atox1-Cu with MBD1-6 analyzed by ^{1}H, ^{15}N-TROSY spectroscopy. A) Overlay of ^{15}N MBD1-6 in the absence (black) and presence (red) of Atox1-Cu. (B) The difference between the transverse relaxation rates R_2 in the absence and presence of Atox1-Cu plotted as a function of residue sequence number.

4.6 Nucleotide-binding and actuator domains do not interact with MBD1-6

The N-terminal region of ATP7B is a characteristic region of heavy metal transporters. The number of MBDs varies from one or two in bacteria to six in humans, which suggests a more complex regulatory function in higher order species. The interaction of MBD1-6 with other cytosolic domains, such as the ATP-binding (ATP-BD) (Tsivkovskii et al., 2000) and actuator domain (Gupta et al., 2011), has been suggested to regulate ATP7B copper transport and trafficking activity. It has been demonstrated that ATP-BD interacts with MBD1-6 in a copper dependent manner (Tsivkovskii et al., 2000). The ATP-BD consists of two sub-domains, the phosphorylation- and nucleotide-binding domains. Copper-free MBD1-6 tightly interacts with ATP-BD, locking ATP-BD in an inhibited conformation. However, copper binding to MBD1-6 decreases this inter-domain interaction, allowing ATP-BD to adopt an active conformation that can readily bind ATP.

To test this hypothesis, we tried to detect interactions between ATP-BD and MBD1-6 and to map the interaction surface by NMR. However, the isolated ATP-BD was unfolded, as evidenced by poor chemical shift dispersion in a ^{1}H-^{15}N HSQC spectrum *(data not shown)*. As an alternative, we tried to determine whether MBD1-6 interacts with the N-domain, the domain responsible for binding ATP (Dmitriev et al., 2006). The rationale for using the N-domain is that the P-domain shows much higher sequence conservation among the different P-type ATPases than the N-domain, which suggests that inter-domain interactions may occur at sequences that are unique to the N-domain of ATP7B. Additionally, the N-domain of human Cu-ATPases has a large flexible loop that may be important for inter-domain interactions. Therefore, it is much more likely that the N-domain, rather than P-domain, would be the site of inter-domain interactions with MBD1-6. In these experiments, unlabeled MBD1-6 was added in equimolar ratio to ^{15}N-labeled N-domain in the absence (Figure 4.15A) and presence of 5 mM ATP (Figure 4.15B). We did not observe any chemical shift changes, which indicates that MBD1-6 does not interact with N-domain under these conditions. This is consistent with the results of another study (Mondol et al., 2016), which reported no interactions between the N-domain and MBD1-4. To explain the discrepancy with the earlier report (Tsivkovskii et al., 2000), a minor population of interacting proteins were detected in the pull-down assay (Mondol et al., 2016). Alternatively,

other proteins that were present in the crude cell lysate, but not in the purified NMR sample, may be required for MBD interaction with the ATP-BD (Mondol et al., 2016).

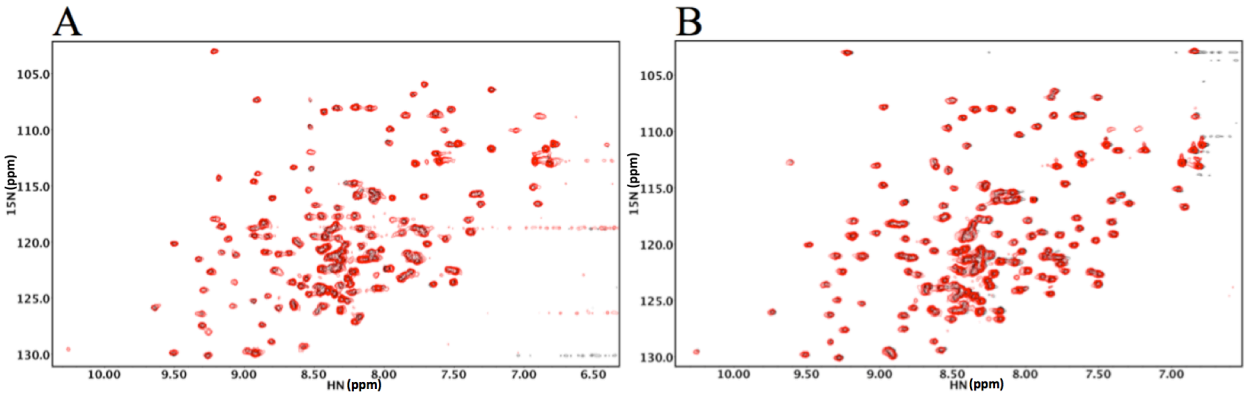

Figure 4.15: Potential interaction of MBD1-6 with the ^{15}N-labeled N-domain of ATP7B tested by ^{1}H, ^{15}N-HSQC spectroscopy. Spectra overlay of the ^{15}N N-domain (black) with MBD1-6 (red) in the (A) absence and (B) presence of 5 mM ATP.

Based on our nanobody and Atox1-Cu relaxation analysis of MBD1-6, a third alternative hypothesis becomes apparent. We propose that the inter-domain interactions between MBD1-3 may shield the sites involved in the interactions with the N-domain. To expose the potential binding sites, we examined the interaction between N-domain and the isolated MBDs 1, 2, and 3 by chemical shift perturbation analysis. Addition of the N-domain caused some chemical shift changes in the spectra of MBD1 (Figure 4.16A) and MBD2 (Figure 4.16B), but not MBD3. Mapping the affected residues onto the solution structures shows that the copper-binding motif was affected in both MBD1 and MBD2 (Figure 4.16CD). In addition, the N-terminal region of α2 was affected in MBD1.

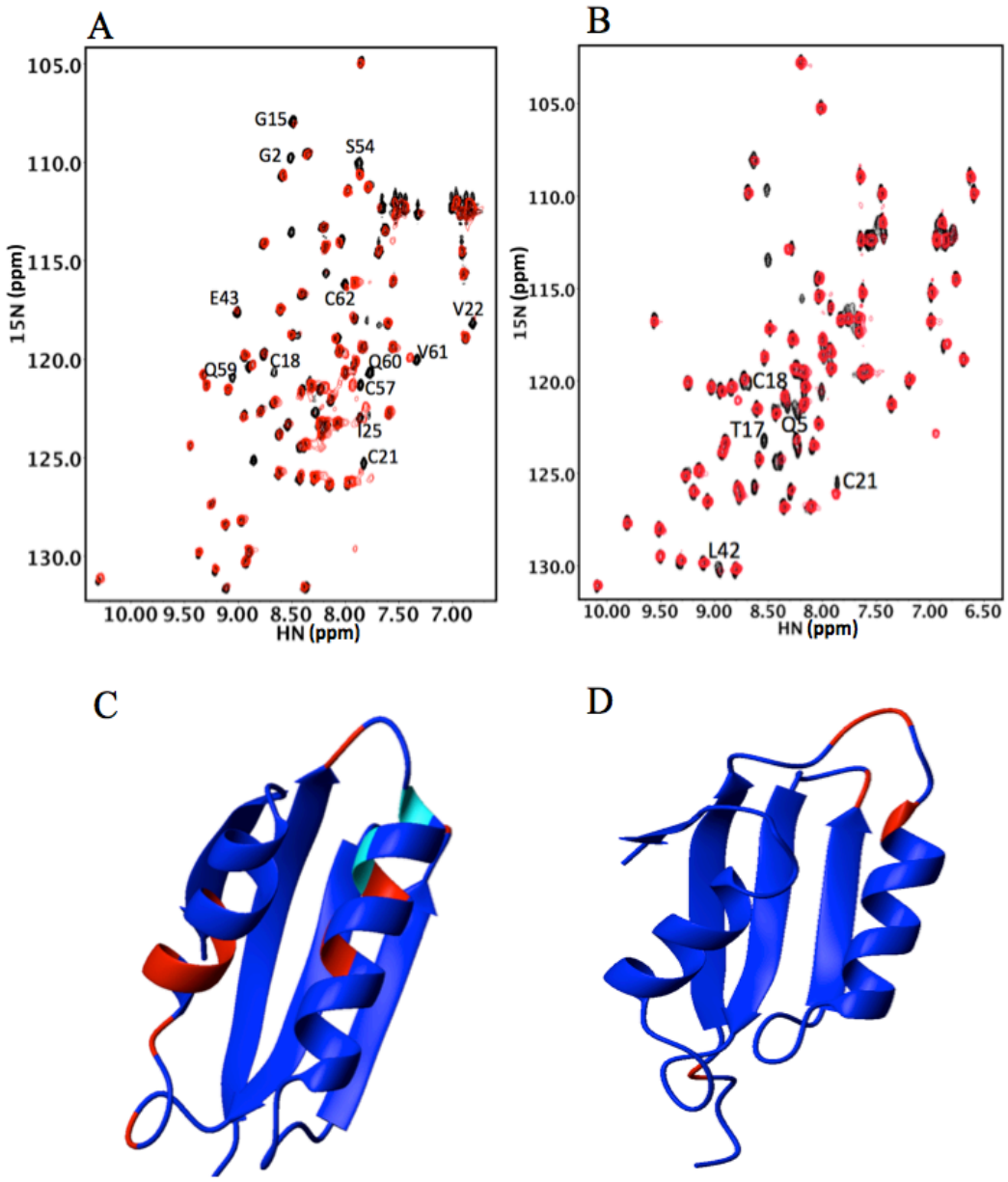

Figure 4.16: Interaction of N-domain with ^{15}N-labeled MBD1 and MBD2. ^{1}H, ^{15}N-HSQC spectra of (A) MBD1 and (B) MBD2 before (*black*) and after (*red*) the addition of N-domain. Regions of (C) MBD1 and (D) MBD2 that are affected by N-domain binding, respectively.

Another study also suggested that MBD1-6 interacts with the A-domain (Gupta et al., 2011). The G875R mutation results in unfolding of the A-domain, causing mislocalization of ATP7B. At the basal copper level, G875R-ATP7B is localized to the endoplasmic reticulum (ER), instead of the TGN. When the copper level in the cell increases, G875R-ATP7B migrates from the ER to the TGN, restoring normal ATP7B copper transport function. Since the G875R-A-domain was unfolded, it was hypothesized that MBD1-6 stabilized G875R-A-domain in a

copper-dependent manner (Gupta et al., 2011). To test this hypothesis, we examined the interaction of MBD1-6 with G875R-A-domain in the absence of copper using ^{1}H, ^{15}N-NMR spectroscopy. No chemical shift changes were observed in either MBD1-6 or G875R-A-domain, demonstrating that MBD1-6 did not interact with G875R-A-domain (Figure 4.17A). We also analyzed the interaction between wild-type A-domain and MBD1-6 (Figure 4.17B) both in the absence and presence of copper and did not observe any spectral changes (Figure 4.17C).

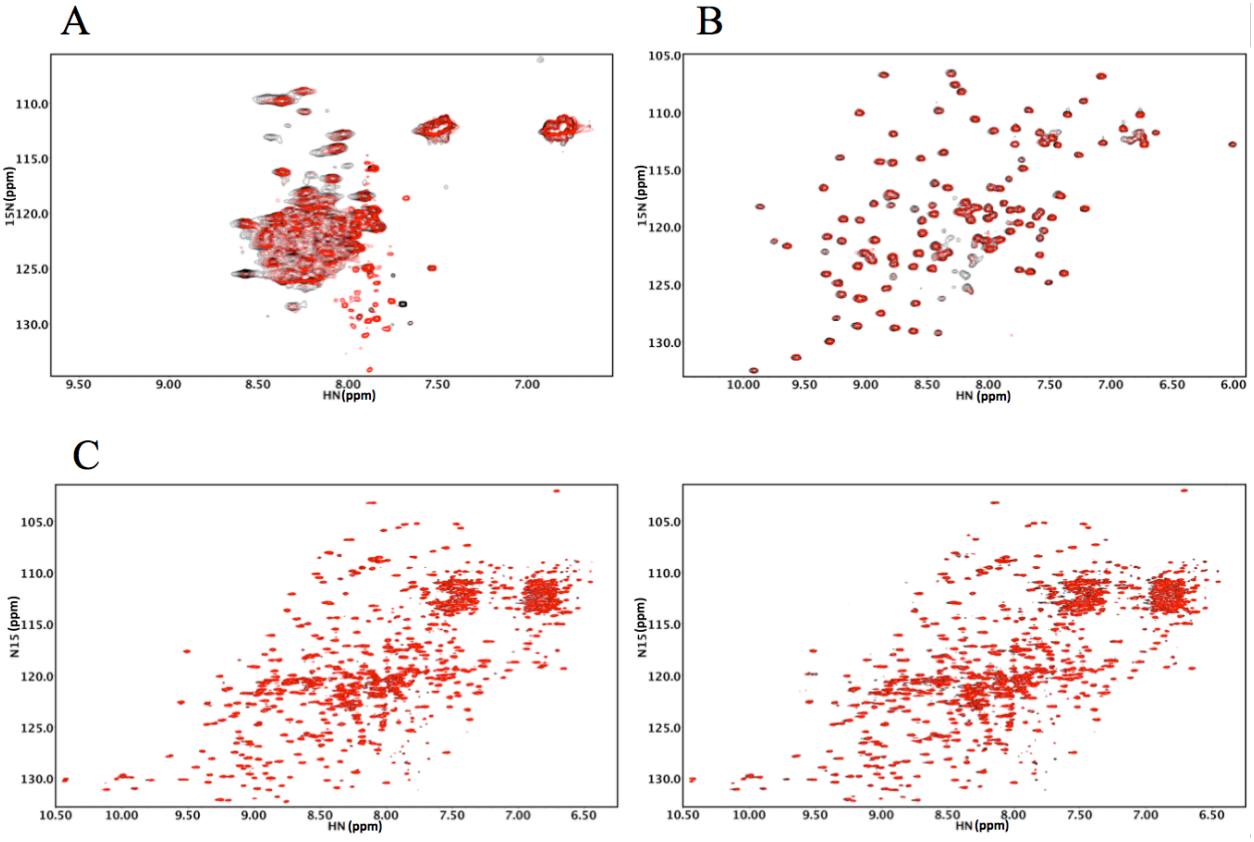

Figure 4.17: Interaction of MBD1-6 with the A-domain of ATP7B analyzed by ^{1}H, ^{15}N NMR spectroscopy. Overlay of ^{15}N (A) G875R-A-domain and (B) wild type A-domain in the absence (*black*) and presence of MBD1-6 (*red*). (C) Overlay of ^{15}N MBD1-6 (black) with wild-type A-domain (*red*) in the absence (*left*) and presence (*right*) of Atox1-Cu.

4.7 Glutaredoxin1 preferentially interacts with MBD1 and MBD2

Human glutaredoxin1 (hGrx1) has been identified as another protein that interacts with and binds to the N-terminus of ATP7B in a copper-dependent manner (Singleton et al., 2010). The hGrx1 is a thiol oxidoreducatase that catalyzes the reduction of disulfide bonds. Glutathionylation blocks copper binding through the formation of disulfide bridges in the cysteine residues of the MBDs. The hGrx1 catalyzes reduction of the GSSG-MBD disulfides to sulfhydryls, which restores Cu(I) binding to the MBDs. Thus, glutathione and glutaredoxin can regulate ATP7B activity through reversible modification of the cysteines in the copper-binding CxxC motif. To confirm whether hGrx1 and the MBDs interact, we used ^{1}H-^{15}N NMR spectroscopy to test the interaction.

Glutathione is present in millimolar concentrations in the cell, which may affect the binding of redox sensitive proteins to the metal-binding domains. In the presence of 10 mM GSH, we added unlabeled hGrx1 at a 6:1 molar ratio to ^{15}N MBD1-6, which ensured that all the MBDs could equally interact with hGrx1. Using chemical shift perturbation analysis, we mapped chemical shift changes, with the majority localized to MBD1 and MBD2 (Figure 4.18B).

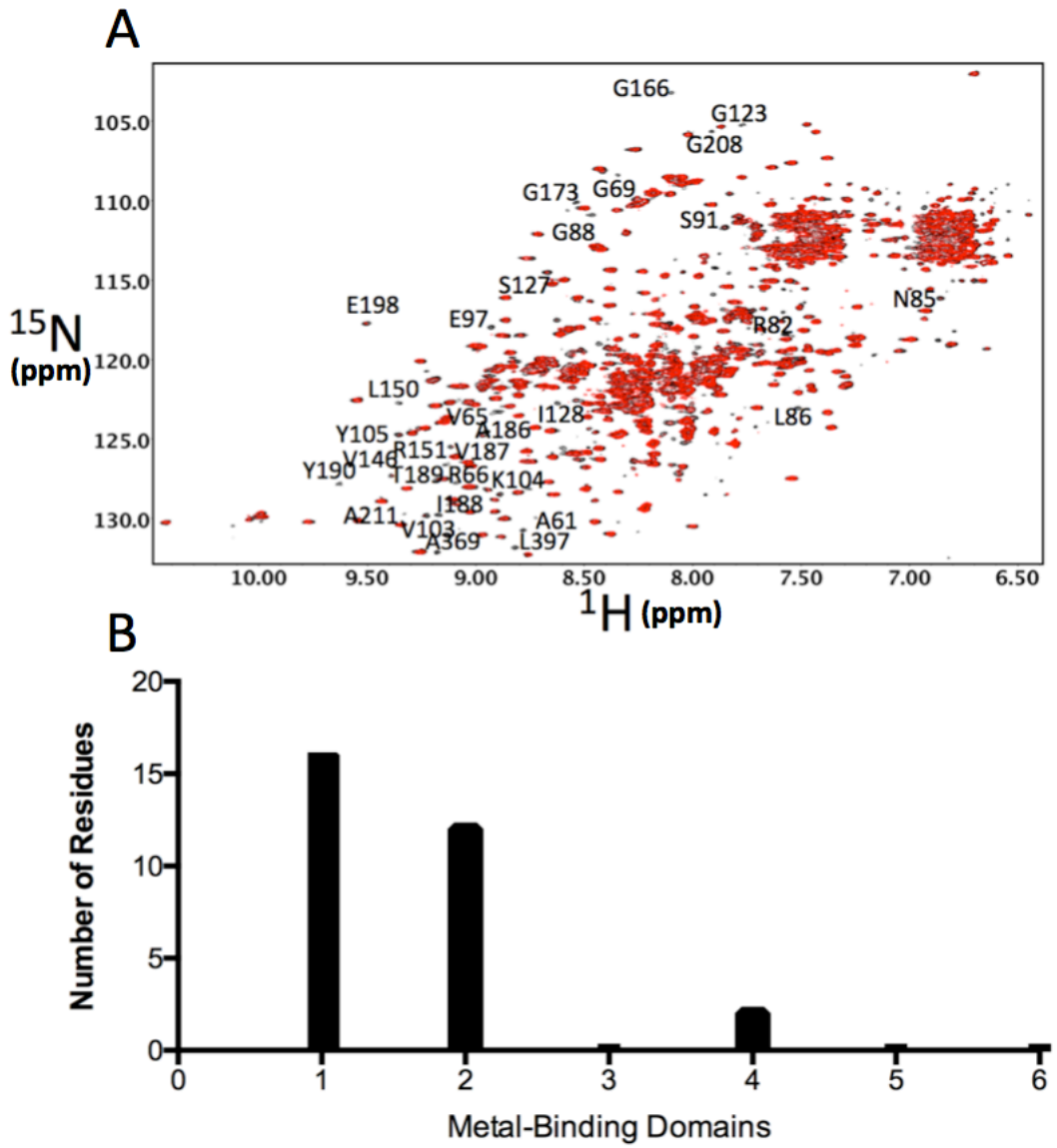

Figure 4.18: Interaction of MBD1-6 with hGrx1 analyzed by ^{1}H, ^{15}N-HSQC spectroscopy. (A) Overlay of ^{15}N MBD1-6 spectra in the absence (black) and presence (red) of hGrx1. (B) The distribution of residues in MBD1-6 that interact with hGrx1.

Interaction of hGrx1 with the first four individual MBDs was subsequently tested to determine the specific hGrx1-binding site. In the presence of 10 mM GSH, we titrated unlabeled hGrx1 up to a 2:1 molar ratio to the isotopically labeled individual MBDs. Interaction of the two proteins was monitored by chemical shift perturbation analysis. Our results show the following differences between the interaction of hGrx1 with MBD1 and MBD2. Significant chemical shift changes are observed when hGrx1 was added to MBD1 (Fig 4.19A), whereas a small amount of peak volume loss was observed when hGrx1 was added to MBD2 (Figure 4.19B). Interestingly,

no changes were observed when hGrx1 was added to either MBD3 or MBD4 (Figure 4.19CD). Despite the highly conserved CxxC copper binding motifs and sequence similarity of all of the MBDs, the interaction of hGrx1 appears to be preferential towards MBD1.

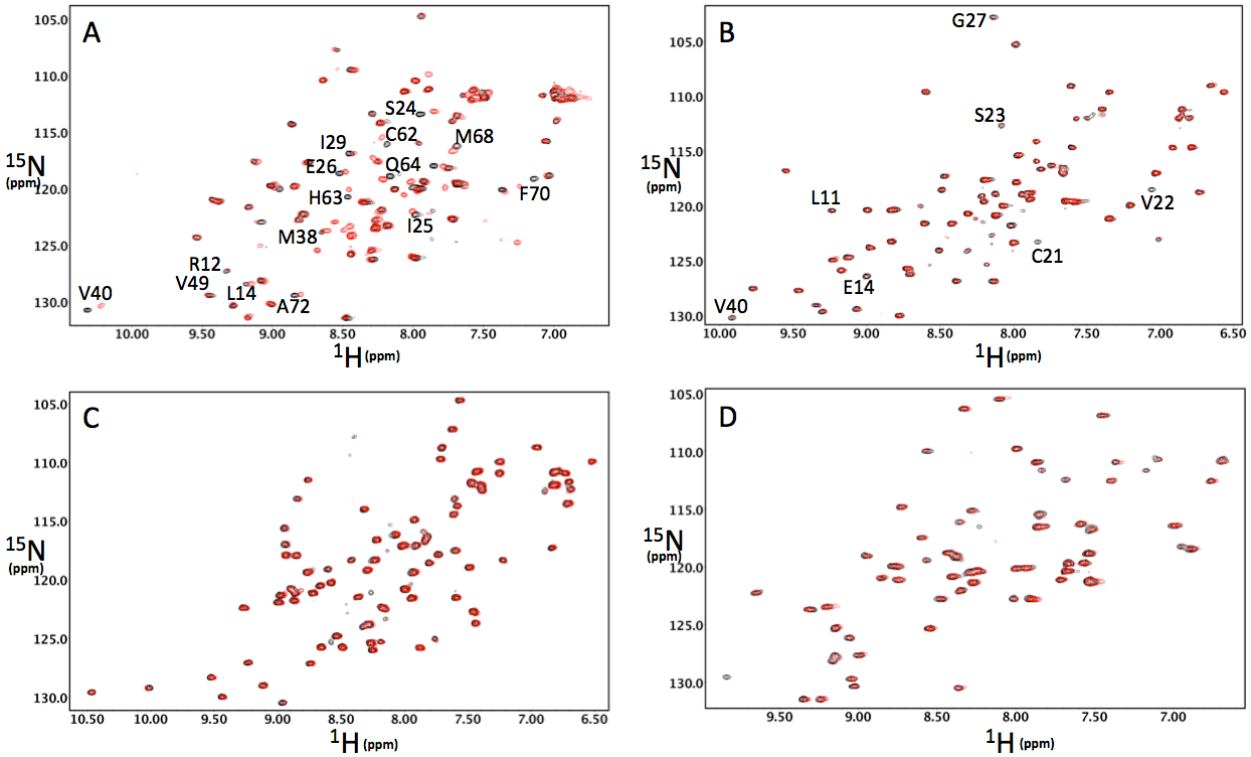

Figure 4.19: Interaction of individual MBDs with hGrx1 analyzed by ^{1}H, ^{15}N-HSQC spectroscopy. ^{1}H, ^{15}N-HSQC spectra overlay of (A) MBD1, (B) MBD2, (C) MBD3, and (D) MBD4 in the absence (*black*) and presence (*red*) of hGrx1.

4.8 Reaction of cisplatin with MBDs and platinum transfer between the copper-binding proteins and redox regulators.

4.8.1 Cisplatin and carboplatin bind to the CxxC motif of the metal-binding domains and form the same reaction product.

Overexpression of ATP7B has been implicated in cancer resistance to platinum-containing drugs. Using an *in vivo* bacterial assay, a previous study in our lab demonstrated that ATP7B confers cisplatin resistance by trapping cisplatin at the MBDs in the N-terminal region (Dolgova et al., 2009). The expression of a cytosolic fragment containing four metal-binding domains (MBD1-4) protected bacterial cells from the toxic effects of cisplatin. This demonstrates that cisplatin sequestration by the MBDs is an effective mechanism for causing cisplatin resistance (Dolgova et al., 2009). To characterize the molecular interactions of cisplatin with the MBDs, we analyzed the reactions of cisplatin and a related platinum analogue, carboplatin, with MBD2 using NMR chemical shift perturbation analysis.

MBD2 was chosen as the model system to examine the reactions of cisplatin and carboplatin because MBD2 is the preferential acceptor of copper from the chaperone protein Atox1 (Walker, 2004) and has been demonstrated to bind cisplatin (Dolgova et al., 2009). Therefore, we wanted to determine the cisplatin and carboplatin-binding site and analyze the structural effects of platinum drug binding to MBD2. The solution structure of metal-free MBD2 was solved, which allowed us map the cisplatin and carboplatin binding site (Dolgova et al., 2013). The cisplatin-binding site was mapped using NMR chemical shift perturbation analysis (Figure 4.20A). Cisplatin binding induced large chemical shift changes in the CxxC motif, as well as in regions distant from the copper-binding site (Figure 4.20D). To confirm the location of the cisplatin-binding site, we used an SxxS variant of MBD2, where the cysteines in the copper-binding motif were substituted with serine. As expected, no spectral changes were observed when cisplatin was added, confirming that cisplatin binds to the cysteine residues in the copper-binding motif (Figure 4.20B). A higher number of chemical shift changes caused by cisplatin is consistent with the larger size of the platinum-derivative compared to the copper ion, and may reflect an increased degree of conformational change required in the protein to accommodate platinum and its four ligands. Despite having different chemical structures,

cisplatin and carboplatin cause identical spectral changes (Figure 4.20C), which indicate that these drugs have the same binding mode. This suggests that ATP7B can confer resistance to both drugs through the same mechanism. Although the MBD2-Pt intermediate is the same for both cisplatin and carboplatin, the rates of reaction were significantly different. Complete cisplatin binding was observed within 4 hours, whereas complete binding of carboplatin was observed only after several days (Figure 4.21).

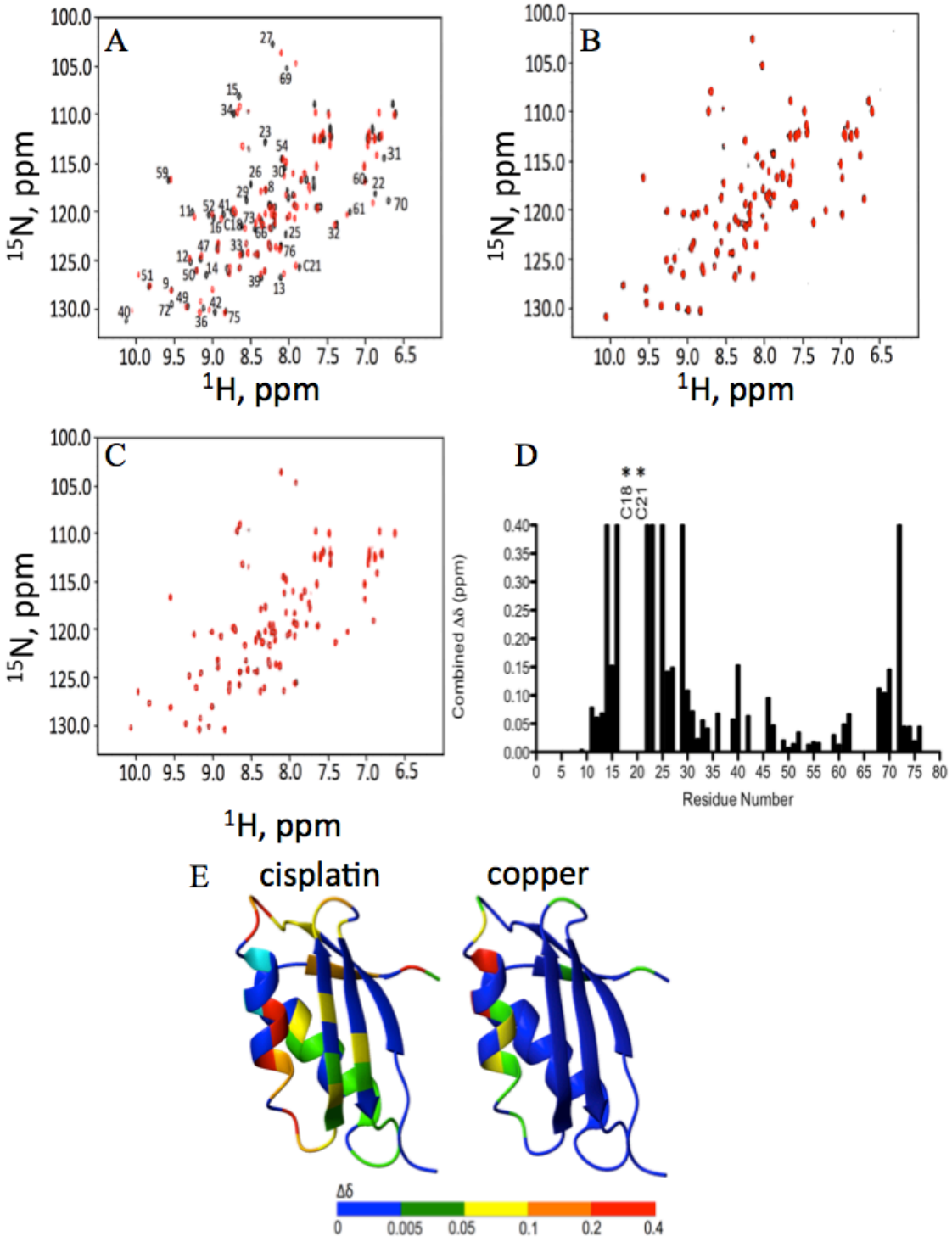

Figure 4.20: ^{1}H, ^{15}N-HSQC spectra of cisplatin binding to MBD2. (A) Overlay of apo- (black) and cisplatin-bound (red) wild-type MBD2 spectra; (B) Overlay of SxxS-MBD2 with (red) and without (black) cisplatin; (C) Overlay of MBD2 reacted with cisplatin (black) and carboplatin (red). (D) Chemical shift changes caused by cisplatin binding to MBD2 as a function of amino acid residue number. (E) Regions of MBD2 that are affected by cisplatin (left) and

copper (right) binding. Chemical shift assignment of C18 and C21 in the cisplatin-bound form was not found (*, cyan).

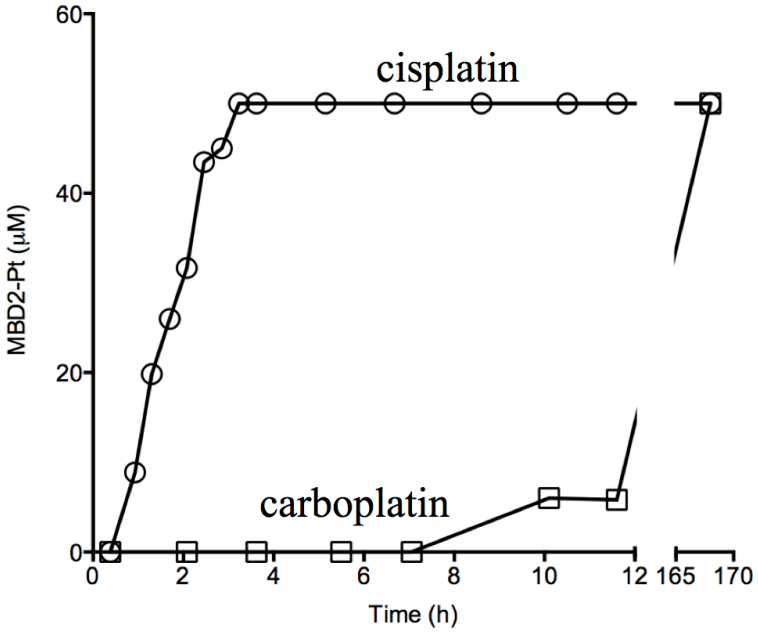

Figure 4.21: Time course of cisplatin and carboplatin reactions with MBD2.

4.8.2 Platinum is unidirectionally transferred from Atox1 to MBD2 and can bind to most of the metal-binding domains in MBD1-6.

Overexpression of ATP7B has been shown to be associated with tumor resistance to cisplatin during chemotherapy. In cells overexpressing ATP7B, its abundance is very low and pales in comparison to the concentration of glutathione and other cisplatin scavengers in the cell. How then does an increase in ATP7B expression detoxify cisplatin and cause resistance in cells? We propose that copper chaperone Atox1 binds cisplatin as it enters the cytoplasm and directly transfers the platinum derivative to the MBDs of ATP7B. To test this hypothesis, we measured platinum transfer from Atox1 to MBD2 using ^{1}H, ^{15}N NMR spectroscopy.

Platinum transfer from Atox1 to MBD2 was monitored by the chemical shift changes in both ^{15}N-labeled Atox1 and MBD2. The metal-free and platinum-bound forms of both Atox1 and MBD2 have distinct NMR spectra. This allowed us to simultaneously monitor the concentrations of both forms in the platinum transfer experiments. Initially, unlabeled Atox1 was pre-treated with cisplatin. The addition of ^{15}N-labeled MBD2 to unlabeled Atox1-Pt

produced chemical shift changes in ^{15}N MBD2 that were almost identical to those caused by free cisplatin (Figure 4.22A). This demonstrates that the reaction of MBD2 with free cisplatin and platinum transfer from Atox1 produced the same platinum adduct (Figure 4.22B). To monitor platinum release from Atox1, we repeated this experiment using ^{15}N-labeled Atox1-Pt and unlabeled MBD2. Following the treatment of ^{15}N Atox1 with cisplatin, we observed no residual *apo*-Atox1, confirming that complete cisplatin binding occurred (Figure 4.22C). After the addition of unlabeled MBD2, all of the peaks in the Atox1 spectrum returned back to the positions corresponding to the apo form, demonstrating that cisplatin was completely transferred to MBD2 and the metal-free, properly folded Atox1 was regenerated. However, some peaks near the copper-binding motif of Atox1 showed loss of intensity, which may reflect conformational or chemical exchange (Figure 4.22D). Interestingly, transfer of platinum was unidirectional. No transfer of platinum from ^{15}N MBD2-Pt to unlabeled Atox1 was observed (Figure 4.22EF).

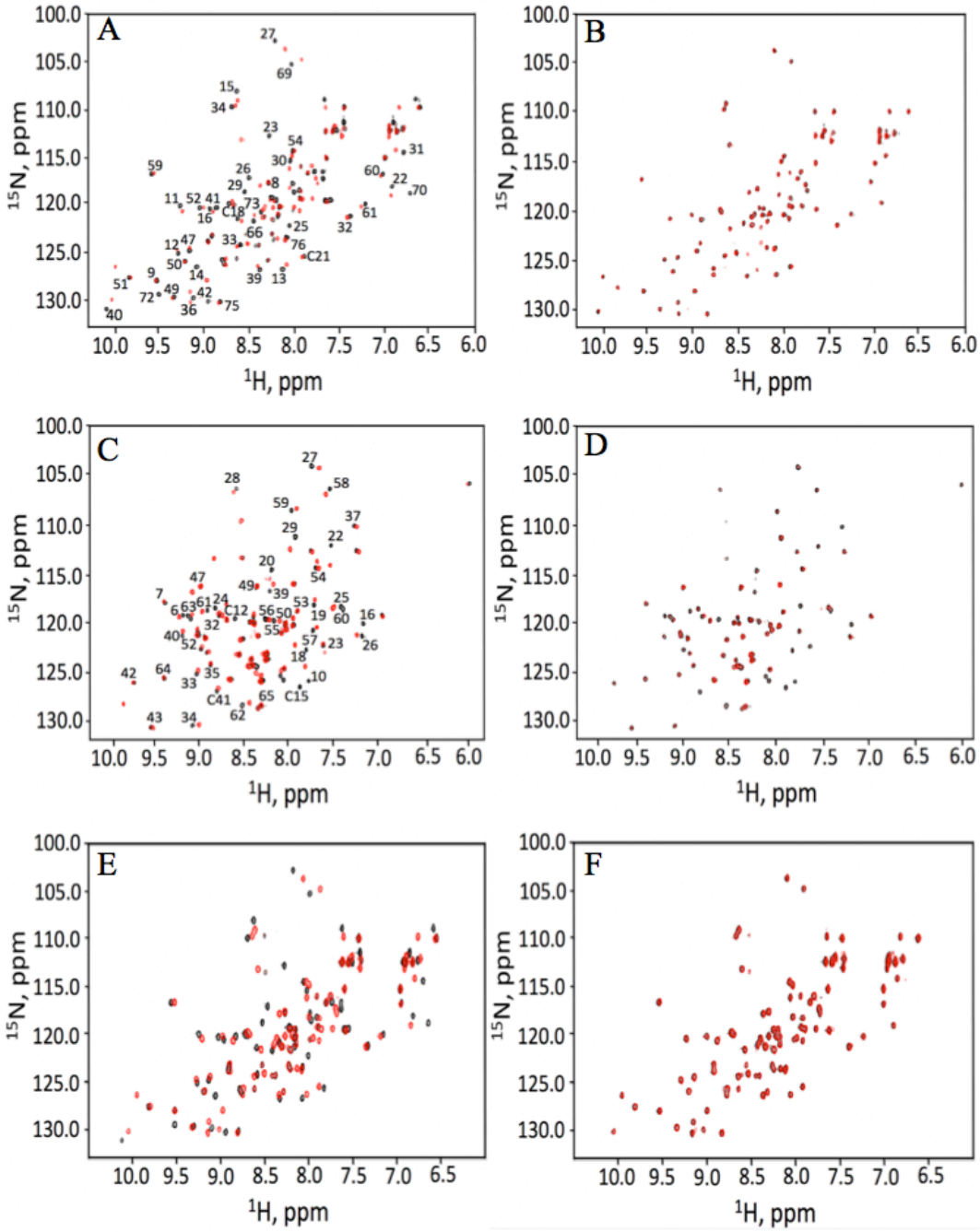

Figure 4.22: Transfer of platinum from Atox1 to MBD2 analyzed by ^{1}H, ^{15}N-HSQC spectroscopy. (A) Overlay of MBD2 before (black) and after (red) incubation of Atox1-cisplatin complex; (B) Overlay of MBD2 incubated with free cisplatin (black) and Atox1-cisplatin (red); (C) Overlay of Atox1 before (black) and after (red) incubation with cisplatin; (D) Overlay of Atox1 before incubation of cisplatin (black) and after (red) addition of unlabeled MBD2 to cisplatin-loaded Atox1; (E) Overlay of MBD2 before (black) and after (red) incubation with cisplatin at a 1:1 molar ratio; (F) Overlay of MBD2 incubated with free cisplatin before (black) and after (red) addition of unlabeled Atox1 at a 2:1 molar ratio.

4.8.3 Glutathione and glutaredoxin1 can serve as platinum acceptors from the metal-binding domains.

We have previously demonstrated that Atox1 directly transfers cisplatin to the MBDs (section 4.9.2). The MBDs may act as a reservoir by trapping cisplatin in the CxxC motif. However, it was unknown whether the MBDs were the final destination for cisplatin. Rather, cisplatin could be transferred on to other terminal acceptors in the cell. To test this hypothesis, we performed platinum transfer experiments from MBD2 to glutathione, glutaredoxin1, and thioredoxin1. These molecules contain cysteine residues in the active site that may remove platinum from MBD2 via the ligand-exchange mechanism. MBD2 was pre-treated with cisplatin. GSH, glutaredoxin1 (hGrx1), or thioredoxin1 (hTrx1) was subsequently added to the MBD2-Pt complex and the reaction was monitored by NMR spectroscopy. We observed a gradual return of MBD2-Pt back to its apo form in the presence of 5 mM GSH (Figure 4.23), demonstrating that GSH can indeed act as a terminal acceptor and extract platinum bound to the MBDs. Although the rate of platinum removal from the MBDs was slow, MBD2 completely returned to its apo form. The observed rate of MBD2-Pt reaction with glutathione appears to be too slow to account for cisplatin detoxification in the cell, which prompted us to investigate other potential acceptors such as thioredoxin1 or glutaredoxin1. These acceptors have a CxxC motif, which may extract platinum from the MBDs and contribute to efficient cisplatin detoxification. The rate of platinum transfer from MBD2-Pt to hTrx1 or hGrx1 was monitored by ^{1}H, ^{15}N-HSQC spectroscopy.

Chemical shift perturbation analysis was used to determine the rate of platinum transfer from MBD2 to hGrx1 or hTrx1. MBD2 was preloaded with cisplatin at an equimolar ratio. After addition of hGrx1 to MBD2-Pt at an equimolar ratio, we observed a slow rate of platinum release to hGrx1 in the first 12 hours, followed by a much faster rate of platinum release between 18 and 60 hours. This demonstrates that hGrx1 can be a potential acceptor of platinum from the MBDs. In contrast, platinum remains completely bound to MBD2 in the presence of hTrx1 (Figure 4.23). The lack of platinum transfer to hTrx1 suggests that platinum release from MBD2 is not indiscriminate.

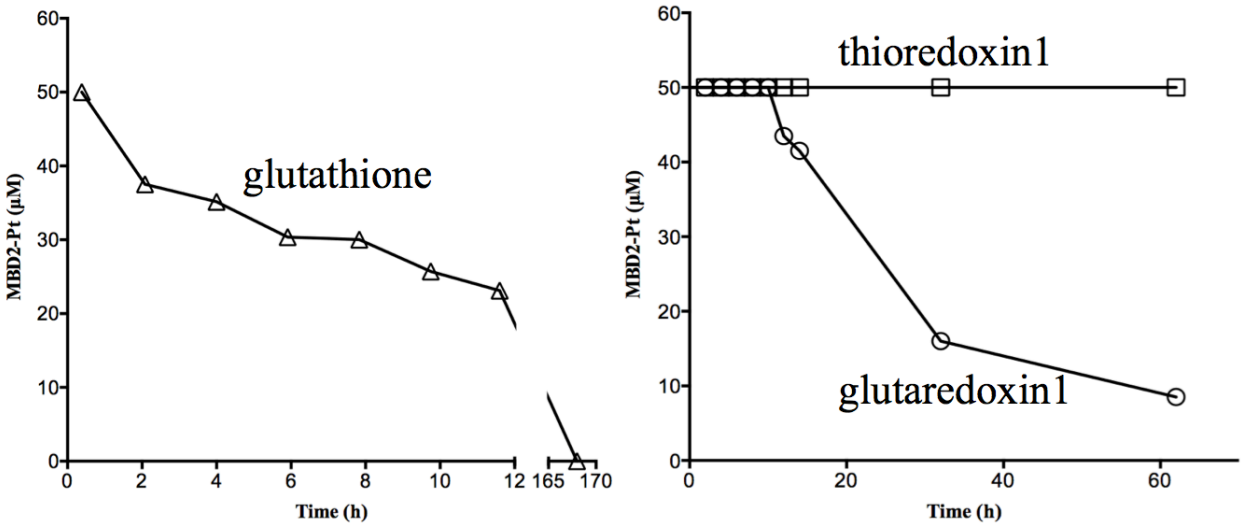

Figure 4.23: Time course for the return of the MBD2-cisplatin adduct in the presence of glutathione, glutaredoxin1, and thioredoxin1.

5 Discussion

5.1 Transient domain interactions within MBD1-3 and MBD5-6 groups.

The N-terminal region of ATP7B is composed of six metal-binding domains that function in the regulation of copper transport and trafficking activity. Except for MBD1, all the other individual metal-binding domain structures of ATP7B had been solved previously. Each MBD has a characteristic ferredoxin-like fold (βαββαβ) and binds one Cu(I) ion between two cysteine residues. The individual MBDs are compact structures that tumble as rigid bodies. However, to fully understand the conformation and dynamics of full-length MBD1-6, the structure of MBD1 was required.

We solved the structure of MBD1 using high-resolution NMR. Despite sharing only ~40-50% sequence similarity with the other MBDs of ATP7B and ATP7A, the structure of MBD1 has a ferredoxin-like fold (Figure 5.1). Similar to the other MBDs, copper binding to MBD1 affected the CxxC motif and adjacent residues. However, copper binding to MBD1 also affected the N-terminal region of α2, which was not observed in the other MBDs (Figure 5.1).

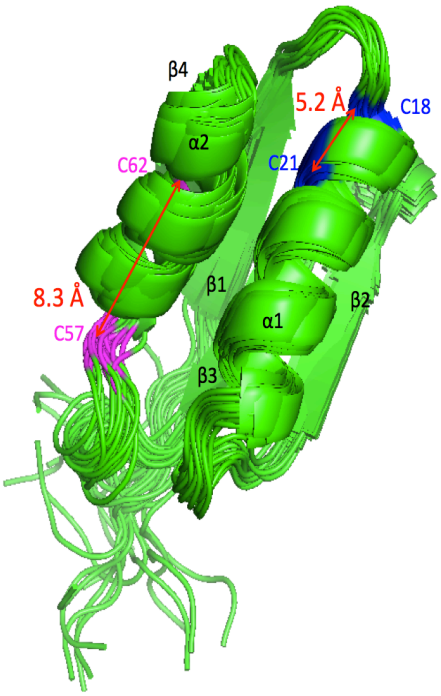

Figure 5.1: Structure of MBD1 showing the distances between the sulfur atoms in the CxxC copper-binding motif (blue) and the C^{57}xxxxC^{62} sequence (magenta).

Interestingly, there is a specific $C^{57}xxxxC^{62}$ sequence in the N-terminal region of α2 found only in MBD1. It is unlikely that the $C^{57}xxxxC^{62}$ sequence is another copper-binding site. The distance between the two sulfurs in the $C^{57}xxxxC^{62}$ sequence is 8.3 Å apart, which is 3.1 Å farther apart than the CxxC copper-binding motif (Figure 5.1). Additionally, complete binding of copper to MBD1 was observed at a 1:1 ratio. However, copper binding to the CxxC motif in the α1-helix may trigger conformational changes that affect the $C^{57}xxxxC^{62}$ region. Although the $C^{57}xxxxC^{62}$ sequence is not near the copper-binding motif, the C-terminus of a2-helix is significantly closer to the copper-binding motif compared to the other MBDs of ATP7B and MBD1 of ATP7A (MNK1) (Figure 5.2). At the nearest point of contact, the two alpha helices of MBD1 are at least 2 Å closer than the other MBDs, indicating that copper-binding to the α1-helix may trigger conformational changes in the α2-helix. We also observed that MBD1 aggregates significantly faster than all of the other purified MBDs and Atox1. This may suggest that the $C^{57}xxxxC^{62}$ sequence of MBD1 plays a role in inter-domain interactions with the other MBDs or cytosolic domains. This supports a previous hypothesis that hydrogen bond formation between the cysteine residues is required to maintain a tight conformation of MBD1-6 (LeShane et al., 2010).

NMR structural studies of the metal-binding domains show large conformational mobility. NMR relaxation measurements using shorter MBD constructs demonstrate independent dynamics and flexibility between the individual domains (Banci et al., 2008; Fatemi et al., 2010). The individual MBDs of MBD4-6 tumble at different rates, suggesting that the MBDs maintain a high degree of flexibility (Fatemi et al., 2010). In contrast, another study suggests that MBD5-6 tumbles as a rigid dumbbell in solution (Achila et al., 2006). The presence of additional MBDs may influence the behavior of shorter MBD constructs, which prompted us to investigate the dynamics of full-length MBD1-6. The narrow linewidths in the ^{1}H, ^{15}N-TROSY spectrum of MBD1-6 are consistent with rapidly tumbling independent MBDs, suggesting a "beads-on-a-string" model (Banci et al., 2009a; Fatemi et al., 2010). Inter-domain flexibility may allow the N-terminal region to interact with other cytosolic domains and facilitate copper transfer to MBD5, MBD6, and the transmembrane copper-binding sites. However, the completely independent dynamics of MBD1-6 appears to be inconsistent with previous biochemical studies.

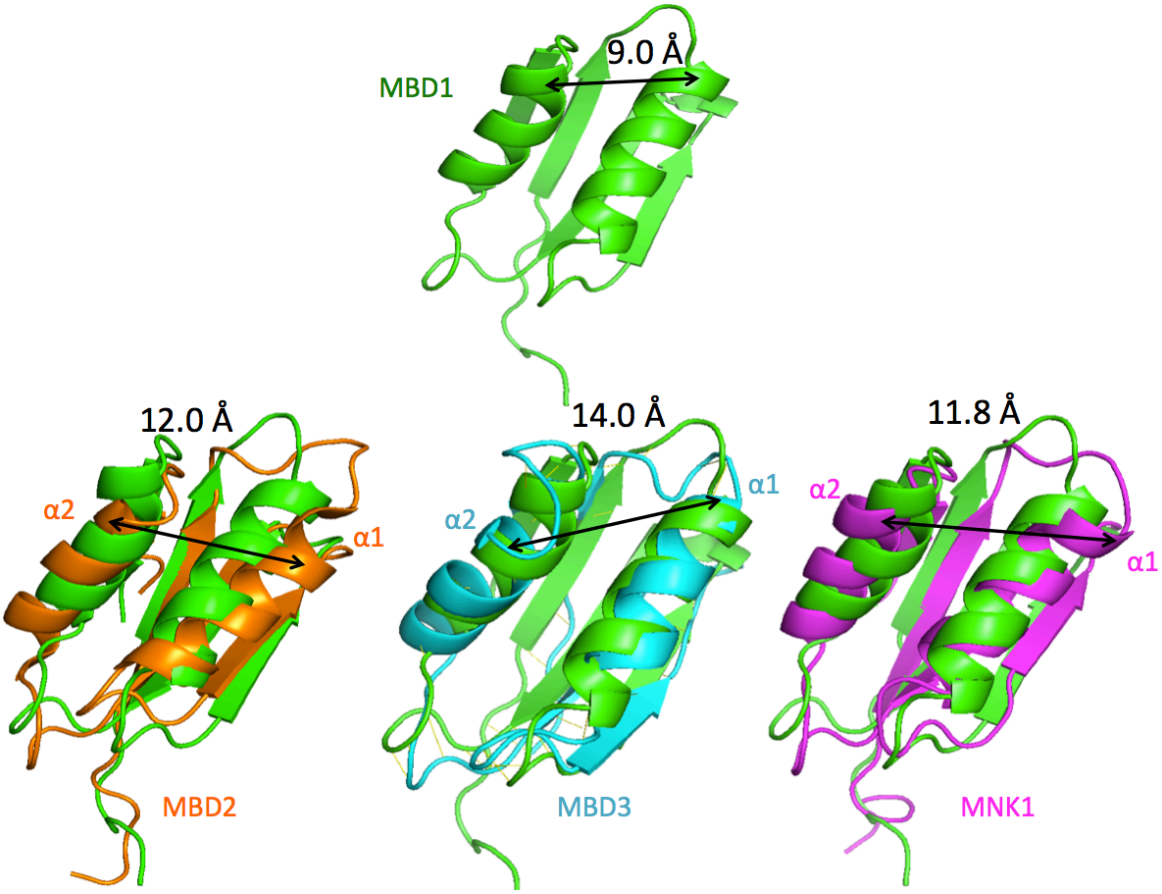

Figure 5.2: Structural comparison of MBD1 (green) with MBD2 (orange), MBD3 (cyan), and MNK1 (magenta). The distances shown are the nearest contact points between the copper-binding motif in α1 and the C-terminal region of α2.

Biochemical studies demonstrated copper-dependent conformational changes in MBD1-6. Cysteine to alanine mutations in the copper-binding motif of MBD2 and MBD3 caused oxidation in other MBDs, resulting in the total loss of copper binding (LeShane et al., 2010). Inter-domain hydrogen bonding at the cysteine residues was hypothesized to keep a tight conformation of MBD1-6. Investigating domain-domain interactions is particularly challenging because the individual MBDs are highly mobile, as indicated by the narrow linewidths in the ^{1}H, ^{15}N-TROSY spectrum of MBD1-6. To investigate the domain-domain interactions observed in the N-terminal region of ATP7B, we used nanobodies as a tool to probe the backbone dynamics and transient interactions of the individual MBDs in full-length MBD1-6.

Nanobodies are isolated single variable domains of heavy-chain antibodies. The nanobodies that were produced are highly soluble, monomeric proteins that specifically bind to

MBD1-6. The small size of the nanobodies is particularly advantageous in NMR transverse relaxation studies because the binding of a nanobody to a specific domain does not decrease the quality of the MBD1-6 ^{1}H-^{15}N TROSY spectra. The rationale for using nanobodies in our analysis is that binding of a nanobody to a specific MBD may change the dynamic properties for a specific group of MBDs. A change in the mobility of specific MBDs is reflected in the transverse relaxation rate. Our work reveals important structural and dynamic interactions that may explain the regulation of ATP7B copper transport and trafficking activity (Huang et al., 2014). Contrary to previous studies (Fatemi et al, 2010; Banci et al., 2009a), our NMR relaxation experiments demonstrated that MBD1-6 does not resemble a complete "beads-on-a-string" model. Rather, MBD1-3 is a correlated group of interacting MBDs with distinct dynamic characteristics compared to the other metal-binding domains. Binding of the R50 nanobody to MBD3 decreased the mobility of that specific domain, which is consistent with an increased molecular mass of the complex. Interestingly, the mobility of MBD1 and MBD2 significantly increased. This suggests that R50 nanobody binding

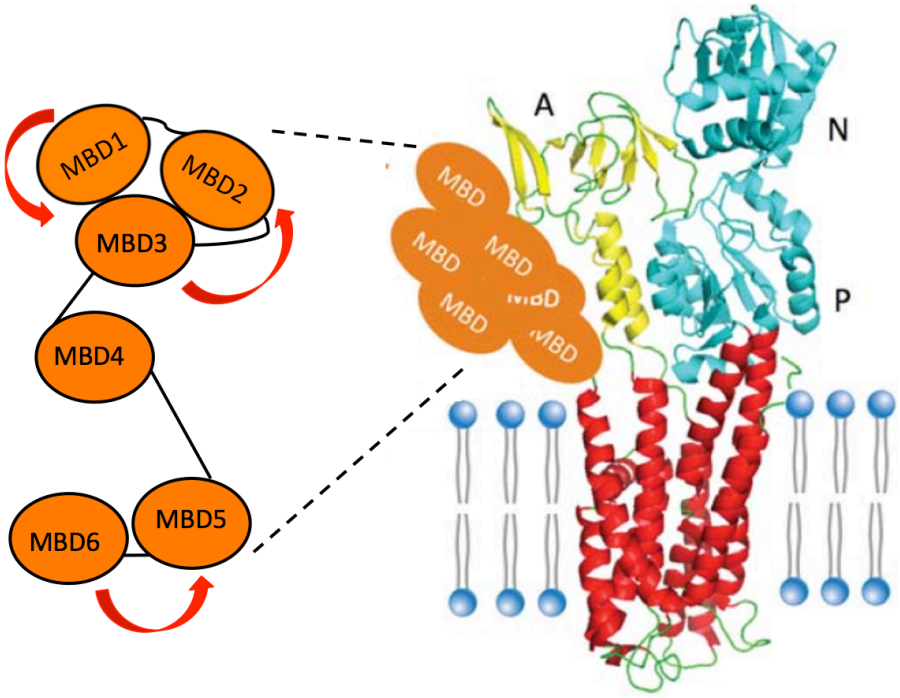

Figure 5.3: Model of the metal-binding domain interactions in the N-terminal region of ATP7B. Nanobodies have identified transient interactions (*red arrows*) between two groups of metal-binding domains, MBD1-3 (*in this work*) and MBD5-6 (*previously*). The dynamics of MBD4 is largely independent.

to MBD3 disrupts the transient interactions between MBD1-3, which cause increased dynamic independence of MBD1 and MBD2. R50 binding did not change the correlation times of MBD5 and MBD6. This is consistent with previous studies suggesting that MBD5-6 forms a separate structural unit (Achila et al., 2006). In contrast, when the 1R1 nanobody was bound to MBD4, the mobility of all the domains decreased to a similar extent. This suggests that the slower tumbling of the 1R1 nanobody-MBD4 complex is partially propagated to the other MBDs. The lack of distinct mobility changes in the MBDs suggests that the dynamics of MBD4 is highly independent and does not interact with other MBDs. MBD4 of rats cannot bind copper because it does not have the signature CxxC copper-binding motif, suggesting that MBD4 does not have an essential role in copper transfer. MBD4 may exclusively function as a structural link between two groups of correlated domains, MBD1-3 and MBD5-6.

To completely investigate the dynamics of the N-terminal region, we characterized a panel of 14 additional nanobodies that bind to the MBDs. We mapped all the nanobody-binding sites by chemical shift perturbation analysis and estimated the nanobody-binding affinities from the chemical exchange regime of the MBD-nanobody complexes. All the nanobodies tested bind to either MBD3 or MBD4, which suggests that these MBDs are more exposed in full-length MBD1-6, leading to higher immunogenicity of these domains. Nanobodies against MBD3 bind tightly and specifically to the C-terminal region of the α1 helix (Huang et al., 2014), suggesting that the folding of MBD1-3 exposes a single well-defined epitope. In contrast to MBD3, there is a wide range of binding epitopes and affinities for nanobodies that are produced against MBD4. This variability is consistent with independent dynamics of MBD4, resulting in higher surface exposure in full-length MBD1-6.

To obtain a more detailed model of MBD1-6 conformation and dynamics, we can investigate other transient interactions using nanobodies that bind to other MBDs. Although we only tested nanobodies against MBD3 or MBD4, phage display is a powerful technique for selecting nanobodies that bind to the other MBDs. Using the original cDNA library containing 4 x 10^8 independent clones that specifically bind to MBD1-6, we can select for nanobodies against a desired MBD. For example, to select for nanobodies against MBD1, we purify MBD1 and use that domain as an antigen for new rounds of positive selection by phage display. Since

nanobodies against MBD4 appear to be prevalent in the library, MBD4 can be used for negative selection. Our studies demonstrate that nanobodies are an effective tool for probing the conformation and dynamics of multi-domain proteins.

5.2 Regulation of ATP7B activity through domain-domain interactions.

The N-terminal region of ATP7B functions in the regulation of copper transport and trafficking activity. However, the precise molecular mechanism for regulating ATP7B activity by the N-terminal region is not well characterized. All the metal-binding domains have similar structures, but different groups of metal-binding domains have distinct functions. Only MBD5 and MBD6, the metal-binding domains closest to the transmembrane region, are essential for copper transport and trafficking activity (Cater et al., 2004; Huster, 2003). MBD1-4 was proposed to regulate ATP7B activity by controlling copper access to functionally important metal-binding sites (Huster, 2003).

All of the individual MBDs have similar structural folds and copper-binding properties. Each MBD binds one Cu(I) ion between two cysteine residues in a linear distorted geometry (DiDonato et al., 2000; Ralle et al., 2004). Although absolute values of copper-binding affinity to each MBD depend on the method used, the relative affinities of all the MBDs were found to be similar in each study (Banci et al., 2010; Wernimont, 2003; Yatsunyk and Rosenzweig, 2007). Since there is no specific MBD with a significantly higher copper-binding affinity, the mechanism of copper transfer to functionally important metal-binding sites such as MBD5 and MBD6 is not clear. One mechanism may involve inter-domain copper transfer. Docking of Atox1-Cu to MBD2 may trigger conformational changes in the N-terminal region, allowing upstream copper acceptor sites to transfer copper to MBDs 5 and 6 (Achila et al., 2006). Recognition of the partner protein in the copper transfer reaction may be mediated through electrostatic interactions. An alternative mechanism may involve the direct transfer of copper from Atox1 to all of the MBDs (Banci et al., 2009a; LeShane et al., 2010; Yatsunyk and Rosenzweig, 2007). However, we cannot exclude the possibility that Atox1 can directly transfer copper to the transmembrane binding site. The bacterial copper chaperone, CopZ, activates the enzymatic activity of the *Archaeoglobus fulgidus* Cu^{+}-ATPase, CopA, by directly transferring copper to the transmembrane binding sites (González-Guerrero and Argüello, 2008).

We previously demonstrated that transient interactions exist between MBD1-3 and are disrupted by nanobody binding. Our results demonstrate that copper binding to MBD1-6 indeed disrupts transient interactions between MBD1-3 in a similar mechanism as R50 nanobody binding to MBD3 (Figure 5.4). We observed a decrease in mobility in both MBD2 and MBD1 when apo-Atox1 is added to MBD1-6. This result is consistent with previous studies demonstrating that MBD2 preferentially interacts with Atox1 (Walker, 2004). Since there is a short linker of 13 amino acids between MBD1 and MBD2, the slower tumbling caused by the increased molecular weight of the Atox1-MBD2 complex may propagate to MBD1, thereby, decreasing the mobility of that domain. In contrast, the mobility of MBD1, MBD2, and MBD3 increase when copper is transferred from Atox1 to MBD1-6. The increased dynamic independence of MBD1-3 confirms our hypothesis that transient interactions exist between MBD1-3 and are disrupted when copper binds (Huang et al., 2014).

Taken together, our transverse relaxation data of MBD1-6 allow us to propose a model for the regulation of ATP7B copper transport and trafficking activity. Transient interactions restrict copper access to MBD1-3 (Figure 5.5A). Under copper limiting conditions, copper is transferred from Atox1 to MBD2, which is the preferred docking site for Atox1 (Walker, 2004). The transfer of copper to MBD2 disrupts the weak inter-domain interactions between MBD1-3, causing increased dynamic independence of MBD1 and MBD3 (Figure 5.5B). The increased dynamics of MBD1-3 changes the orientation of the connecting loops, which may increase copper accessibility to the other MBDs (Figure 5.5C). MBD5 and MBD6 may acquire copper directly from Atox1 (Figure 5.5D) or by inter-domain copper transfer from upstream acceptor sites such as MBD1-3 (Figure 5.5E).

An additional mechanism for regulating ATP7B activity involves the interaction of the MBDs with the other cytosolic domains. It has been demonstrated that the N-terminal region of ATP7B interacts with the ATP-BD (Tsivkovskii et al., 2000). The authors proposed that the MBDs hold ATP-BD in a specific conformation (Tsivkovskii et al., 2000). Copper binding releases the MBDs from ATP-BD. ATP-BD subsequently adopts a conformation with a high ATP binding-affinity (Tsivkovskii et al, 2000). This is in agreement with our model demonstrating that copper binding disrupts inter-domain interactions between MBD1-3. After

Cu(I) binds to MBD2, conformational changes in MBD1-3 triggers the release of MBD1-6 from ATP-BD.

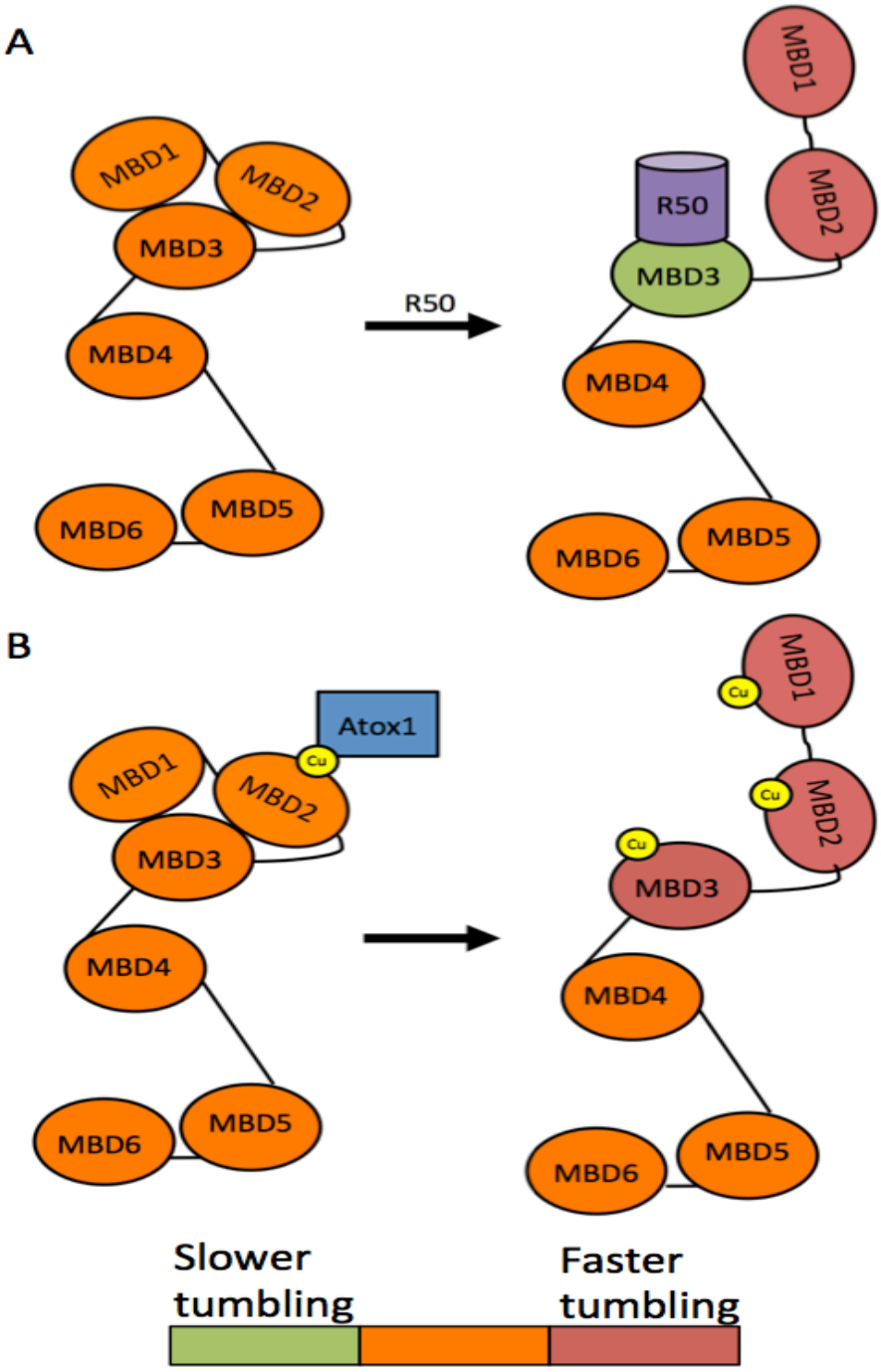

Figure 5.4: The effect of (A) R50 nanobody and (B) copper-binding on the domain dynamics of MBD1-6.

Additionally, a previous study suggested that the metal-binding domains interact with the G875R A-domain in a copper-dependent manner (Gupta et al., 2011). The G875R A-domain is unfolded, resulting in mislocalization of ATP7B to the endoplasmic reticulum. The MBDs were hypothesized to provide extra rigidity to the G875R A-domain. However, we did not observe any interaction between the N-terminal region and the A-domain. In the N-terminal region of ATP7B, there is a 63 amino acid sequence that is upstream from the first metal-binding domain (Guo, 2005). This 63 amino acid sequence is responsible for correctly targeting ATP7B to the apical membrane in polarized cells (Guo, 2005). It could be hypothesized that the N-terminal 63 amino acid residues actually interact with the other cytosolic domains and not the specific metal-binding domains.

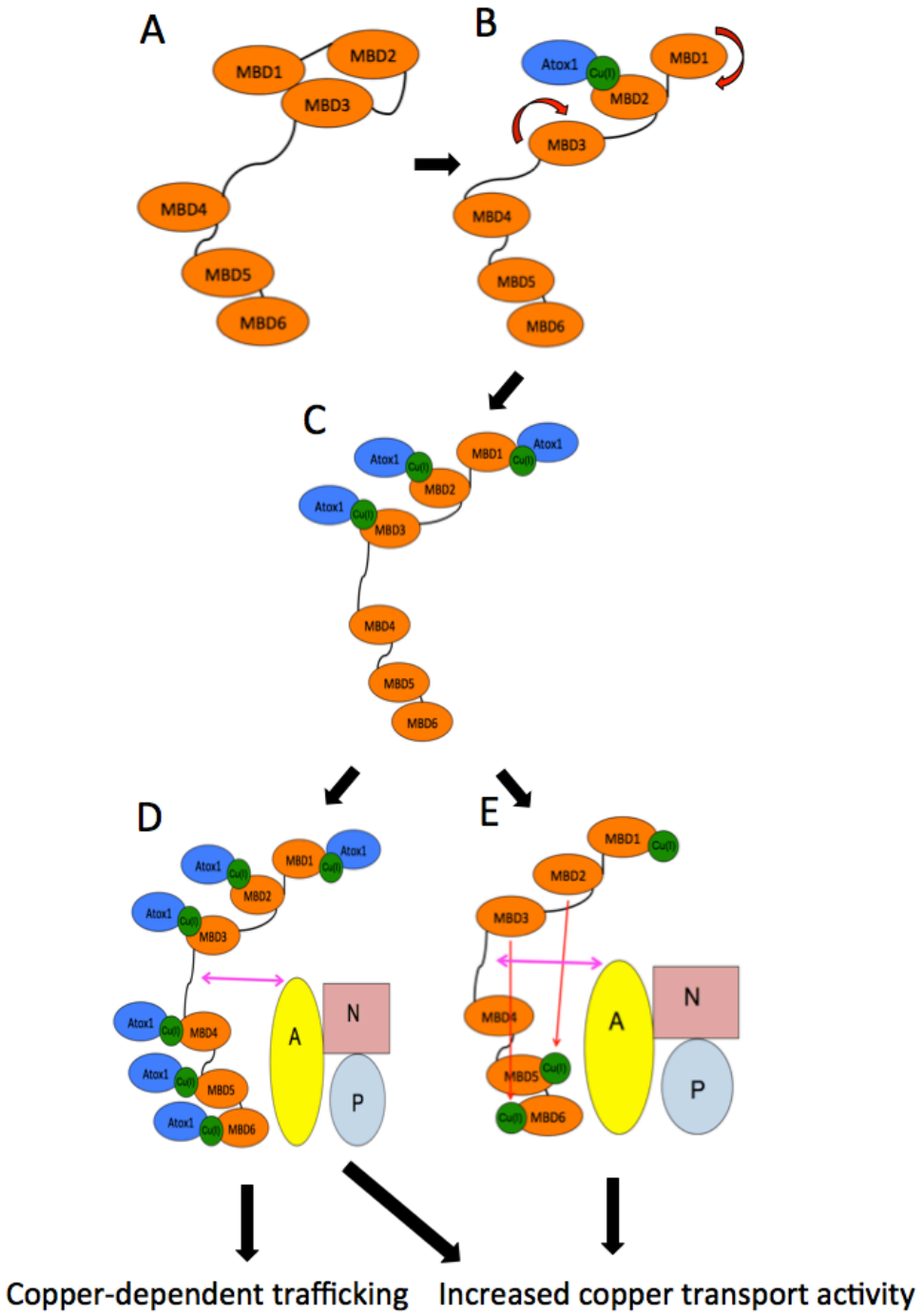

Figure 5.5: The proposed mechanism for the regulation of ATP7B activity. (A) Transient interactions restrict copper access to MBD1-3. (B) Atox1 transfers Cu(I) to MBD2 and disrupts the transient interactions, causing increased mobility of MBD1 and MBD3 (*red arrows*). (C) Other MBDs become more accessible for Cu(I) binding. A copper saturated state occurs by either (D) direct transfer of copper from Atox1 or (E) inter-domain copper transfer from MBD1-3. This conformation maintains the electrostatic repulsion between the MBDs and the other cytosolic domains (*pink arrow*), which increases copper transport activity and triggers copper-dependent trafficking of ATP7B.

5.3 Platinum and copper interact with the metal-binding domains of ATP7B via the same mechanism.

Cisplatin is a widely used anti-cancer drug; however, intrinsic and acquired resistance limit its effectiveness. Several copper transport proteins can bind cisplatin and are implicated in a variety of cisplatin resistance mechanisms. The copper transporter hCtr1 has been shown to mediate the uptake of cisplatin (Ishida et al., 2002). Atox1 is a copper chaperone that binds cisplatin both *in vitro* (Palm et al., 2011) and *in vivo* (Arnesano et al., 2011) at the signature CxxC motifs. Lastly, overexpression of ATP7B is associated with tumor resistance to cisplatin during chemotherapy. Our lab previously demonstrated that the metal-binding domains efficiently detoxified cisplatin without actively transporting it out of the cell (Dolgova et al., 2009). However, it was unclear how cisplatin actually reached the metal-binding domains of ATP7B. We propose that cisplatin utilizes the copper transport pathway by hijacking the Atox1-ATP7B copper transport route. This may allow Atox1 to directly deliver cisplatin to the MBDs of ATP7B. To test this hypothesis, we measured cisplatin transfer from Atox1 to MBD2. Since Atox1 specifically delivers copper to MBD2 (Walker, 2004), this domain was chosen as a small model system to examine the interactions with cisplatin.

It was previously reported that cisplatin-induced Atox1 unfolding may be a possible cisplatin resistance mechanism (Palm et al., 2011). However, this study was performed with higher cisplatin to protein ratios. With the large number of molecular components in the cell that can bind cisplatin, it is unlikely that multiple cisplatin molecules can bind to one specific protein and induce homo-oligomerization. No protein unfolding during the course of the NMR experiments was observed in our experimental conditions.

We successfully demonstrated that Atox1 directly transferred cisplatin to MBD2. Unlike copper transfer between Atox1 and MBD2, which is reversible, cisplatin transfer to MBD2 was unidirectional. This suggests that the MBDs can serve as a kinetic trap by stabilizing the four ligands that are attached to platinum. This transfer mechanism may also be applicable for another platinum analog, carboplatin. We demonstrated that carboplatin formed the same platinum adduct with MBD2, suggesting that ATP7B can confer resistance to both drugs through the same mechanism.

To increase the effectiveness of cisplatin detoxification by the metal-binding domains of ATP7B, Atox1 may also transfer cisplatin to the other MBDs. This hypothesis was recently supported by a study demonstrating that Atox1 transferred cisplatin to MBD4 of ATP7B (Palm-Espling et al., 2013). However, contrary to our studies, a heterodimer was also formed between Atox1 and MBD4 during platinum transfer (Palm-Espling et al., 2013). Differences in incubation times for Atox1-Pt may explain the shift towards heterodimer formation in MBD4. It was suggested that increasing the incubation time between Atox1-Pt and MBD4 decreased the amount of platinum transferred between Atox1 and MBD4 (Palm-Espling, 2013). This observation is consistent with our results. Atox1-Pt was incubated with MBD2 for two hours in our experimental conditions, whereas the reported study incubated Atox1-Pt with MBD4 for twice as long.

Our study demonstrates that Atox1 binds and transfers cisplatin to the MBDs of ATP7B. However, it is well established that the main physiological function of Atox1 is to deliver copper to the MBDs. If both cisplatin and copper are present in the cell, how does Atox1 determine which metal to bind? A recent study demonstrated that monomeric Atox1 forms a di-metal complex by binding both copper and platinum simultaneously at the CxxC motif (Palm-Espling et al., 2013). This study also proposes that cisplatin may hitchhike with copper onto Atox1 instead of completely occupying the single metal-binding site. However, it is unknown which metal, if any, can be transferred from copper- and cisplatin-bound Atox1 to the metal-binding domains. Our studies demonstrate that cisplatin utilizes the copper transport pathway by binding to Atox1 for subsequent delivery to the MBDs of ATP7B.

5.4 Transfer of platinum along the copper transport pathway serves as a mechanism of cisplatin detoxification in the cell.

We have demonstrated that Atox1 binds and transfers cisplatin to the MBDs of ATP7B, in a process that parallels the copper transport pathway. Since ATP7B has several potential cisplatin binding sites, the transfer of platinum to the MBDs serves as an efficient mechanism for cisplatin detoxification. When cisplatin reaches ATP7B, two possible mechanisms have been proposed in the detoxification of cisplatin. One mechanism is the active transport of cisplatin out

of the cell catalyzed by ATP7B (Safaei et al., 2007; Tadini-Buoninsegni et al., 2013). The other mechanism involves cisplatin being trapped at the MBDs (Dolgova et al., 2013; 2009). Although ATP7B is known to transport copper across the cell membrane, cisplatin transport using the same mechanism is not an efficient process. Platinum transport was observed in Sf9 cells expressing functional ATP7B (Safaei et al., 2007). The maximal platinum transport rate was 30 pmol/mg protein/min measured at a non-physiological pH of 4.6. This rate was also pH dependent, as the cisplatin transport rate was almost negligible near physiological pH (Safaei et al., 2007).

The low cisplatin transport rate at physiological pH suggests that active extrusion may not be the primary mechanism for cisplatin detoxification. Rather, we propose that a more likely *in vivo* cisplatin resistance mechanism involving ATP7B is the sequestration of cisplatin at the metal-binding domains. Our lab previously demonstrated that a protein construct expressing the first four metal-binding domains (MBD1-4) was sufficient to confer cisplatin resistance in *E. coli* cells (Dolgova et al., 2009). Using a simple *in vivo* assay, platinum binding to DNA can be monitored by the formation of *E. coli* cell filaments. When MBD1-4 was expressed, cell filamentation was not observed, demonstrating that the MBDs can exert a protective effect against cisplatin. Since MBD1-4 is entirely cytosolic in the cell, cisplatin detoxification is likely mediated by platinum sequestration in the metal-binding domains and not active extrusion out of the *E. coli* cell.

The six metal-binding sites in ATP7B increase the total cisplatin binding capacity. However, the abundance of ATP7B is still low even in cells overexpressing ATP7B. How then does a limited number of approximately 500 ATP7B molecules per cell (Beck et al., 2011) detoxify cisplatin and cause resistance in cells? We propose that the metal-binding domains may not be the final destination for cisplatin. Rather, the MBDs serve as a high-affinity reservoir for cisplatin molecules that can transfer platinum to other abundant proteins or small molecule acceptors in a non-toxic form. To test this hypothesis, we measured platinum release from MBD2 to other potential terminal acceptors such as glutathione, glutaredoxin1, and thioredoxin1.

We observed a gradual return of cisplatin-bound MBD2 back to its apo form in the presence of GSH or human glutaredoxin. This demonstrates that GSH and hGrx1 can be potential acceptors by extracting platinum bound to the MBDs. Despite having a CxxC motif, hTrx1 cannot strip platinum off MBD2, suggesting that platinum transfer is not indiscriminate. Specific protein-protein interactions with an even higher cisplatin binding affinity than MBD2 may be required to strip platinum off the MBDs. The quantitative cisplatin-binding affinities for hGrx1 have not been determined; however, hGrx1 is a likely candidate as an intermediate acceptor in the cell because it has been shown to specifically interact with the MBDs at the CxxC motif (Singleton et al., 2010).

The ability for GSH to extract platinum from the MBDs is more complicated. GSH has the lowest copper binding affinity among the copper-binding proteins (Banci et al., 2010). If cisplatin transport follows the same copper binding affinity gradient, how can GSH strip platinum off the MBDs? A possible explanation may be that copper and platinum react differently upon binding to various cellular components. Copper(I) does not change chemically when it reacts with different proteins in the cell. Cu(I) remains bound by two ligands in a distorted linear geometry. In contrast, the ligands attached to platinum are substituted by different moieties depending on the protein it binds to. Therefore, the different combination of ligands that are bound to platinum may cause some of these reactions to be kinetically irreversible.

Taken together, our data allows us to propose a mechanism of cisplatin detoxification by ATP7B. We propose that there are two branches of cisplatin transport in the cell, both mediated through Atox1. One pathway leads to cisplatin detoxification through ATP7B (Figure 5.6A; *red arrow*). The other pathway involves cisplatin delivery to the nucleus, causing cell death (Figure 5.6A; *blue arrow*). Therefore, cell sensitivity to cisplatin is determined by the balance of cisplatin delivery to ATP7B or to the nucleus.

The direct transfer of platinum from Atox1 to the MBDs parallels copper distribution within cells and allows us to explain how moderate levels of ATP7B overexpression can lead to cisplatin resistance. Cisplatin enters the cell through the passive copper channel, hCtr1. Atox1

binds cisplatin at the entry site from the C-terminal region of hCtr1, which prevents cisplatin sequestration by glutathione and other low-affinity acceptors in the cytosol (Figure 5.6B; *black arrow*). Atox1 also functions as a copper-responsive transcription factor that can translocate into the nucleus and bind to DNA (Itoh et al., 2008; Muller and Klomp, 2009). This suggests that Atox1 may deliver cisplatin into the nucleus, causing various Pt-DNA crosslinks. Concurrently, a fraction of Atox1-Pt is also delivered to the MBDs of ATP7B. Platinum is then gradually released to other acceptors such as glutathione and glutaredoxin in a non-toxic form (Figure 5.6B; *red dashed arrow*). This mechanism may predominate at low cisplatin concentrations in the cell during chemotherapy. As ATP7B expression increases, so does the amount of cisplatin interacting with the MBDs, which decreases the potential amount of cisplatin reacting with DNA. This supports the correlation between increased ATP7A/ATP7B expression and cisplatin resistance (Figure 5.6B*; red arrow*). However, in our experimental work, much higher cisplatin concentrations were used. At higher cisplatin concentrations, the Atox1-Pt transport mechanism may become overwhelmed. This may cause excess platinum to indiscriminately bind to GSH, metallothionein, or other low-affinity acceptors.

Since the cisplatin and copper transport pathways are intertwined, it may be possible to reduce cisplatin detoxification by manipulating the copper status in the cell. Copper induces the downregulation of its own influx transporter, hCtr1 (Molloy and Kaplan, 2009). By decreasing the copper concentration in the cell, the amount of hCtr1 at the plasma membrane is maximized for cisplatin uptake. When cisplatin was used in combination with a copper chelator, tetrathiomolybdate, tumor cell sensitivity to cisplatin increased by two-fold (Ishida et al., 2010). Increased cisplatin uptake into the cell would allow Atox1 to bind and transfer more cisplatin to the nucleus. Therefore, combinational therapy with cisplatin and copper chelators may lead to safer and more effective platinum-based chemotherapy.

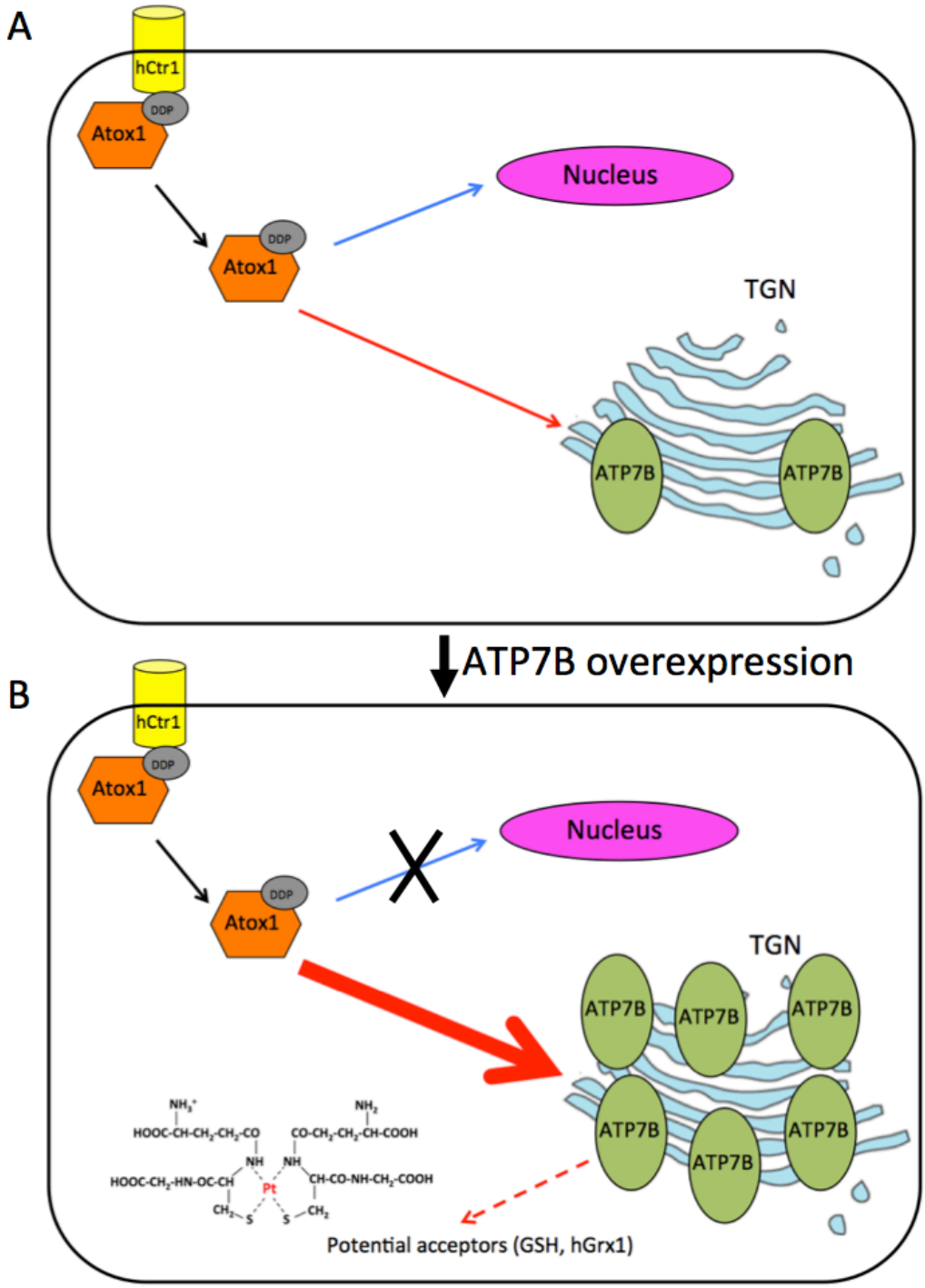

Figure 5.6: Cisplatin transfer from Atox1 to the MBDs leads to cisplatin detoxification. (A) Atox1 binds and transfers cisplatin to the nucleus (*blue arrow*) and a small fraction to the MBDs (*red arrow*). (B) As ATP7B is overexpressed, the fraction of cisplatin transferred to the MBDs also increases (*red arrow*). This reduces the amount of cisplatin reaching the nucleus (*blue arrow*), thereby, facilitating cisplatin resistance. Platinum or a platinum derivative can be subsequently transferred from the MBDs to other acceptors such as glutathione and glutaredoxin1 (*red dashed arrow*).

6 Conclusions

We have demonstrated that cisplatin can be transferred in the cell along the copper transport pathway by hijacking copper chaperone Atox1. We have shown that copper and platinum share the same mechanism of interaction with the metal-binding domains of ATP7B. We have also demonstrated that ATP7B can confer resistance to different platinum analogs through the same mechanism. We have proposed an effective mechanism of cisplatin detoxification in the cell mediated by ATP7B and have identified potential acceptors that can strip platinum off the MBDs.

We have solved the solution structure of MBD1, the only metal-binding domain whose structure was missing in ATP7B. We have demonstrated the potential of nanobodies as tools to study protein dynamics. This is a novel method that has helped us identify transient interactions between MBD1-3. The disruption of these transient interactions between MBD1-3 may be the key initial step for regulating ATP7B copper transport and trafficking activity. We have demonstrated copper dependent conformational transitions in MBD1-6 that led us to a structure-based model of ATP7B regulation by copper.

7 Future directions

In this work, we have identified two groups of dynamically correlated domains, MBD1-3 and MBD5-6, which are involved in the regulation of ATP7B copper transport and trafficking activity. Investigating how MBD1-3 is positioned in space relative to MBD5-6 may help us understand how these downstream metal-binding domains acquire copper. Residual dipolar couplings and paramagnetic relaxation enhancement are two NMR techniques that can be used to build a more precise model of MBD1-6 conformation and dynamics. Also, nanobodies that bind to other MBDs can be used to gain a complete picture of the transient interactions that exist within MBD1-6. Our studies have demonstrated that the disruption of transient interactions between MBD1-3 is the initial step for regulating ATP7B activity. However, it is unclear what the subsequent steps are in the mechanism of ATP7B copper transport. Does Atox1 directly transfer copper to MBD5, MBD6, or the transmembrane region? Is inter-domain copper transfer to MBD5-6 the predominant mechanism for activating ATP7B activity? We can test this hypothesis by examining whether Atox1-Cu can activate the copper transport activity of ATP7B

by selectively mutating cysteine residues in either MBD1-3 or MBD5-6.

To test our hypothesis that the Atox1-ATP7B copper transport pathway diverts platinum away from the nucleus, it is necessary to examine whether Atox1 can enter the nucleus and deliver cisplatin to DNA. The rate of platinum transfer from MBD2 to GSH or hGrx1 may be too slow to effectively detoxify cisplatin in the cell. We can investigate other potential acceptors that can remove platinum at a much faster rate from the MBDs.

8 References

Achila, D., Banci, L., Bertini, I., Bunce, J., Ciofi-Baffoni, S., and Huffman, D.L. (2006). Structure of human Wilson protein domains 5 and 6 and their interplay with domain 4 and the copper chaperone HAH1 in copper uptake. Proc. Natl. Acad. Sci. U.S.A. *103*, 5729–5734.

Albers, R.W. (1967). Biochemical aspects of active transport. Annu. Rev. Biochem. *36*, 727–756.

Anastassopoulou, I., Banci, L., Bertini, I., Cantini, F., Katsari, E., and Rosato, A. (2004). Solution structure of the apo and copper(I)-loaded human metallochaperone HAH1. Biochemistry *43*, 13046–13053.

Andersson, M., Mattle, D., Sitsel, O., Klymchuk, T., Nielsen, A.M., Møller, L.B., White, S.H., Nissen, P., and Gourdon, P. (2013). Copper-transporting P-type ATPases use a unique ion-release pathway. Nature *21*, 43–48.

Apell, H.J. (2004). How do P-type ATPases transport ions? Bioelectrochemistry *63*, 149-156.

Arnesano, F., Banci, L., Bertini, I., Felli, I.C., Losacco, M., and Natile, G. (2011). Probing the interaction of cisplatin with the human copper chaperone Atox1 by solution and in-cell NMR spectroscopy. J. Am. Chem. Soc. *133*, 18361–18369.

Banci, L., Bertini, I., Cantini, F., Massagni, C., Migliardi, M., and Rosato, A. (2009). An NMR study of the interaction of the N-terminal cytoplasmic tail of the Wilson disease protein with copper(I)-HAH1. J. Biol. Chem. *284*, 9354–9360.

Banci, L., Bertini, I., Cantini, F., Migliardi, M., Natile, G., Nushi, F., and Rosato, A. (2009). Solution structures of the actuator domain of ATP7A and ATP7B, the Menkes and Wilson disease proteins. Biochemistry *48*, 7849–7855.

Banci, L., Bertini, I., Cantini, F., Rosenzweig, A.C., and Yatsunyk, L.A. (2008). Metal binding domains 3 and 4 of the Wilson disease protein: solution structure and interaction with the copper(I) chaperone HAH1. Biochemistry *47*, 7423–7429.

Banci, L., Bertini, I., Ciofi-Baffoni, S., Kozyreva, T., Zovo, K., and Palumaa, P. (2010). Affinity gradients drive copper to cellular destinations. Nature *465*, 645–648.

Banci, L., Bertini, I., del Conte, R., D'Onofrio, M., and Rosato, A. (2004). Solution structure and backbone dynamics of the Cu(I) and apo forms of the second metal-binding domain of the Menkes protein ATP7A. Biochemistry *43*, 3396–3403.

Beck, M., Schmidt, A., Malmstroem, J., Claassen, M., Ori, A., Szymborska, A., Herzog, F., Rinner, O., Ellenberg, J., and Aebersold, R. (2011). The quantitative proteome of a human cell line. Mol. Syst. Biol. *7*, 1–8.

Bellacosa, A. (2001). Functional interactions and signaling properties of mammalian DNA mismatch repair proteins. Cell Death Differ. *8*, 1076–1092.

Bhattacharya, A., Tejero, R., and Montelione, G.T. (2006). Evaluating protein structures determined by structural genomics consortia. Proteins *66*, 778–795.

Binks, S.P., and Dobrota, M. (1990). Kinetics and mechanism of uptake of platinum-based pharmaceuticals by the rat small intestine. Biochem. Pharmacol. *40*, 1329–1336.

Boal, A.K., and Rosenzweig, A.C. (2009). Structural biology of copper trafficking. Chem. Rev. *109*, 4760–4779.

Boal, A.K., and Rosenzweig, A.C. (2009). Crystal structures of cisplatin bound to a human copper chaperone. J. Am. Chem. Soc. *131*, 14196–14197.

Braiterman, L., Nyasae, L., Guo, Y., Bustos, R., Lutsenko, S., and Hubbard, A. (2008). Apical targeting and Golgi retention signals reside within a 9-amino acid sequence in the copper-ATPase, ATP7B. Am. J. Physiol. *296*, G433–G444.

Braiterman, L., Nyasae, L., Leves, F., and Hubbard, A.L. (2011). Critical roles for the COOH terminus of the Cu-ATPase ATP7B in protein stability, trans-Golgi network retention, copper sensing, and retrograde trafficking. Am. J. Physiol. *301*, G69–G81.

Byerly, D., McElroy, C., and Foster, M. (2002). Mapping the surface of *Escherichia coli* peptide deformylase by NMR with organic solvents. Protein Sci. *11*, 1850-1853.

Cater, M.A., Forbes, J., La Fontaine, S., Cox, D.W., and Mercer, J.F.B. (2004). Intracellular trafficking of the human Wilson protein: the role of the six N-terminal metal-binding sites. Biochem. J. *380*, 805–813.

Cater, M.A., La Fontaine, S., Shield, K., Deal, Y., and Mercer, J.F.B. (2006). ATP7B mediates vesicular sequestration of copper: insight into biliary copper excretion. Gastroenterol. *130*, 493–506.

Chong, S., Mersha, F.B., Comb, D.G., Scott, M.E., and Landry, D. (1997). Single-column purification of free recombinant proteins using a self-cleavable affinity tag derived from a protein splicing element. Gene *192*, 271–281.

Cohen, G.L., Bauer, W.R., Barton, J.K., and Lippard, S.J. (1979). Binding of cis- and trans-dichlorodiammineplatinum(II) to DNA: evidence for unwinding and shortening of the double helix. Science *203*, 1014–1016.

Coste, F., Malinge, J.M., Serre, L., Shepard, W., Roth, M., Leng, M., and Zelwer, C. (1999). Crystal structure of a double-stranded DNA containing a cisplatin interstrand cross-link at 1.63 Å resolution: hydration at the platinated site. Nucleic Acids Res. *27*, 1837–1846.

Davies, J., and Riechmann, L. (1994). 'Camelising' human antibody fragments: NMR studies on VH domains. FEBS Lett. *339*, 285–290.

Dayie, K., Wagner, G., and Lefevre, J. (1996). Theory and practice of nuclear spin relaxation in proteins. Annu. Rev. Phys. Chem. *47*, 243-282.

de Feo, C.J., Aller, S.G., Siluvai, G.S., Blackburn, N.J., and Unger, V.M. (2009). Three-dimensional structure of the human copper transporter hCTR1. Proc. Natl. Acad. Sci. U.S.A. *106*, 4237–4242.

de Vries, S.J., van Dijk, M., and Bonvin, A.M.J.J. (2010). The HADDOCK web server for data-driven biomolecular docking. Nat. Protoc. *5*, 883–897.

Delaglio, F., Grzesiek, S., Vuister, G.W., Zhu, G., Pfeifer, J., and Bax, A. (1995). NMRPipe: a multidimensional spectral processing system based on UNIX pipes. J. Biomol. NMR *6*, 277–293.

DeLano, W., and Lam, J. (2005). PyMOL: A communications tool for computational models. Abstr. Pap. Am. Chem. S. *230*, U1371-U1372.

DeSilva, T.M., Veglia, G., and Opella, S.J. (2005). Solution structures of the reduced and Cu(I) bound forms of the first metal binding sequence of ATP7A associated with Menkes disease. Proteins *61*, 1038–1049.

Desmyter, A., Transue, T.R., Ghahroudi, M.A., Dao Thi, M-H., Poortmans, F., Hamers, R., Muyldermans, S., and Wyns, L. (1996). Crystal structure of a camel single-domain VH antibody fragment in complex with lysozyme. Nat. Struct. Biol. *3*, 803–811.

DiDonato, M., Hsu, H.-F., Narindrasorasak, S., Que, L., and Sarkar, B. (2000). Copper-induced conformational changes in the N-terminal domain of the Wilson disease copper-transporting ATPase. Biochemistry *39*, 1890–1896.

Dmitriev, O.Y., Lutsenko, S., and Muyldermans, S. (2016). Nanobodies as probes of protein dynamics *in vitro* and in cells. J. Biol. Chem. *291*, 3767-3775.

Dmitriev, O.Y., Tsivkovskii, R., Abildgaard, F., Morgan, C.T., Markley, J.L., and Lutsenko, S. (2006). Solution structure of the N-domain of Wilson disease protein: distinct nucleotide-binding environment and effects of disease mutations. Proc. Natl. Acad. Sci. U.S.A. *103*, 5302–5307.

Dolgova, N.V., Nokhrin, S., Yu, C.H., George, G.N., and Dmitriev, O.Y. (2013). Copper chaperone Atox1 interacts with the metal-binding domain of Wilson's disease protein in cisplatin detoxification. Biochem. J. *454*, 147–156.

Dolgova, N.V., Olson, D., Lutsenko, S., and Dmitriev, O.Y. (2009). The soluble metal-binding domain of the copper transporter ATP7B binds and detoxifies cisplatin. Biochem. J. *419*, 51-56.

Dosset, P., Hus, J., Blackledge, M., and Marion, D. (2000). Efficient analysis of macromolecular

rotational diffusion from heteronuclear relaxation data. J. Biomol. NMR. *16*, 23-28.

Elbing, K.L., and Brent, R. (1998). Media Preparation and Bacteriological Tools (Hoboken: John Wiley & Sons)

Fatemi, N., Korzhnev, D.M., Velyvis, A., Sarkar, B., and Forman-Kay, J.D. (2010). NMR characterization of copper-binding domains 4−6 of ATP7B. Biochemistry *49*, 8468–8477.

Fichtinger-Schepman, A., Van der Veer, J.L. (1985). Adducts of the antitumor drug cis-diamminedichloroplatinum (II) with DNA: formation, identification, and quantitation. Biochemistry *24*, 707–713.

Flores, A.G., and Unger, V.M. (2013). Atox1 contains positive residues that mediate membrane association and aid subsequent copper loading. J. Membr. Biol. *246*, 903–913.

Franke, D., and Svergun, D.I. (2009). DAMMIF, a program for rapid *ab-initio* shape determination in small-angle scattering. J. Appl. Crystallogr. *42*, 342-346.

Furuta, T., Ueda, T., Aune, G., Sarasin, A., Kraemer, K.H., and Pommier, Y. (2002). Transcription-coupled nucleotide excision repair as a determinant of cisplatin sensitivity of human cells. Cancer Res. *62*, 4899–4902.

Garrett, D., Seok, YJ, Peterkofsky, A., Clore, M., and Gronenborn, A. (1997). Identification by NMR of the binding surface for the histidine-containing phosphocarrier protein HPr on the N-terminal domain of enzyme I of the *Escherichia coli* phosphotransferase system. Biochemistry *36*, 4393-4398.

Gardner, K.H., and Kay, L.E. (1998). The use of ^{2}H, ^{13}C, ^{15}N multidimensional NMR to study the structure and dynamics of proteins. Annu. Rev. Biophys. Biomol. Struct. *27*, 357–406.

Gelasco, A., Lippard, S.J. (1998). NMR solution structure of a DNA dodecamer duplex containing a cis-diammineplatinum(II) d(GpG) intrastrand cross-link, the major adduct of the anticancer drug cisplatin. Biochemistry *37*, 9230–9239.

González-Guerrero, M., Argüello, J.M. (2008). Mechanism of Cu^{+}-transporting ATPases: soluble Cu^{+} chaperones directly transfer Cu^{+} to transmembrane transport sites. Proc. Natl. Acad. Sci. U.S.A. *105*, 5992–5997.

Gourdon, P., Liu, X.-Y., Skjørringe, T., Morth, J.P., Møller, L.B., Pedersen, B.P., and Nissen, P. (2011). Crystal structure of a copper-transporting PIB-type ATPase. Nature *475*, 59–64.

Göbl, C., Madl, T., Simon, B., and Sattler, M. (2014). NMR approaches for structural analysis of multidomain proteins and complexes in solution. Prog. Nucl. Magn. Reson. Spectrosc. *80*, 26–63.

Grzesiek, S., Bax, A., Clore, M., Gronenborn, A., Hu, JS., Kaufman, J., Palmer, I., Stahl, S., and

Wingfield, P. (1996). The solution structure of HIV-1 Nef reveals an unexpected fold and permits delineation of the binding surface for the SH3 domain of Hck tyrosine protein kinase. Nature 3, 340-345.

Guo, Y., Nyasae, L., Braiterman, L., and Hubbard, A. (2005). NH_2-terminal signals in ATP7B Cu-ATPase mediate its Cu-dependent anterograde traffic in polarized hepatic cells. Am. J. Physiol. *289*, G904–G916.

Gupta, A., Bhattacharjee, A., Dmitriev, O.Y., Nokhrin, S., Braiterman, L., Hubbard, A.L., and Lutsenko, S. (2011). Cellular copper levels determine the phenotype of the Arg875 variant of ATP7B/Wilson disease protein. Proc. Natl. Acad. Sci. U.S.A. *108*, 5390-5395.

Güntert, P. (1998). Structure calculation of biological macromolecules from NMR data. Q. Rev. Biophys. *31*, 145–237.

Hamza, I., Schaefer, M., Klomp, L.W.J., and Gitlin, J.D. (1999). Interaction of the copper chaperone HAH1 with the Wilson disease protein is essential for copper homeostasis. Proc. Natl. Acad. Sci. U.S.A. *96*, 13363-13368.

Harada, M., Kawaguchi, T., Kumemura, H., Terada, K., Ninomiya, H., Taniguchi, E., Hanada, S., Baba, S., Maeyama, M., Koga, H., Ueno, T., Furuta, K., Suganuma, T., Sugiyama, T., and Sata, M. (2010). The Wilson disease protein ATP7B resides in the late endosomes with Rab7 and the Niemann-Pick C1 protein. Am. J. Pathol. *166*, 499–510.

Harada, M., Sakisaka, S., Kawaguchi, T., Kimura, R., Taniguchi, E., Koga, H., Hanada, S., Baba, S., Furuta, K., Kumashiro, R., Sugiyama, T., and Sata, M. (2000). Copper does not alter the intracellular distribution of ATP7B, a copper-transporting ATPase. Biochem. Biophys. Res. Commun. *275*, 871–876.

Holzer, A.K., and Howell, S.B. (2006). The internalization and degradation of human copper transporter 1 following cisplatin exposure. Cancer Res. *66*, 10944–10952.

Huang, Y., Nokhrin, S., Hassanzadeh-Ghassabeh, G., Yu, C.H., Yang, H., Barry, A.N., Tonelli, M., Markley, J.L., Muyldermans, S., Dmitriev, O.Y., and Lutsenko, S. (2014). Interactions between metal-binding domains modulate intracellular targeting of Cu(I)-ATPase ATP7B, as revealed by nanobody binding. J. Biol. Chem. *289*, 32682–32693.

Hung, I.H., Suzuki, M., Yamaguchi, Y., Yuan, D.S., Klausner, R.D., and Gitlin, J.D. (1997). Biochemical characterization of the Wilson disease protein and functional expression in the yeast Saccharomyces cerevisiae. J. Biol. Chem. *272*, 21461–21466.

Huster, D. (2003). The distinct roles of the N-terminal copper-binding sites in regulation of catalytic activity of the Wilson's disease protein. J. Biol. Chem. *278*, 32212–32218.

Ishida, S., Lee, J., Thiele, D.J., and Herskowitz, I. (2002). Uptake of the anticancer drug cisplatin mediated by the copper transporter Ctr1 in yeast and mammals. Proc. Natl. Acad. Sci. U.S.A. *99*,

14298–14302.

Ishida, S., McCormick, F., Smith-McCune, K., and Hanahan, D. (2010). Enhancing tumor-specific uptake of the anticancer drug cisplatin with a copper chelator. Cancer Cell *17*, 574–583.

Ishikawa, T., Ali-Osman, F. (1993). Glutathione-associated cis-diamminedichloroplatinum(II) metabolism and ATP-dependent efflux from leukemia cells. Molecular characterization of glutathione-platinum complex and its biological significance. J. Biol. Chem. *268*, 20116–20125.

Itoh, S., Kim, H.W., Nakagawa, O., Ozumi, K., Lessner, S.M., Aoki, H., Akram, K., McKinney, R.D., Ushio-Fukai, M., and Fukai, T. (2008). Novel role of antioxidant-1 (Atox1) as a copper-dependent transcription factor involved in cell proliferation. J. Biol. Chem. *283*, 9157–9167.

Jamieson, E.R., and Lippard, S.J. (1999). Structure, recognition, and processing of cisplatin−DNA adducts. Chem. Rev. *99*, 2467–2498.

Johnson, B.A. (2004). Using NMRView to visualize and analyze the NMR spectra of macromolecules. Methods Mol. Biol. *278*, 313–352.

Jung, Y., and Lippard, S.J. (2007). Direct cellular responses to platinum-induced DNA damage. Chem. Rev. *107*, 1387–1407.

Kaler, S.G. (2011). ATP7A-related copper transport diseases—emerging concepts and future trends. Nature *7*, 15–29.

Kay, L.E., Torchia, D.A., and Bax, A. (1989). Backbone dynamics of proteins as studied by ^{15}N inverse detected heteronuclear NMR spectroscopy: application to staphylococcal nuclease. Biochemistry *28*, 8972–8979.

Keller, R.L.J. (2005). Optimizing the process of nuclear magnetic resonance spectrum analysis and computer aided resonance assignment [Doctoral dissertation]. Institute of Molecular Biology and Biophysics, ETH Zürich. 149 p.

Kenney, S.M., and Cox, D.W. (2007). Sequence variation database for the Wilson disease copper transporter, ATP7B. Hum. Mutat. *28*, 1171–1177.

Komatsu, M., Sumizawa, T., Mutoh, M., Chen, Z.S., Terada, K., Furukawa, T., Yang, X.L., Gao, H., Miura, N., Sugiyama, T., and Akiyama, S. (2000). Copper-transporting P-type adenosine triphosphatase (ATP7B) is associated with cisplatin resistance. Cancer Res. *60*, 1312–1316.

Konarev, P., Volkov, V., Sokolova, A., Koch, H., and Svergun, D. (2003). PRIMUS: a Windows PC-based system for small-angle scattering data analysis. J. Appl. Cryst. *36*, 1277-1282.

Kurokawa, H., Ishida, T., Nishio, K., Arioka, H., Sata, M., Fukumoto, H., Miura, M., and Saijo, N. (1995). Gamma-glutamylcysteine synthetase gene overexpression results in increased activity of the ATP-dependent glutathione S-conjugate export pump and cisplatin resistance. Biochem.

Biophys. Res. Commun. *216*, 258–264.

Lalioti, V., Peiró, R., Pérez-Berlanga, M., Tsuchiya, Y., Muñoz, A., Villalba, T., Sanchez, C., and Sandoval, I.V. (2016). Basolateral sorting and transcytosis define the Cu^{+}-regulated translocation of ATP7B to the bile canaliculus. J. Cell. Sci. *129*, 2190-2201.

Laskowski, R., MacArthur, M., Moss, D., and Thornton, J. (1993). PROCHECK - a program to check the stereochemical quality of protein structures. J. Appl. Cryst. *26*, 283-291.

Lee, W., Kim, J.H., Westler, W.M., and Markley, J.L. (2011). PONDEROSA, an automated 3D-NOESY peak picking program, enables automated protein structure determination. Bioinformatics *27*, 1727–1728.

Lee, W., Stark, J.L., and Markley, J.L. (2014). PONDEROSA-C/S: client-server based software package for automated protein 3D structure determination. J. Biomol. NMR. 60, 73-75.

Lee, W., Tonelli, M., and Markley, J. (2014). NMRFAM-SPARKY: enhanced software for biomolecular NMR spectroscopy. Bioinformatics 31, 1325-1327.

LeShane, E.S., Shinde, U., Walker, J.M., Barry, A.N., Blackburn, N.J., Ralle, M., and Lutsenko, S. (2010). Interactions between copper-binding sites determine the redox status and conformation of the regulatory N-terminal domain of ATP7B. J. Biol. Chem. *285*, 6327–6336.

Linder, M., and Hazegh-Azam, M. (1996). Copper biochemistry and molecular biology. Am. J. Clin. Nutr. *63*, 797-811.

Lovell, S., Davis, I., Arendall, W., de Bakker, P., Word, J., Prisant, M., Richardson, J., and Richardson, D. (2003). Structure validation by Cα geometry: ϕ, ψ and Cβ deviation. Proteins *50*, 437-450.

Lutsenko, S., Barnes, N.L., Bartee, M.Y., and Dmitriev, O.Y. (2007). Function and regulation of human copper-transporting ATPases. Physiol. Rev. *87*, 1011–1046.

Lutsenko, S., Petrukhin, K., and Cooper, M. (1997). N-terminal domains of human copper-transporting adenosine triphosphatases (the Wilson's and Menkes disease proteins) bind copper selectively in vivo and in vitro with stoichiometry of one copper per metal-binding repeat. J. Biol. Chem. *272*, 18939-18944.

Maryon, E.B., Molloy, S.A., and Kaplan, J.H. (2013). Cellular glutathione plays a key role in copper uptake mediated by human copper transporter 1. Am. J. Phys. *304*, C768–C779.

Molloy, S.A., Kaplan, J.H. (2009). Copper-dependent recycling of hCTR1, the human high affinity copper transporter. J. Biol. Chem. *284*, 29704–29713.

Mondol, T., Ådén, J., and Wittung-Stafshede, P. (2016). Copper binding triggers compaction in N-terminal tail of human copper pump ATP7B. Biochem. Biophys. Res. Commun. 470, 1–7.

Morris, G.A., and Freeman, R. (1979). Enhancement of nuclear magnetic resonance signals by polarization transfer. J. Am. Chem. Soc. *101*, 760–762.

Muller, P.A.J., and Klomp, L.W.J. (2009). ATOX1: A novel copper-responsive transcription factor in mammals? Int. J. Biochem. Cell Biol. *41*, 1233–1236.

Muyldermans, S. (2013). Nanobodies: natural single-domain antibodies. Annu. Rev. Biochem. *82*, 775–797.

Nakayama, K., Kanzaki, A., Ogawa, K., Miyazaki, K., Neamati, N., and Takebayashi, Y. (2002). Copper-transporting P-type adenosine triphosphatase (ATP7B) as a cisplatin based chemoresistance marker in ovarian carcinoma: comparative analysis with expression of MDR1, MRP1, MRP2, LRP, and BCRP. Int. J. Cancer *101*, 488–495.

Nakayama, K., Kanzaki, A., Terada, K., Mutoh, M., Ogawa, K., Sugiyama, T., Takenoshita, S., Itoh, K., Yaegashi, N., Miyazaki, K., Neamati, N., and Takebayashi, Y. (2004). Prognostic value of the Cu-transporting ATPase in ovarian carcinoma patients receiving cisplatin-based chemotherapy. Clin. Cancer Res. *10*, 2804–2811.

Nehmé, A., Baskaran, R., Aebi, S., Fink, D., Nebel, S., Cenni, B., Wang, J.Y., Howell, S.B., and Christen, R.D. (1997). Differential induction of c-Jun NH2-terminal kinase and c-Abl kinase in DNA mismatch repair-proficient and -deficient cells exposed to cisplatin. Cancer Res. *57*, 3253–3257.

Nyasae, L.K., Schell, M.J., and Hubbard, A.L. (2014). Copper directs ATP7B to the apical domain of hepatic cells via basolateral endosomes. Traffic *15*, 1344–1365.

Overhauser, A.W. (1953). Polarization of nuclei in metals. Phys. Rev. *92*, 411–415.

Palm, M.E., Weise, C.F., Lundin, C., Wingsle, G., Nygren, Y., Björn, E., Naredi, P., Wolf-Watz, M., and Wittung-Stafshede, P. (2011). Cisplatin binds human copper chaperone Atox1 and promotes unfolding in vitro. Proc. Natl. Acad. Sci. U.S.A. *108,* 6951–6956.

Palm-Espling, M.E. (2013). Copper-transporting proteins and their interactions with platinum-based anticancer substances [Doctoral Dissertation]. Department of Chemistry, Umeå University. 110 p.

Palm-Espling, M.E., Andersson, C.D., Björn, E., Linusson, A., and Wittung-Stafshede, P. (2013). Determinants for simultaneous binding of copper and platinum to human chaperone Atox1: hitchhiking not hijacking. PloS One *8*, e70473.

Pardon, E., Laeremans, T., Triest, S., Rasmussen, S., Wohlkonig, A., Ruf, A., Muyldermans, S., Hol, W., Kobilka, B., and Steyaert, J. (2014). A general protocol for the generation of Nanobodies for structural biology. Nat. Protoc. *9*, 674–693.

Peña, M.M., Lee, J., and Thiele, D.J. (1999). A delicate balance: homeostatic control of copper uptake and distribution. J. Nutr. *129*, 1251–1260.

Pervushin, K., Riek, R., Wider, G., and Wüthrich, K. (1997). Attenuated T2 relaxation by mutual cancellation of dipole–dipole coupling and chemical shift anisotropy indicates an avenue to NMR structures of very large biological macromolecules in solution. Proc. Natl. Acad. Sci. U.S.A. *94*, 12366–12371.

Petoukhov, M.V., Franke, D., Shkumatov, A.V., Tria, G., Kikhney, A.G., Gajda, M., Gorba, C., Mertens, H.D.T., Konarev, P.V., and Svergun, D.I. (2012). New developments in the ATSAS program package for small-angle scattering data analysis. J. Appl. Crystallogr. *45*, 342–350.

Polishchuk, E.V., Concilli, M., Iacobacci, S., Chesi, G., Pastore, N., Piccolo, P., Paladino, S., Baldantoni, D., van IJzendoorn, S.C.D., Chan, J., Chang, C.J., Amoresano, A., Pane, F., Pucci, P., Tarallo, A., Parenti, G., Brunetti-Pierri, N., Settembre, C., Ballabio, A., and Polishchuk, R.S. (2014). Wilson disease protein ATP7B utilizes lysosomal exocytosis to maintain copper homeostasis. Dev. Cell *29*, 686–700.

Pope, C.R., De Feo, C.J., and Unger, V.M. (2013). Cellular distribution of copper to superoxide dismutase involves scaffolding by membranes. Proc. Natl. Acad. Sci. U.S.A. *110*, 20491-20496.

Ralle, M., Lutsenko, S., and Blackburn, N.J. (2004). Copper transfer to the N-terminal domain of the Wilson disease protein (ATP7B): X-ray absorption spectroscopy of reconstituted and chaperone-loaded metal binding domains and their interaction with exogenous ligands. J. Inorg. Biochem. *98*, 765–774.

Rasmussen, S., Choi, H., Fung, J., Pardon, E., Casarosa, P., Chae, P., Devree, B., Rosenbaum, D., Thian, F., Kobilka, T., Schnapp, A., Konetzki, I., Sunahara, R., Gellman, S., Pautsch, A., Steyaert, J., Weis, W., and Kobilka, B. (2011). Structure of a nanobody-stabilized active state of the β2 adrenoceptor. Nature *469*, 175-180.

Ravia, J.J., Stephen, R.M., Ghishan, F.K., and Collins, J.F. (2005). Menkes copper ATPase (Atp7a) is a novel metal-responsive gene in rat duodenum, and immunoreactive protein is present on brush-border and basolateral membrane domains. J. Biol. Chem. *280*, 36221–36227.

Reddy, T., and Rainey, J.K. (2010). Interpretation of biomolecular NMR spin relaxation parameters. Biochem. Cell Biol. *88*, 131–142.

Roelofsen, H., Wolters, H., Van Luyn, M.J.A., Miura, N., Kuipers, F., and Vonk, R.J. (2000). Copper-induced apical trafficking of ATP7B in polarized hepatoma cells provides a mechanism for biliary copper excretion. Gastroenterol. *119*, 782–793.

Safaei, R., Maktabi, M.H., Blair, B.G., Larson, C.A., and Howell, S.B. (2009). Effects of the loss of Atox1 on the cellular pharmacology of cisplatin. J. Inorg. Biochem. *103*, 333–341.

Safaei, R., Otani, S., Larson, B.J., Rasmussen, M.L., and Howell, S.B. (2007). Transport of

cisplatin by the copper efflux transporter ATP7B. Mol. Pharmacol. *73*, 461–468.

Sazinsky, M.H., Mandal, A.K., Arguello, J.M., Rosenzweig, A.C. (2006). Structure of the ATP binding domain from the *Archaeoglobus fulgidus* Cu^{+}-ATPase. J. Biol. Chem. *281*, 11161–11166.

Schaefer, M., Hopkins, R.G., Failla, M.L., and Gitlin, J.D. (1999). Hepatocyte-specific localization and copper-dependent trafficking of the Wilson's disease protein in the liver. Am. J. Physiol. *276*, G639–G646.

Schilsky, M.L. (2002). Diagnosis and treatment of Wilson's disease. Pediatr. Transplant. *6*, 15–19.

Schushan, M., Bhattacharjee, A., Ben-Tal, Nir, and Svetlana, S. (2012). A structural model of the copper ATPase ATP7B to facilitate analysis of Wilson disease-causing mutations and studies of the transport mechanism. Metallomics *4*, 669-678.

Schwieters, C., Kusewski, J., and Clore, M. (2006). Using Xplor–NIH for NMR molecular structure determination. Prog. Nucl. Magn. Reson. Spectrosc. *48*, 47–62.

Shah, A.B., Chernov, I., Zhang, H.T., Ross, B.M., Das, K., Lutsenko, S., Parano, E., Pavone, L., Evgrafov, O., Ivanova-Smolenskaya, I.A., Annerén, G., Westermark, K., Urrutia, F.H., Penchaszadeh, G.K., Sternlieb, I., Scheinberg, I.H., Gilliam, T.C., and Petrukhin, K. (1997). Identification and analysis of mutations in the Wilson disease gene (ATP7B): population frequencies, genotype-phenotype correlation, and functional analyses. Am. J. Hum. Genet. *61*, 317–328.

Shen, Y., and Bax, A. (2013). Protein backbone and sidechain torsion angles predicted from NMR chemical shifts using artificial neural networks. J. Biomol. NMR *56*, 227–241.

Sinani, D., Adle, D.J., Kim, H., and Lee, J. (2007). Distinct mechanisms for Ctr1-mediated copper and cisplatin transport. J. Biol. Chem. *282*, 26775–26785.

Singleton, W.C.J., McInnes, K.T., Cater, M.A., Winnall, W.R., McKirdy, R., Yu, Y., Taylor, P.E., Ke, B.X., Richardson, D.R., Mercer, J.F.B., and La Fontaine, S. (2010). Role of glutaredoxin1 and glutathione in regulating the activity of the copper-transporting P-type ATPases, ATP7A and ATP7B. J. Biol. Chem. *285*, 27111–27121.

Spronk, C., Nabuurs, S., Krieger, E., Vriend, G., Vuister, G. (2004). Validation of protein structures derived by NMR spectroscopy. Prog. Nucl. Magn. Reson. Spectrosc. *45*, 315-337.

States, J.C., Reed, E. (1996). Enhanced XPA mRNA levels in cisplatin-resistant human ovarian cancer are not associated with XPA mutations or gene amplification. Cancer Lett. *108*, 233–237.

Stein, E.G., Rice, L.M., and Brünger, A.T. (1997). Torsion-angle molecular dynamics as a new efficient tool for NMR structure calculation. J. Magn. Reson. *124*, 154–164.

Tadini-Buoninsegni, F., Bartolommei, G., Moncelli, M.R., Inesi, G., Galliani, A., Sinisi, M., Losacco, M., Natile, G., and Arnesano, F. (2014). Translocation of platinum anticancer drugs by human copper ATPases ATP7A and ATP7B. Angew. Chem. Int. Ed. *53*, 1297-1301.

Toyoshima, C., Nakasako, M., Nomura, H., and Ogawa, H. (2000). Crystal structure of the calcium pump of sarcoplasmic reticulum at 2.6 Å resolution. Nature *405*, 647-655.

Tsivkovskii, R., MacArthur, B., and Lutsenko, S. (2001). The Lys^{1010}-Lys^{1325} fragment of the Wilson's disease protein binds nucleotides and interacts with the N-terminal domain of this protein in a copper-dependent manner. J. Biol. Chem. *276*, 2234–2242.

Walker, J., Huster, D., Ralle, M., Morgan, C., Blackburn, N., and Lutsenko, S. (2004). The N-terminal metal-binding site 2 of the Wilson's disease protein plays a key role in the transfer of copper from Atox1. J. Biol. Chem. *279*, 15376–15384.

Ward, E.S., Güssow, D., Griffiths, A.D., Jones, P.T., and Winter, G. (1989). Binding activities of a repertoire of single immunoglobulin variable domains secreted from *Escherichia coli.* Nature *341*, 544–546.

Wernimont, A.K. (2003). Binding of copper(I) by the Wilson disease protein and its copper chaperone. J. Biol. Chem. *279*, 12269–12276.

Williamson, M.P. (2006). The Nuclear Overhauser Effect. In Modern Magnetic Resonance, G. Webb, ed. (Netherlands: Springer), pp. 409–412.

Wishart, D.S., Sykes, B.D., and Richards, F.M. (1992). The chemical shift index: a fast and simple method for the assignment of protein secondary structure through NMR spectroscopy. Biochemistry *31*, 1647–1651.

Wüthrich, K. (1989). Protein structure determination in solution by nuclear magnetic resonance spectroscopy. Science *243*, 45-50.

Yatsunyk, L.A., Rosenzweig, A.C. (2007). Cu(I) binding and transfer by the N-terminus of the Wilson disease protein. J. Biol. Chem. *282*, 8622–8631.

Yoshizawa, K., Nozaki, S., Kitahara, H., Ohara, T., Kato, K., Kawashiri, S., and Yamamoto, E. (2007). Copper efflux transporter (ATP7B) contributes to the acquisition of cisplatin-resistance in human oral squamous cell lines. Oncol. Rep. *18*, 987–991.

Zhu, G., Xia, Y., Nicholson, L.K., Sze, K.H. (2000). Protein dynamics measurements by TROSY-based NMR experiments. J. Magn. Reson. 1*43*, 423–426.